INFORMATION TO USERS

This manuscript has been reproduced from the microfilm master. UMI films the text directly from the original or copy submitted. Thus, some thesis and dissertation copies are in typewriter face, while others may be from any type of computer printer.

The quality of this reproduction is dependent upon the quality of the copy submitted. Broken or indistinct print, colored or poor quality illustrations and photographs, print bleedthrough, substandard margins, and improper alignment can adversely affect reproduction.

In the unlikely event that the author did not send UMI a complete manuscript and there are missing pages, these will be noted. Also, if unauthorized copyright material had to be removed, a note will indicate the deletion.

Oversize materials (e.g., maps, drawings, charts) are reproduced by sectioning the original, beginning at the upper left-hand corner and continuing from left to right in equal sections with small overlaps.

ProQuest Information and Learning
300 North Zeeb Road, Ann Arbor, MI 48106-1346 USA
800-521-0600

Université d'Ottawa • University of Ottawa

PERMISSION DE REPRODUIRE ET DE DISTRIBUER LA THÈSE

PERMISSION TO REPRODUCE AND DISTRIBUTE THE THESIS

NOM DE L'AUTEUR / NAME OF AUTHOR:	GAUTHIER, Éric
ADRESSE POSTALE / MAILING ADDRESS:	C.P. 454, 10 RUE BERGEVIN ST-ISIDORE ON K0C2B0
GRADE / DEGREE:	**ANNÉE D'OBTENTION / YEAR GRANTED**
M.Sc. (Earth Sciences)	2003
TITRE DE LA THÈSE / TITLE OF THESIS: THE POTENTIAL OF AIRBORNE SYNTHETIC APERTURE RADAR (SAR) IMAGERY AS A BASIC TOOL FOR STRATIGRAPHIC INVESTIGATIONS IN FORESTED AREAS: THE ORDOVICIAN-SILIRIAN CARBONATE SUCCESSION OF ANTICOSTI ISLAND, GULF OF ST. LAWRENCE, EASTERN CANADA	

L'auteur permet, par la présente, la consultation et le prêt de cette thèse en conformité avec les règlements établis par le bibliothécaire en chef de l'Université d'Ottawa. L'auteur autorise aussi l'Université d'Ottawa, ses successeurs et cessionnaires, à reproduire cet exemplaire par photograhie ou photocopie pour fins de prêt ou de vente au prix coûtant aux bibliothèques ou aux chercheurs qui en feront la demande.

Les droits de publication par tout autre moyen et pour vente au public demeureront la propriété de l'auteur de la thèse sous réserve des règlements de l'Université d'Ottawa en matière de publication de thèses.

The author hereby permits the consultation and the lending of this thesis pursuant to the regulations established by the Chief Librarian of the University of Ottawa. The author also authorizes the University of Ottawa, its successors and assignees, to make reproductions of this copy by photographic means or by photocopying and to lend or sell such reproductions at cost to libraries and to scholars requesting them.

The right to publish the thesis by other means and to sell it to the public is reserved to the author, subject to the regulations of the University of Ottawa governing the publication of theses.

N.B. LE MASCULIN COMPREND ÉGALEMENT LE FÉMININ

17 juin 2003

DATE

(AUTEUR) SIGNATURE (AUTHOR)

Université d'Ottawa • University of Ottawa

Université d'Ottawa • University of Ottawa

FACULTÉ DES ÉTUDES SUPÉRIEURES ET POSTDOCTORALES

FACULTY OF GRADUATE AND POSTDOCTORAL STUDIES

GAUTHIER, .Éric L.

AUTEUR DE LA THÈSE - AUTHOR OF THESIS

M.Sc. (Earth Sciences)

GRADE - DEGREE

Earth Sciences

FACULTÉ, ÉCOLE, DÉPARTEMENT - FACULTY, SCHOOL, DEPARTMENT

TITRE DE LA THÈSE - TITLE OF THE THESIS

The Potential of Airborne Synthetic Aperture Radar (SAR) Imagery as a Basic Tool for Stratigraphic Investigations in Forested Areas: The Ordovician-Silurian Carbonate Succession of Anticosti Island, Gulf of St. Lawrence, Eastern Canada

André Desrochers and Marc D'Iorio

DIRECTEUR DE LA THÈSE - THESIS SUPERVISOR

EXAMINATEURS DE LA THÈSE - THESIS EXAMINERS

J. Blenkinsop

A. Bannari

J.-M. De Koninck, Ph.D.

LE DOYEN DE LA FACULTÉ DES ÉTUDES SUPÉRIEURES ET POSTDOCTORALES

SIGNATURE

DEAN OF THE FACULTY OF GRADUATE AND POSTDOCTORAL STUDIES

THE POTENTIAL OF AIRBORNE SYNTHETIC APERTURE RADAR (SAR) IMAGERY AS A BASIC TOOL FOR STRATIGRAPHIC INVESTIGATIONS IN FORESTED AREAS: THE ORDOVICIAN-SILURIAN CARBONATE SUCCESSION OF ANTICOSTI ISLAND, GULF OF ST. LAWRENCE, EASTERN CANADA.

by

Eric L. Gauthier

A thesis submitted to the Faculty of Graduate and Postdoctoral Studies

in partial fulfillment of the requirements

for the degree of M.Sc. in Earth Sciences

OTTAWA-CARLETON GEOSCIENCE CENTRE

AND

UNIVERSITY OF OTTAWA

OTTAWA, CANADA

ABSTRACT

Anticosti Island, located in the Gulf of St. Lawrence in eastern Canada, is one of the few places in the world where the Ordovician/Silurian boundary is well preserved and exposed. Its relatively undeformed shallow-water carbonate sequence of approximately 900 m in thickness is rich in fossils and is known to contain traces of hydrocarbons. The island has been for decades the subject of several geological studies, but its stratigraphic succession was never successfully mapped precisely because of its dense forest cover present over almost 95 % of its vast territory.

This study provides new mapping tools and techniques to support the geological representation of the island stratigraphic succession. Airborne SAR (Synthetic Aperture Radar) data acquired with the active radar system onboard of the former CCRS (Canada Centre for Remote Sensing) Convair-580 aircraft, in single and fully polarimetric modes and with different viewing geometry, were qualitatively and quantitatively evaluated by means of image interpretation and polarimetric analysis for their mapping potential over the densely forested study area.

The airborne SAR data, supported with ancillary geoscience data sets and derivative topographic related products, have resulted in the availability of valuable and accurate terrain information such as topographic variations associated with the gently inclined recessive and resistant strata of the island succession. It also provided with information on the polarimetric

scattering mechanism of the vegetation cover overlying the surface deposits and bedrock geology, suggesting a possible preferential distribution.

With almost 50 % of the Canadian territory covered by forest, radar remote sensing, as demonstrated by this study, is a cost-effective tool to produce more accurate regional structural and geological map in areas where traditional mapping campaigns failed due to the presence of an extensive vegetation cover.

RÉSUMÉ

L'île d'Anticosti, située dans le golfe du Saint-Laurent à l'est du Canada, est l'un des seuls endroits au monde où le contact Ordovicien/Silurien est aussi bien préservé et exposé. Cette séquence d'environ 900 m d'épaisseur de carbonates d'eau peu profonde relativement peu déformé est riche en fossile et est connue pour contenir des traces d'hydrocarbures. L'île a été le sujet d'études géologiques depuis plusieurs décennies, mais sa succession stratigraphique n'a jamais été cartographiée précisément à cause de son dense couvert forestier s'étalant sur près de 95 % de son vaste territoire.

Cette étude procure de nouveaux outils et techniques de cartographie pour appuyer la représentation géologique de la succession stratigraphique de l'île. Des données RSO (Radar à synthèse d'ouverture) aéroportées acquises grâce au system radar actif à bord de l'aéronef Convair-580 anciennement du CCT (Centre canadien de télédétection), en modes polarimétriques simple et multiple et avec visés géométriques variés, ont été qualitativement et quantitativement évaluées à partir d'interprétation d'image et d'analyse polarimétrique pour leur potentiel de cartographie géologique au-dessus de la région d'étude à forte densité forestière.

Les données aéroportées RSO, appuyées par des ensembles de données géoscientifiques auxiliaires et des produits topographiques dérivés, ont fourni des informations de terrain précieuses et précises telles les variations topographiques associées aux strates résistantes et récessives légèrement inclinées de la succession de l'île. Elles ont aussi fourni de

l'information sur le mécanisme de diffusion polarimétrique du couvert végétal sus-jacent les dépôts de surfaces et le substrat rocheux suggérant possiblement une distribution préférentielle.

Avec tout près de 50 % du territoire canadien couvert de forêts, la télédétection radar, comme démontré par cette étude, est un outil rentable pour produire plus précisément des cartes régionales géologiques et structurales en régions où les campagnes de terrain traditionnelles ont échoué à cause de la présence extensive du couvert végétal.

ACKNOWLEDGMENTS

I would like to express my gratitude to everyone who contributed directly or indirectly to the accomplishment of this project. First, I would like to thank Dr. André Desrochers, my thesis director, for his guidance and his immense patience. A particular expression of thanks to Dr. Marc D'Iorio, my co-supervisor, who gave me the opportunity to work on this project at the Canada Centre for Remote Sensing (CCRS), part of Natural Resources Canada, and therefore benefit from the facilities and valuable resources provided by the institution. Without the financial support of the CCRS, the acquisition of the airborne SAR data would have been impossible. Many thanks to Dr. Bob Hawkins and his team for the acquisition, calibration, and pre-processing of the SAR data and to Dr. Ridha Touzi and his research assistant for their help with the polarimetric analysis software developed to extract polarimetric parameters from SAR data. The fieldwork logistic was greatly facilitated by the support of Jean Boisclair, *Direction des parc québécois, Ministère de l'Environnement et de la Faune.* It was also a pleasure to work with Yan Troutet and Karine Bédard, from whom I benefited of their assistance in the field and their help in processing the polarimetric SAR data. Claude Dufour, from *Produit Forestier Anticosti*, was of great help since she provided various GIS data sets used to achieve this project. The expertise and precious advice of Dr. Paul Copper and Dr. Darrel Long from the Laurentian University of Sudbury were sincerely appreciated. And finally, a special thanks to my lovely wife Nancy and all family members who provided the moral support needed to complete this thesis.

TABLE OF CONTENTS

LIST OF TABLES

LIST OF FIGURES

1. Introduction

Remote sensing imagery taken from airborne and satellite platforms are valuable for geological mapping, but since every sensor responds differently to the various terrain parameters, their information content is not the same and requires to be interpreted and analysed accordingly. Optical remote sensing images[1] are ideal to map lithological variations from arid and semi-arid terrains, but over forested areas their effectiveness is often reduced. The sensitivity of optical sensors to the high-frequency spatial details of vegetation cover limits the underlying bedrock geology to be mapped accurately. Actually, most remote sensing sensors are affected by the presence of vegetation and cannot provide direct lithological information of forested terrains. In order to overcome that common problem, it is important to select the appropriate system that enhanced the most the distinctive topographic patterns associated with the lithological and structural geology despite the vegetation cover. As it will be demonstrated in this study, the viewing geometry and polarisation capability of side-looking Synthetic Aperture Radar (SAR) systems are believed to be better suited for mapping topographic variations associated with the lithological and structural geology of forested terrains.

[1] *Optical remote sensing images are acquired by satellite or airborne sensors generating, transmitting, and detecting electromagnetic radiation in the spectral range extending from the long wave edge of the x-ray region to the short wave edge of the radio region including the UV, visible, NIR, SWIR, FIR, and TIR bands.*

1.1 Study Purpose and Objectives

The purpose of this study is to evaluate the potential of airborne SAR data to support geological mapping of forested areas. To achieve that goal, airborne SAR data acquired, calibrated, and pre-processed by the Canada Centre for Remote Sensing (CCRS) with the Convair-580 side-looking radar system in wide and narrow swath configurations and in single and fully polarimetric modes over Anticosti Island (Figure 1-1) will be visually interpreted and quantitatively analysed.

Even though superb bedrock exposures can be found all along the coast of Anticosti Island, within its riverbeds, and along its road network, previous field campaigns were largely limited in mapping precisely its geology since almost 95 % of its territory is covered by a dense boreal forest. The lack of ground control in inaccessible sectors has always resulted in inaccurate geology maps, but it is believed that valuable terrain information over these areas can be extracted from SAR data to improve the representation of the island stratigraphy. The first objective of this study is to produce a more precise geology map of the island by visually interpreting the single polarimetric wide-swath SAR data. The second objective is to quantitatively analyse the fully polarimetric narrow-swath SAR data to identify any preferential distribution of the vegetation cover with respect to the underlying surface deposits and bedrock geology. The results of these two approaches will be used to determine if SAR remote sensing with its flexible viewing geometry and polarisation capability can assist geological mapping over densely forested terrains like Anticosti Island.

Figure 1-1: Location of Anticosti Island with respect to the Québec Reentrant (*1*) and the St. Lawrence Promontory (*2*).

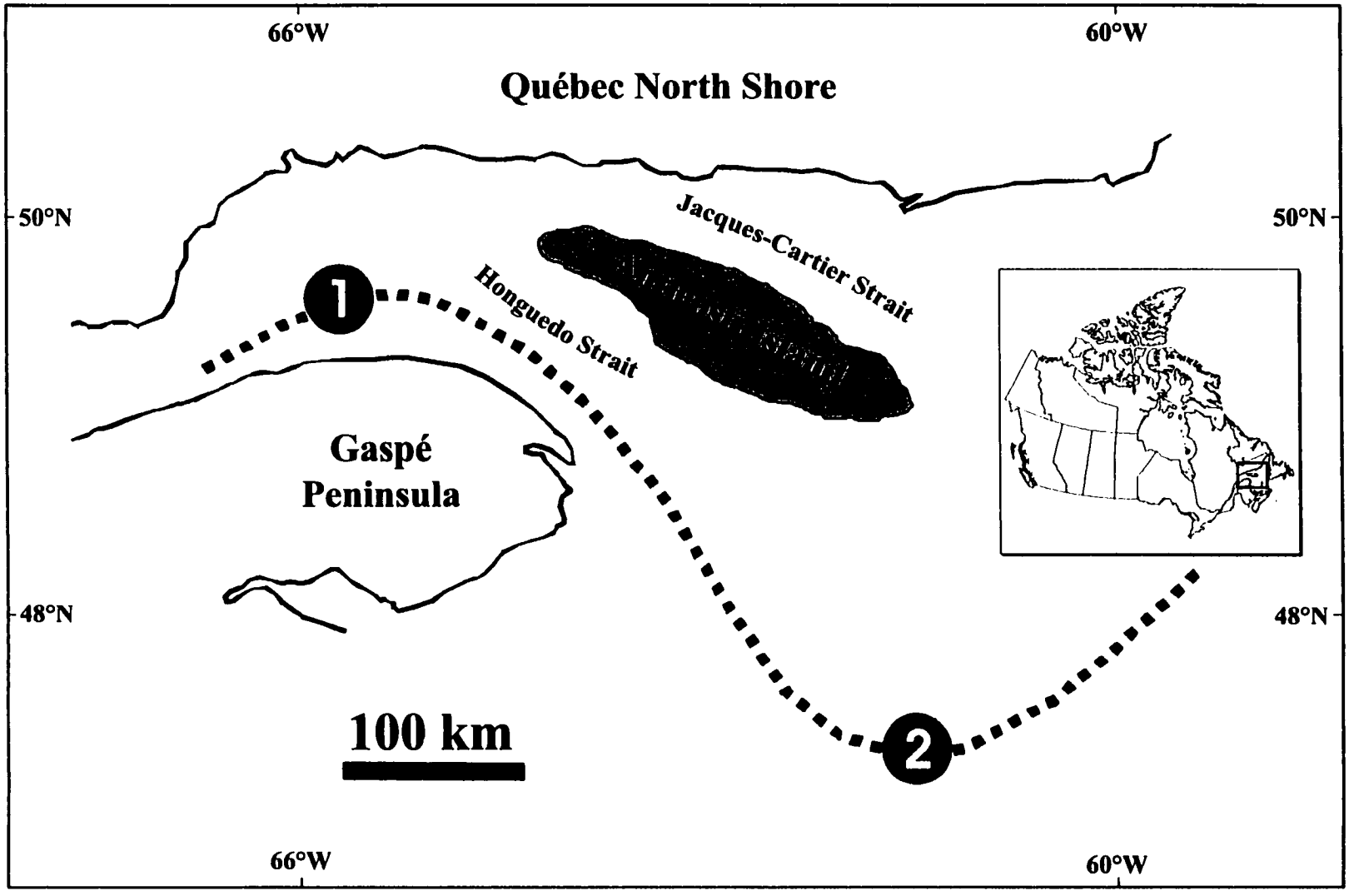
66°W
60°W
Québec North Shore
50°N
50°N
Jacques-Cartier Strait
Honguedo Strait
1
Gaspé
Peninsula
48°N
48°N
100 km
2
66°W
60°W

The following section explains the problems encountered by the traditional mapping campaigns conducted over Anticosti Island in the past and the need to evaluate the potential of airborne SAR data in various swath configurations and polarimetric modes in this study.

1.2 Statement of Problems

1.2.1 New Stratigraphic Framework

The geology of the Anticosti Island has been the subject of numerous studies for more than a century now. It all started with Richardson (1857) who looked and defined from coastal sections the island stratigraphy and macro-paleontology. Many bio-stratigraphic studies followed, but it is only in the early twentieth century that a formal stratigraphic definition was given to the carbonate sequence of the island by Schuchert and Twenhofel (1910) and then by Twenhofel (1914, 1919, and 1928).

For a couple of decades following Schuchert and Twenhofel contributions, little attention was dedicated to its stratigraphy. A new phase of geological investigations reappeared in the early sixties due to interest in the island oil and gas potential (Roliff, 1968). Bolton (1961, 1965, 1970, and 1972) for the Geological Survey of Canada was really the first one to initiate litho-stratigraphic and bio-stratigraphic studies within the interior of the island since it became more accessible due to the expansion of a road network for the logging activities. Additional litho-stratigraphic, macro-paleontological and micro-paleontological observations from newly discovered outcrops along roads and rivers, mostly in the northwestern part of

the island, allowed Bolton to redefine some of Twenhofel's formations. The task was rather difficult since the former formation contacts were lithologically indistinguishable due to their definition based largely on bio-stratigraphy principles (Petryk, 1981a).

Right after the acquisition of the island in 1974 by the government of Québec, the *Ministère de l'Énergie et des Ressources (MER)* undertook an exhaustive geological program to map in details the geology of Anticosti. Petryk (1979 and 1981a) was in charge of that mapping campaign from which he revised the stratigraphic framework laid by Twenhofel (1914, 1919, and 1928) and later redefined by Bolton (1961, 1965, 1970, and 1972). From his geological interpretation, supported by field observations and air photo examinations, three map sheets covering the whole island were produced at a scale of 1:100 000 by the *MER* (Petryk, 1981b). Figure 1-2 is a simplified version of the geology map of Petryk showing the six stratigraphic formations of the island with their defined and inferred contacts.

The stratigraphic interpretation of Petryk (1981b) was up to recently the most referred to even though several recent studies in paleontology (Brunton and Copper, 1994; Copper, 1989; Copper and Jisuo, 1995; Lespérance, 1985), stratigraphy (Barnes, 1988; Copper and Long, 1989 and 1990; Long and Copper, 1987), chrono-stratigraphy (Barnes, 1989; Orth *et al.*, 1986), and sedimentology (Sami and Desrochers, 1992; Desrochers *et al.*, 1998) had significant improvements to recommend. Among all these studies, it is really Copper and Long (1989) who proposed the most significant changes by the recognition of a new shaly

Figure 1-2: Sketch map of the geology of Anticosti Island by Pretyk (1981a).

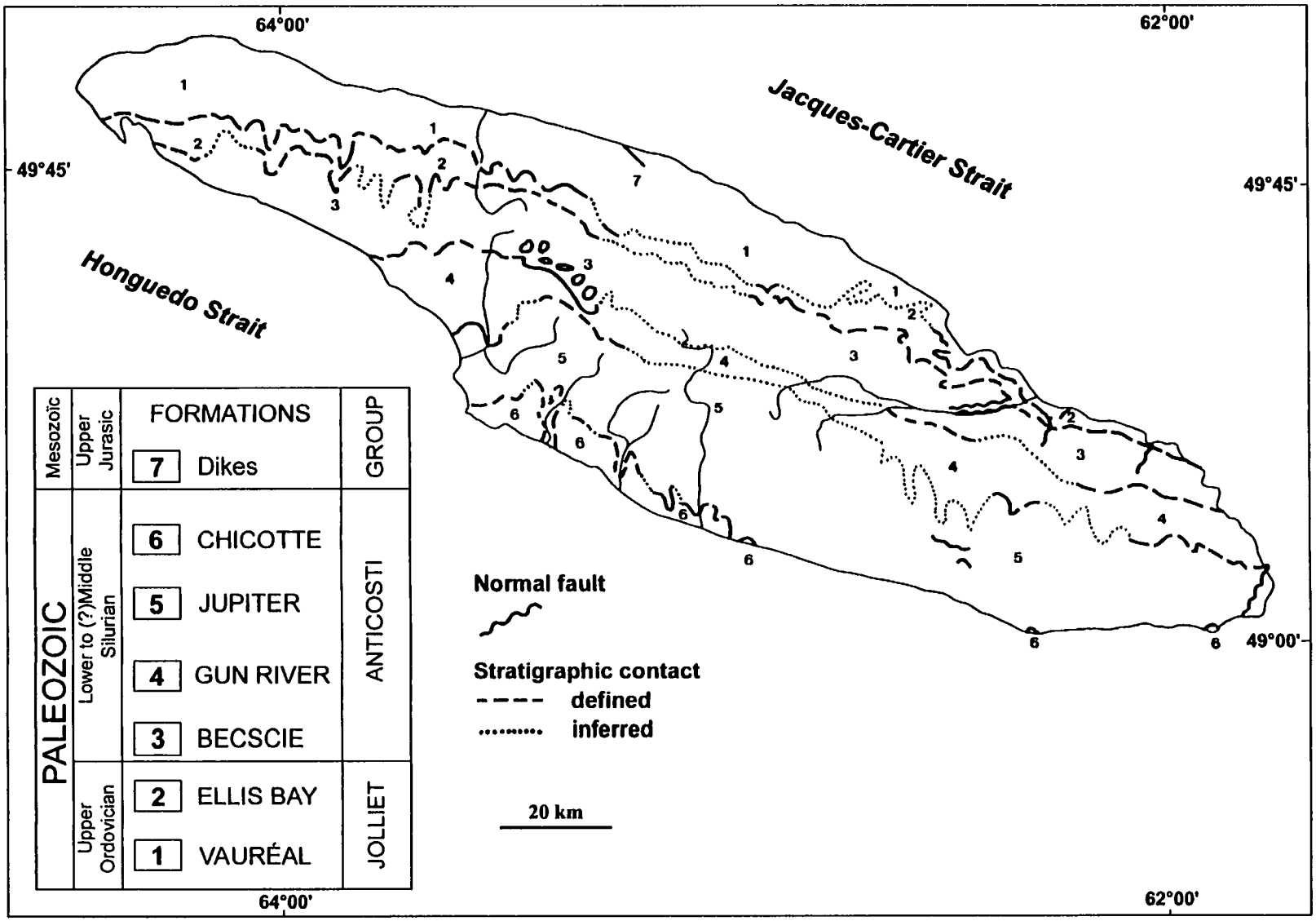
64°00'
62°00'
49°45'
49°00'
Jacques-Cartier Strait
Honguedo Strait
Normal fault
Stratigraphic contact
defined
inferred
20 km
PALEOZOIC
Mesozoïc
Upper Jurasic
Lower to (?)Middle Silurian
Upper Ordovician
FORMATIONS
7 Dikes
6 CHICOTTE
5 JUPITER
4 GUN RIVER
3 BECSCIE
2 ELLIS BAY
1 VAURÉAL
GROUP
ANTICOSTI
JOLLIET

unit located between the Becscie and Gun River formations, named the Merrimack Formation. From numerous field campaigns, they also succeeded to locate more precisely some of the formation contacts mapped by Petryk (1981b) and also to identify new formation members. Even with these latest modifications, nothing other than sketch maps with often-sparse details were presented (Figure 1-3), leaving the outdated geology map of Petryk (1981b) as the only one available today. For that reason, a need to produce a new geology map of Anticosti Island with its latest stratigraphic framework was felt necessary.

1.2.2 Complexity of Stratigraphic Mapping

Bio-stratigraphic and chrono-stratigraphic principles (grouping faunal zones according to evolution, variation, and extinction of species) based on close observations of outcrops are required to define appropriately stratigraphic successions. Identifying formation and member contacts within such succession requires, however, lithological observations that can result in inaccurate geology maps when conducted over vast territories densely vegetated. This is the case for Anticosti Island, since in addition to its vast territory (~8000 km^2) covered by a dense boreal forest and the lack of outcrops between its coast, rivers and few excavated roads, there is lateral lithological variations and noticeable changes in facies within its stratigraphic formations. Therefore, correlating the stratigraphic units across the island inevitably requires the synoptic view and additional terrain information that SAR remote sensing can provide.

Figure 1-3: Sketch map of the latest stratigraphic succession of Anticosti Island presented by Long and Copper (1994). Note the addition of the Merrimack Formation between the Becscie and Gun River formations.

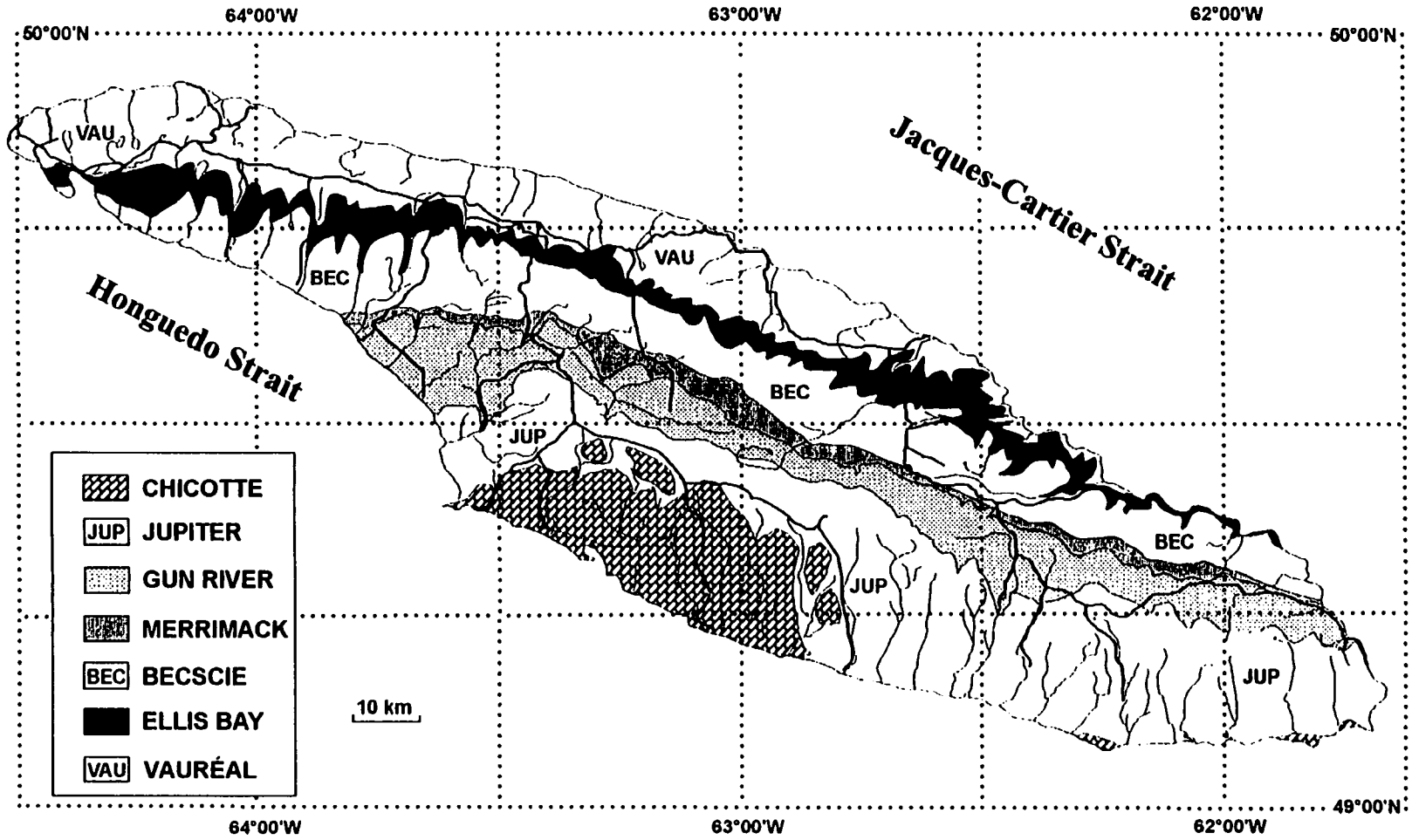
64°00'W
63°00'W
62°00'W
50°00'N
49°00'N
VAU
BEC
JUP
Honguedo Strait
Jacques-Cartier Strait
CHICOTTE
JUPITER
GUN RIVER
MERRIMACK
BECSCIE
ELLIS BAY
VAURÉAL
10 km

1.2.3 Limits of Traditional Photo-Interpretation

Air photos played a considerable role in understanding the geology of the island. *Imperial Oil Limited* and *Consolidated Paper Corporation* were among the first ones to conduct intensive geological interpretations based on air photos (Roliff, 1968). In 1975, over 400 air photos at a scale of 1:40 000 were acquired by the *Ministère des Terres et Forêts*, Québec, to support Petryk's geological mapping campaign (*Ministère des Terres et Forêts*, 1975). The same air photo database served in the automatic extraction of structural lineaments based on digital image analysis carried on by Tanguay *et al.* (1988) and by Carboni (1988). Geomorphologic studies dealing with the karst environment (Côté *et al.*, 1990; Paré, 2000), the coastal platform (Nadeau *et al.*, 1985), and the deglaciation of the island (Painchaud *et al.*, 1984) were also conducted using small-scale air photos.

Satellite optical images, such as Landsat-TM and SPOT-HRV images, were also considered for Anticosti Island, but mostly to map its surficial geology. Perras *et al.* (1985) have successfully demonstrated that the classification of Landsat TM data can be used to separate zones of strong and weak chlorophyll signatures and therefore discriminate vegetation from bare rock surfaces. From similar land cover classifications, Dubois *et al.* (1990) produced and published a 1:250 000 surface geology map (Figure 1-4) showing the various types of surface deposits, geomorphologic, and karstic features present on the whole island.

Figure 1-4: Simplified version of the surficial geology map of Dubois *et al.* (1990). The bedrock extent (*in pink*) represents 60 % of the island area whereas the Quaternary deposits are mostly restricted to river valleys and along the coast below the 150 m of altitude.

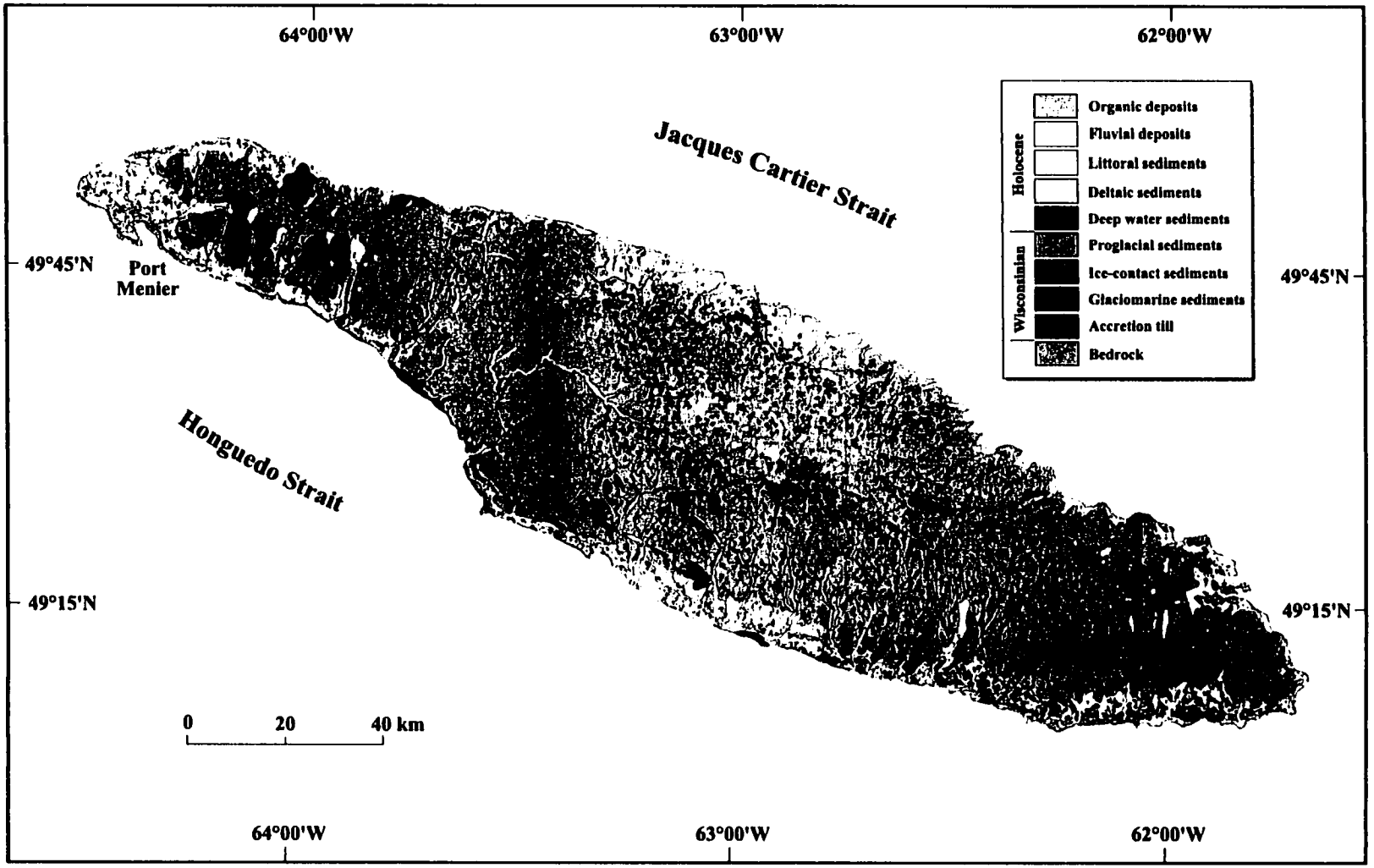
64°00'W
63°00'W
62°00'W
49°45'N
49°15'N
Port
Menier
Jacques Cartier Strait
Honguedo Strait
Holocene
Wisconsinian
Organic deposits
Fluvial deposits
Littoral sediments
Deltaic sediments
Deep water sediments
Proglacial sediments
Ice-contact sediments
Glaciomarine sediments
Accretion till
Bedrock
0
20
40 km

Unfortunately, the photo-interpretation of air photos and satellite optical images are not ideal to map the bedrock geology of forested areas since their responses are strongly influenced by the expression of the different surface albedo and therefore blinded by the high-frequency spatial details of the vegetation cover (Sabins, 1997). Also, the viewing geometry of most optical systems along with the constant depression angle of the solar illumination can be inadequate to enhance subtle topographic variations related to the bedrock geology. Consequently, considerable mapping uncertainty can result from the interpretation of optical remote sensing images over forested terrain.

1.3 Fundamentals and Potential of SAR Data

Neither satellite nor airborne SAR data were previously considered for mapping the distribution of the carbonate rocks of the densely forested Anticosti Island even though they have significant advantages over optical data. To appreciate these advantages, a description of radar principles and potential is presented here.

In comparison to optical systems, radar systems are not dependent on the reflection of the sunlight to image the surface of the earth. They are considered as active systems because they produce their own source of energy in the microwave portion of the electromagnetic spectrum. The microwave energy generated by radar systems is transmitted as pulses towards the surface of the earth where it interacts in various ways with the ground elements and then partially returns to the radar antenna mounted on an airborne or spaceborne platform

(Figure 1-5). The returning echoes are than recorded in a digital format for later processing and analysis (Raney, 1998).

The fundamental parameters affecting the radar backscatter are those associated with the radar system, the imaged terrain, and the inter-relationship existing between the system and the terrain parameters (Lewis *et al.*, 1998). The most important system parameters affecting the radar responses are 1) wavelength (or frequency), 2) incidence angle, 3) look direction, 4) ground resolution, and 5) polarisation. Parameters related to the terrain characteristics are 1) dielectric constant (soil moisture), 2) surface roughness, and 3) surface morphology and composition. Examples of inter-related system and terrain parameters will be given while describing each parameter individually in the following two sections. Despite their complexity, understanding the function and the role of inter-related parameters along with the individual system and terrain parameters are essential to properly interpret and analyse SAR data.

1.3.1 System Parameters

In this present study, the Convair-580 SAR data (fully described in section 3.1 on *Data Description*) were acquired over Anticosti Island in C-band wavelength mode. That C-band wavelength is equivalent to 5.66 cm or 5.30 GHz of frequency and can image the surface of the earth day or night and independently of the weather conditions. It turned out to be ideal for Anticosti Island since cloud cover and fog can prevail for days over that particular region.

Figure 1-5: The principle of radar energy interacting with ground targets and resulting in various backscatter responses. Taken from Sabins (1997).

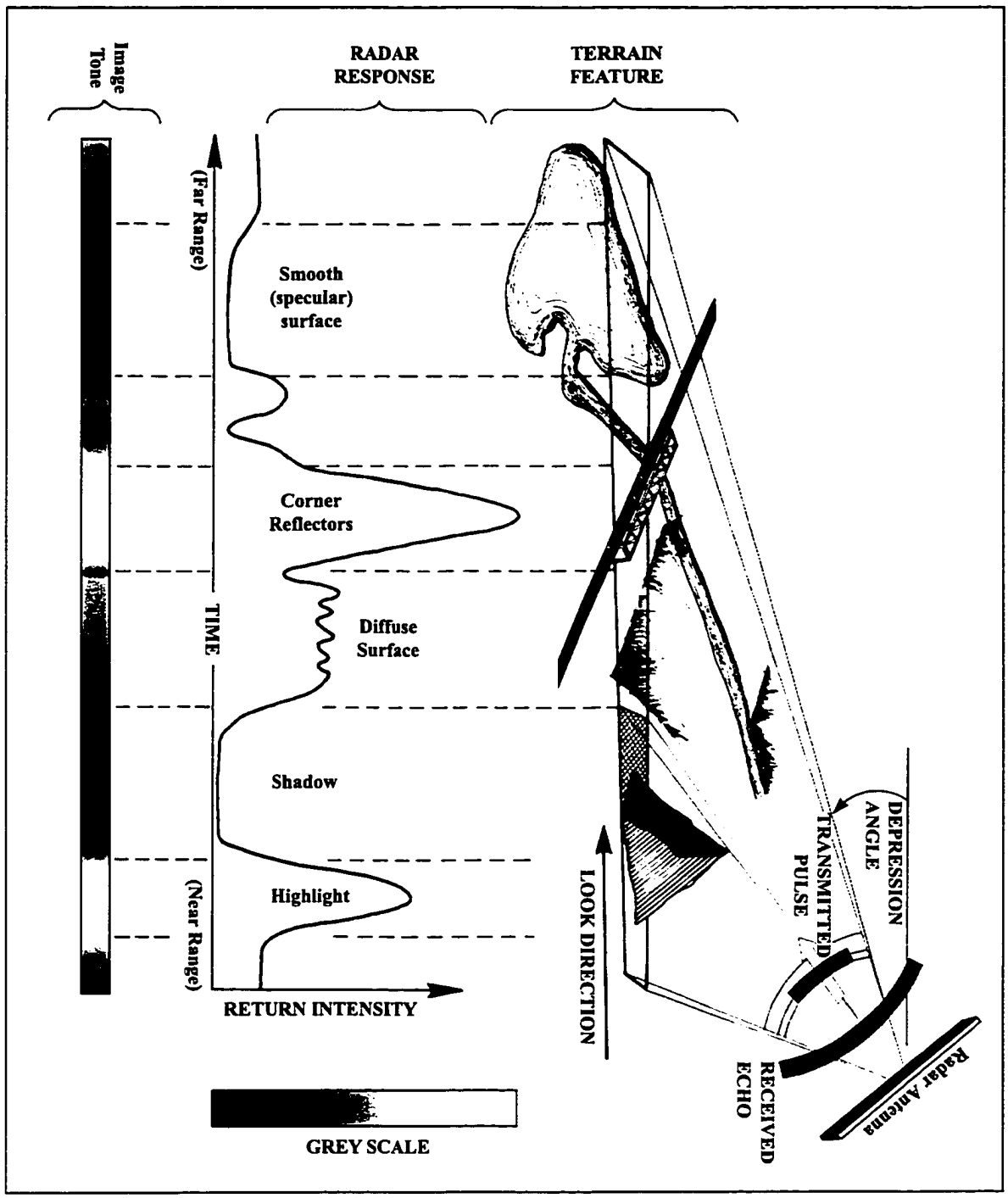
Image Tone
RADAR RESPONSE
TERRAIN FEATURE
(Far Range)
Smooth (specular) surface
Corner Reflectors
Diffuse Surface
Shadow
Highlight
(Near Range)
TIME
RETURN INTENSITY
GREY SCALE
LOOK DIRECTION
DEPRESSION ANGLE
TRANSMITTED PULSE
RECEIVED ECHO
Radar Antenna

Wavelength also plays an important role in defining the surface roughness, the penetration of radar into multiple layers of vegetation and soil, as well as the azimuth resolution of the SAR system (Lewis *et al.*, 1998). In general, the longer the wavelength is, the rougher a surface needs to be before it is recognised as rough, the deeper will be the radar penetration, and the greater the separation distance between ground elements needs to be before they can be resolved. With C-band wavelength, surfaces are considered rough when ground variations exceed only a few centimetres and radar signal rapidly saturates within the forest canopy reducing its penetration capability. The azimuth resolution of the C-band SAR data varies accordingly to the viewing geometry and altitude of the platform. The appearance of the surface elements on Anticosti Island is therefore largely dependent on the C-band wavelength of the Convair-580 SAR system.

The incidence angle (complementary to the depression angle when the ground surface is considered horizontal) is another important system parameter influencing the radar backscatter, thus the appearance of terrain features on intensity images. It is defined as the angle between the radar beam and a line perpendicular to the surface at the ground target. Coupled with the look direction of the radar system along with the orientation and the slope of the terrain features, the incidence angle determines if ground elements will produce radar highlights or shadows. Radar highlights and shadows are essential for geological interpretations since they can be used to measure dip-and-strike direction of inclined bedding. As described by Sabins (1997) and as illustrated in Figure 1-6, beds dipping toward

Figure 1-6: Highlight and shadow effects on bedding planes dipping away and towards the radar antenna. Taken from Sabins (1997).

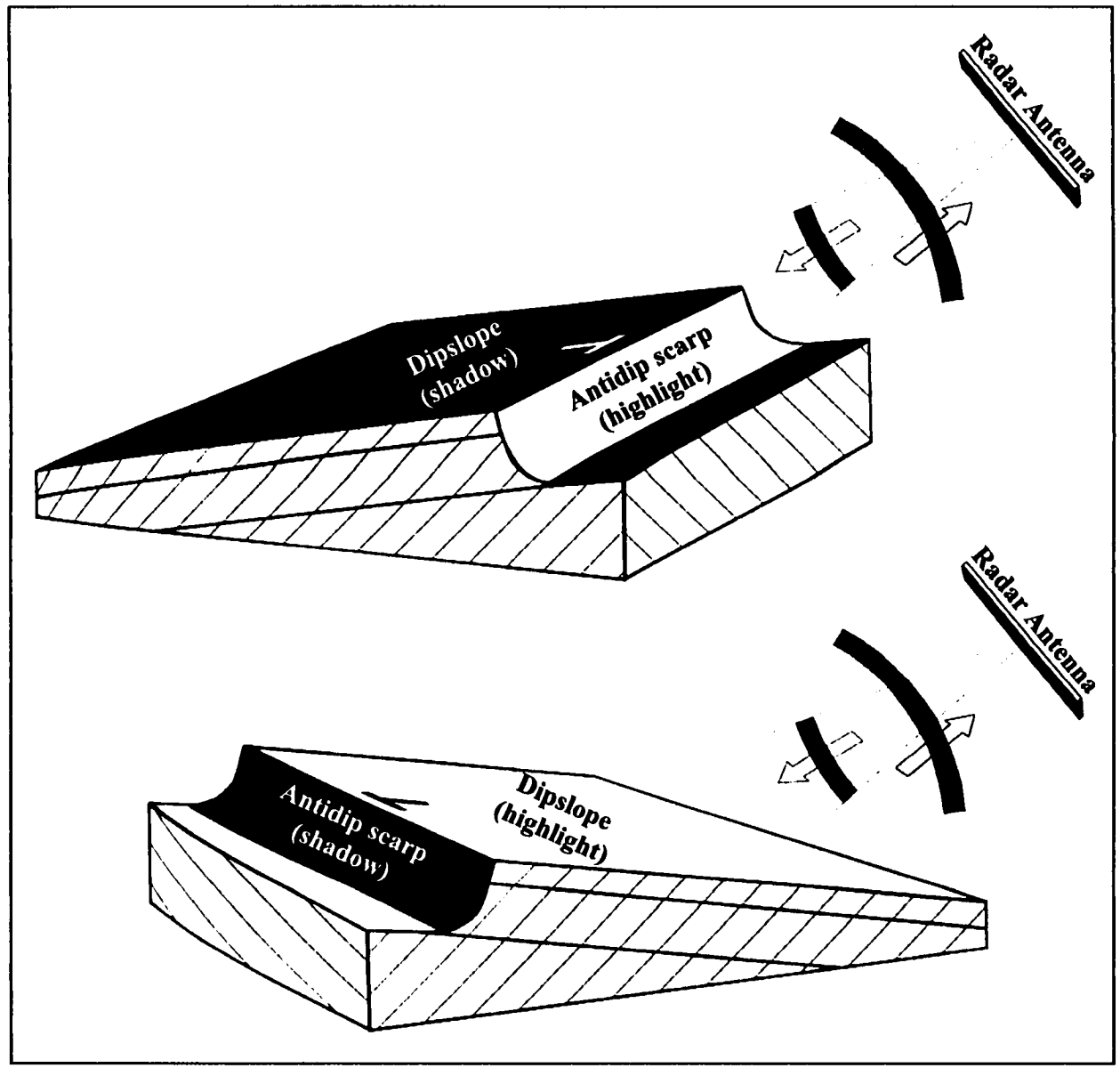
Radar Antenna
Dipslope
(shadow)
Antidip scarp
(highlight)
Radar Antenna
Antidip scarp
(shadow)
Dipslope
(highlight)

the radar antenna have highlights on the dipslopes and shadows on the antidip scarps whereas the inverse configuration of highlights and shadows on dipslopes and antidip scarps also happens for beds dipping away from the antenna.

The incidence angle of the SAR system on board of the Convair-580 aircraft can be as large as 85° in the far range (shallow depression angle) and as small as 0° at the nadir in the near range (steep depression angle). Such variation is possible because of the side-looking capability of the Convair-580 radar system, which allows the acquisition of SAR data in various swath geometries (Livingstone *et al.*, 1987 and 1995). Steep depression angles used over areas where pronounced terrain slopes exist can generate annoying geometric distortions such as radar foreshortening and layover along with the degradation of the range resolution (Blom *et al.*, 1987). Shallow depression angles are therefore preferred in order to avoid topographic distortions, but as a consequence the effect of radar shadow increases. Ideally, the selection of incidence angles should provide a minimum of radar distortions, but with sufficient radar highlights and shadows for proper geological interpretation.

Look-direction is another system parameter that can provide useful information for geological interpretation. Terrain features, especially those of linear geometry such as faults, joints, dykes, and scarp edges of inclined strata, can be enhanced or subdued depending on their orientation and the radar look-direction. The selection of an appropriate look-direction in accordance to the predominant features orientation is thus important in order to gain optimal illumination geometry valuable for geological mapping (Ford *et al.*, 1998). For that

particular reason, most flight lines covering Anticosti Island were acquired with a look-direction quasi perpendicular to the bedding planes in order to enhance with radar highlights and shadows the topographic relief associated with the bedrock geology and therefore facilitate the identification of the formation contacts.

Radar resolution is the system parameter that provides information on the size of the ground surface (resolution cell) with which the radar signal interacts. It also defines the separation distance required between ground elements so they can be resolved and displayed as individual features on radar images (Lewis *et al.*, 1998). Depending on the application, resolving individual features with fine resolution can be essential. However, such resolution over forested areas can prevent adequate geological interpretation. If individual trees were resolved, the overall topographic expression of the terrain along with some geological features would be hidden rather than enhanced due to the high-frequency spatial details coming out of the vegetation cover. The azimuth and range resolutions of 10 m and 20 m respectively (resampled to a common 15 m spatial resolution) of the C-band wide-swath SAR data are ideal to overlook the vegetation details and enhance the low-frequency topographic details associated to the bedrock geology underneath the vegetation cover. Consequently, the surface of the vegetation canopy mimicking the underlying bedrock topography is imaged as a whole and does not interfere in the geological interpretation. Figure 1-7, modified after Sabins (1997), shows how SAR can enhance topographic details associated with the structural geology of forested terrain.

Figure 1-7: The topographic enhancement of forested terrain with radar highlights and shadows. Taken from Sabins (1997).

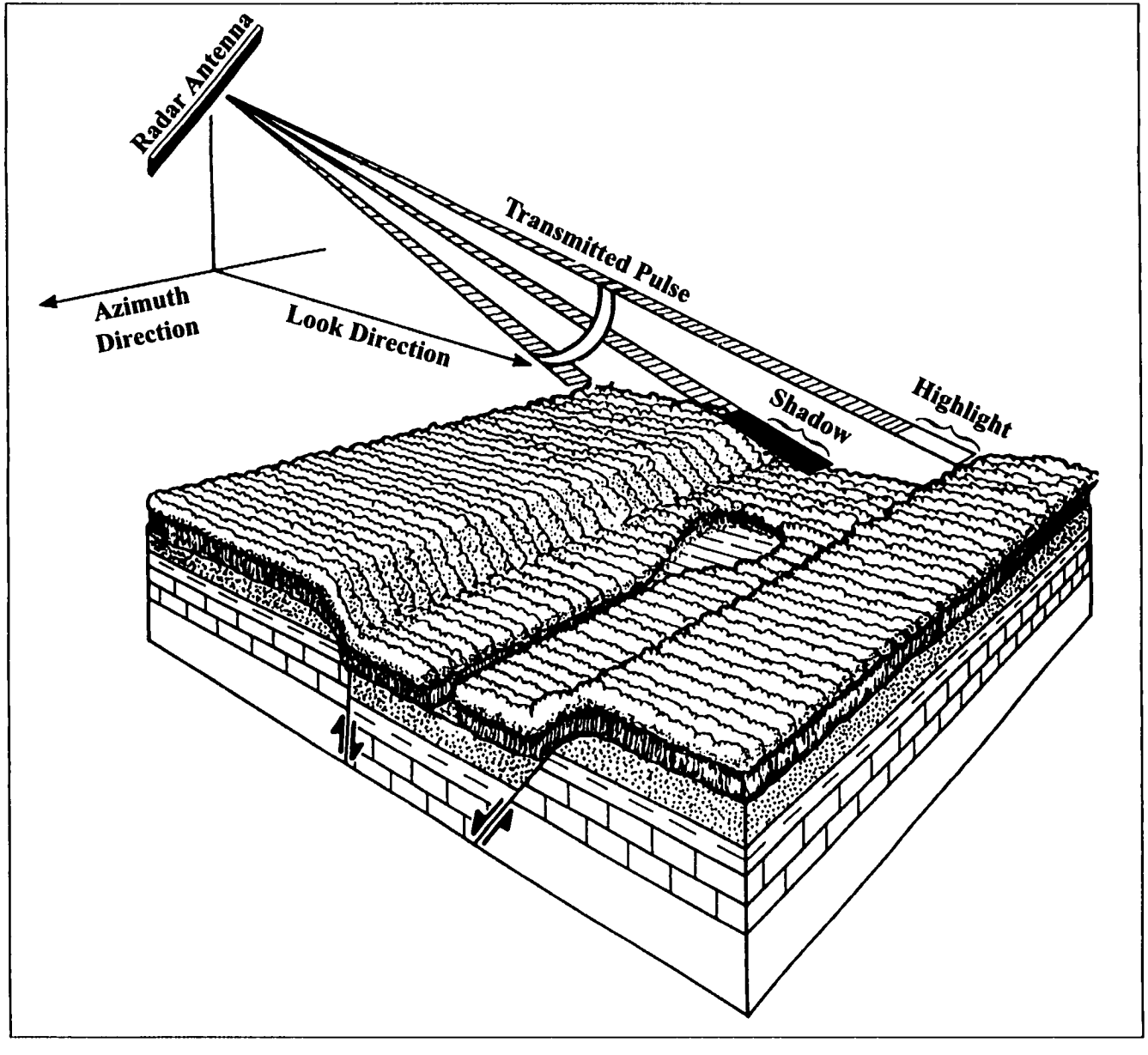
Radar Antenna
Transmitted Pulse
Azimuth Direction
Look Direction
Shadow
Highlight

Another system parameter affecting the radar backscatter is polarisation. Active radar systems have this capability of transmitting and receiving microwave energy in various polarimetric planes, which can be defined by the elliptical components of the electric field vector part of the electromagnetic radiation (Ulaby and Elachi, 1990; Boerner *et al.*, 1998; Zebker and Van Zyl, 1991). With amplitude and phase differences of the transmitted and the received polarisation, it is possible to extract useful information on the scattering mechanisms of the ground elements. For example, if the returning radar signal is seriously depolarised in comparison to the transmitted radiation, it may suggest that multiple volume scattering occurred within a heterogeneous cover. By pushing the polarimetric analysis, it might also be possible to distinguish the various types of elements within that heterogeneous cover. Such heterogeneous cover can be composed of multiple targets such as needles, leaves, stalks, twigs, and branches of trees within forest canopy or bushes and grasses part of the ground layer vegetation beneath the canopy. Specular reflection from smooth surfaces, multiple scattering from rough surfaces, and multiple volume scattering from heterogeneous vegetation or soil covers will result in various degrees of radar depolarisation that can be used to discriminate ground targets (Leckie and Ranson, 1998; Wu and Sader, 1986).

The Convair-580 SAR system allows the acquisition of radar data in fully (HH, HV, VH, and VV) or single-polarisation (HH, HV, VH or VV) modes for quantitative analysis. Fully polarised data are acquired when the microwave energy is transmitted and received simultaneously in all possible directions. The single polarimetric SAR data are, however, acquired when the radar energy is transmitted in one polarisation direction and received in

co- (HH or VV) or cross-polarisation (HV or VH). The analysis of fully polarimetric SAR data is far more complex than the interpretation of single polarimetric images because of the additional phase component to consider.

Most geological studies assisted by SAR polarisation have been conducted in arid and semi-arid environments (Blom *et al.*, 1987; Evans *et al.*, 1986 and 1988; Schaber *et al.*, 1997) and those conducted in regions of temperate climate were often inconclusive due to insufficient results (Rheault *et al.*, 1998; Saint-Jean *et al.*, 1999). A lot more work is required to fully understand the use of polarimetry for geology in forested areas, especially since Evans *et al.* (1986) have suggested that polarimetry has the potential to discriminate different geological units based on geo-botany principles, where certain species of plants and trees are sensitive to particular types of soil and rock. Perras *et al.* (1985) have also pointed out that the density of a forest cover could vary accordingly to the surface material. Surface deposits can block the joint and karst systems of bedrock, thus reducing the permeability of the soil and increasing its humidity. Consequently, certain vegetation species will favour those conditions while others will avoid them. Based on these statements, the fully polarimetric SAR data will be analysed to distinguish any preferential distribution of the vegetation cover with respect to the underlying surface deposits and bedrock geology and possibly determine if it can be used to assist geological mapping.

1.3.2 Terrain Parameters

The dielectric constant of ground targets is the most important terrain parameter influencing the radar backscatter. Moisture content of materials such as vegetation and soil controls the dielectric property of the terrain by influencing the absorption and propagation of electromagnetic radiation interacting with it. As moisture content increases, the dielectric constant increases as well and produces a strong radar return, which is recorded as a bright response on the intensity images. Furthermore, increasing the amount of moisture in ground material reduces radar penetration beneath the surface and through the vegetation canopy. The moisture content of the vegetation cover and the soil layer on Anticosti Island during each SAR acquisition was relatively normal and since no differences in the dielectric constant existed between the various terrain elements (with the exception of the water bodies and the wetland areas), other terrain parameters should be considered in order to understand the cause of the radar responses.

Surface roughness is the second most important terrain parameter influencing the backscatter response of SAR data. As suggested by Morain (1976) and later redefined by Lewis *et al.* (1998), surface roughness can be characterized based on three levels of scale: 1) micro-, 2) meso-, and 3) macro-scale surface roughness. The micro-scale surface roughness occurs within a resolution cell projected on the ground as defined by the radar system parameters. The geometry and spatial arrangement of individual ground elements (such as coniferous trees and their branches, twigs, and needles) within a resolution cell define the surface

irregularities from which the radar energy interacts with to produce the backscatter responses recorded as image tones. It is not much the heterogeneity of the ground elements within a resolution cell that will determines the intensity of the backscatter response, but the magnitude of the surface irregularities generated by these ground elements. The micro-scale surface roughness can be subdivided into three categories: 1) smooth (specular), 2) intermediate (diffuse), and 3) rough surfaces (Figure 1-5). Smooth surfaces reflect almost entirely the microwave radiation, resulting in a minimum of scattered echoes towards the antenna and therefore as a dark image response. Intermediate surfaces reflect partially the incident radiation and scatter the remainder of it, whereas rough surfaces diffuse all radiation with a strong scattered component returning to the antenna. A bright radar response is therefore recorded on the intensity images over these rough surfaces. Since micro-scale roughness is wavelength and incidence angle dependent, different approaches were developed to measure the physical limit between smooth and rough surfaces. The Rayleigh criterion is probably the most common approach used in radar remote sensing to define smooth surfaces from rough surfaces (Sabins, 1997). According to the Rayleigh criterion a surface will be consider rough for C-band (5.66 cm) SAR energy when its micro-scale relief exceeds 1.0 cm at 45° of incidence angle. Any changes of incidence angle or wavelength for that same ground surface will modify the limit between what was previously considered smooth and rough.

Meso-scale roughness is responsible for the textural appearance of intensity images (texture being a spatial variation of tones). It is related to changes in surface elevation and variability

of slopes in relation to the radar resolution. It is the result of spatial heterogeneity of ground elements on the order of a few resolution cells. Unlike the micro-scale surface roughness, the meso-scale roughness does not influence directly the ground interaction of the radar energy, but rather the appearance of the backscatter responses when adjacent resolution cells are taken all together. The backscatter responses associated to the micro-scale and meso-scale surface roughness in this study are not expected to vary much because of the similarity of ground elements within a resolution cell and also between adjacent resolution cells due to the dense and homogeneous forest cover of Anticosti Island.

Macro-scale roughness, however, is perfect for the geological interpretation of radar images over forested areas because it is several times larger than the resolution cell of the radar system and therefore more sensitive to regional topography. The backscatter responses associated to the macro-scale surface roughness are somewhat independent to the forest cover. Because regional topography could be accentuated by radar highlights and shadows, macro-scale roughness can provide essential information on the topographic relief of a region, which is often related to structural and lithological characteristics of the underlying bedrock geology.

Finally, the last terrain parameters affecting radar backscatter is the surface morphology and its composition. Surface morphology is not the same as surface roughness, but includes terrain relief, slope, and the orientation of terrain features. On the other hand, the surface composition describes the type of soil, the vegetation species, the density, and the spatial

arrangement (spacing and heterogeneity) of these materials. All these terrain characteristics have significant impact on how the C-band SAR energy interacts with surface elements on Anticosti Island.

1.3.3 SAR Mapping Potential

Selecting the proper system parameters in accordance to the various terrain parameters allow extracting valuable terrain information from SAR data for geological mapping. The mapping potential of C-band SAR data over the densely forested Anticosti Island is considerable even though there is a minimum of radar interaction with its underlying bedrock geology. There is certainly a rapid saturation of the radar signal within the forest canopy of the island, but its relatively uniform height, controlled by the environmental dynamic of the boreal forest, mimics the topographic relief and does not prevent side-looking SAR data to enhance with highlight and shadow effects the subtle topographic features associated with its structural geology. Mapping the island lithology is also possible based on these same principles since the lithological contrast between the resistant and recessive units allowed weathering process to erode in stair-stepped bedrock topography (cuesta morphology) its gently dipping stratigraphy. The detection by SAR data of that particular morphology can be used to locate and trace precisely the formation contacts associated to noticeable litho-facies changes, thus to distinctive topographic marker beds. Consequently, the macro-scale topographic sensitivity of the SAR data provides geologists with valuable topographic information for geological mapping.

2. Description of the Study Area

2.1 Geographic Location and Physical Environment of Anticosti Island

Anticosti Island is located to the northeast of the Gulf of St. Lawrence (Figure 1-1). It is precisely centred at latitude 49°30' North and longitude 63°00' West between the Gaspé Peninsula and the North Shore of Québec. The island has a total surface of 7925 km^2 with dimensions at its longest and widest points of 222 km and 56 km respectively.

The relief of Anticosti is relatively flat, but can be better described by its rolling topography closely related to its cuesta morphology nicely developed on both island extremities. Its maximum elevation is 306 m and corresponds to a gigantic cuesta front located near the centre of the island. That area is also referred to as the central plateau and is surrounded by lowlands rarely exceeding 150 m in altitude (Roberge, 1996). The central plateau, along with its cuesta, is an important geomorphologic element on the island since it controls the aspect of the various hydrographic basins prevailing in that sector. For example, rivers on the north side of the central plateau flow to the north and tend to be shorter and deeper enclosed in the bedrock compared to these flowing on its south slope, which are longer and less enclosed in the bedrock. That relationship is also attributable to the fact that the northern rivers are flowing in the opposite direction to the dip slope and cutting across the bedding planes whereas the southern rivers are flowing in the same direction as the dip of the bedding planes.

The few brittle structures present in the bedrock geology have also influenced the aspect of the island drainage since many river valleys almost parallel to each other are most likely controlled by fault/joint systems. While some river patterns are dendritic, others have developed a quasi-rectangular pattern controlled by these brittle structures. Several lakes are present on the island and their shapes are often resulting from clusters of sinkholes. These sinkholes are parts of a well-developed karst network resulting from chemical weathering of the carbonate rocks accentuated by the presence of joints (fractures) in the bedrock (Côté *et al.*, 1990; Lauriol *et al.*, 1985; Paré, 2000, Roberge, 1996). Within the surroundings of lakes, there are often ombrotrophic bogs[2] and minerotrophic fens[3] with extensive peat deposits. Their greatest concentration is in the eastern end of the island as well as in the northeastern corner of the Anticosti central plateau.

In terms of climate, the island belongs to a region of temperate and cold weather comparable to the Maritimes. A usual summer on Anticosti Island is short, but relatively warm. It begins in late May and ends in August, with maximum daily temperature in July at 15°C on average. The winters are long, but not too cold. The snow starts to fall in October with an average of 300 mm throughout the season. The minimum daily temperatures are in January at -10°C on average. The annual average temperature is about 2°C (Roberge, 1996). The island is often surrounded by fog, which has been responsible in the past for many shipwrecks along its treacherous coast (MacKay, 1979).

[2] *Peatland fed exclusively by precipitation and therefore acid and low in nutrients.*

[3] *Peatland with the water-table usually at or a few centimetres above or below the surface.*

2.2 Vegetation Cover

Coniferous trees dominate the dense boreal forest of Anticosti Island (Figure 2-1). The balsam fir (*Abies balsamea*), the white spruce (*Picea glauca*), and the black spruce (*Picea mariana*) are the predominant species and can be found in unmixed and dense forest stands in the interior and along the northern coastal area of the island (Roberge, 1996). In mixed stands, however, the paper birch (*Betula papyrifera*) is dominantly present with other tree species such as the eastern larch (*Larix laricina*) in wetland areas, the trembling aspen (*Populus tremuloides*), and the balsam poplar (*Populus balsamifera*) in burned sites and clear-cut areas (Lavoie and Filion, 2001). The ground layer vegetation is composed of a variety of herbaceous species that can be subdivided into two categories: 1) the wet herbaceous vegetation, and 2) the dry herbaceous vegetation (Roberge, 1996). The wet herbaceous vegetation is often associated to topographic depressions where minerotrophic fens prevails as well as swamps, marshes, and lakes (Figure 2-2a). The dry herbaceous vegetation, however, prefers ombrotrophic bogs where higher grounds exist, but can also be found in areas of open forest (Figure 2-2b).

It was estimated that over 30 % of the Anticosti forest was significantly disturbed in the past century by logging activities, fires, and insect outbreaks (Lavoie and Filion, 2001). It is the logging activities, however, that contributed the most in the past hundred years to the forest perturbation. Fires and insect outbreaks are more sporadic, but when uncontrolled they can

Figure 2-1: Field pictures showing the boreal forest of coniferous predominance present throughout the Anticosti territory:

(A) perspective view of the dense forest canopy where no ground surface can be detected;
(B) forest canopy mimicking the cuesta morphology of the island (*in background*);
(C) dense forest cover also present all around the coast.

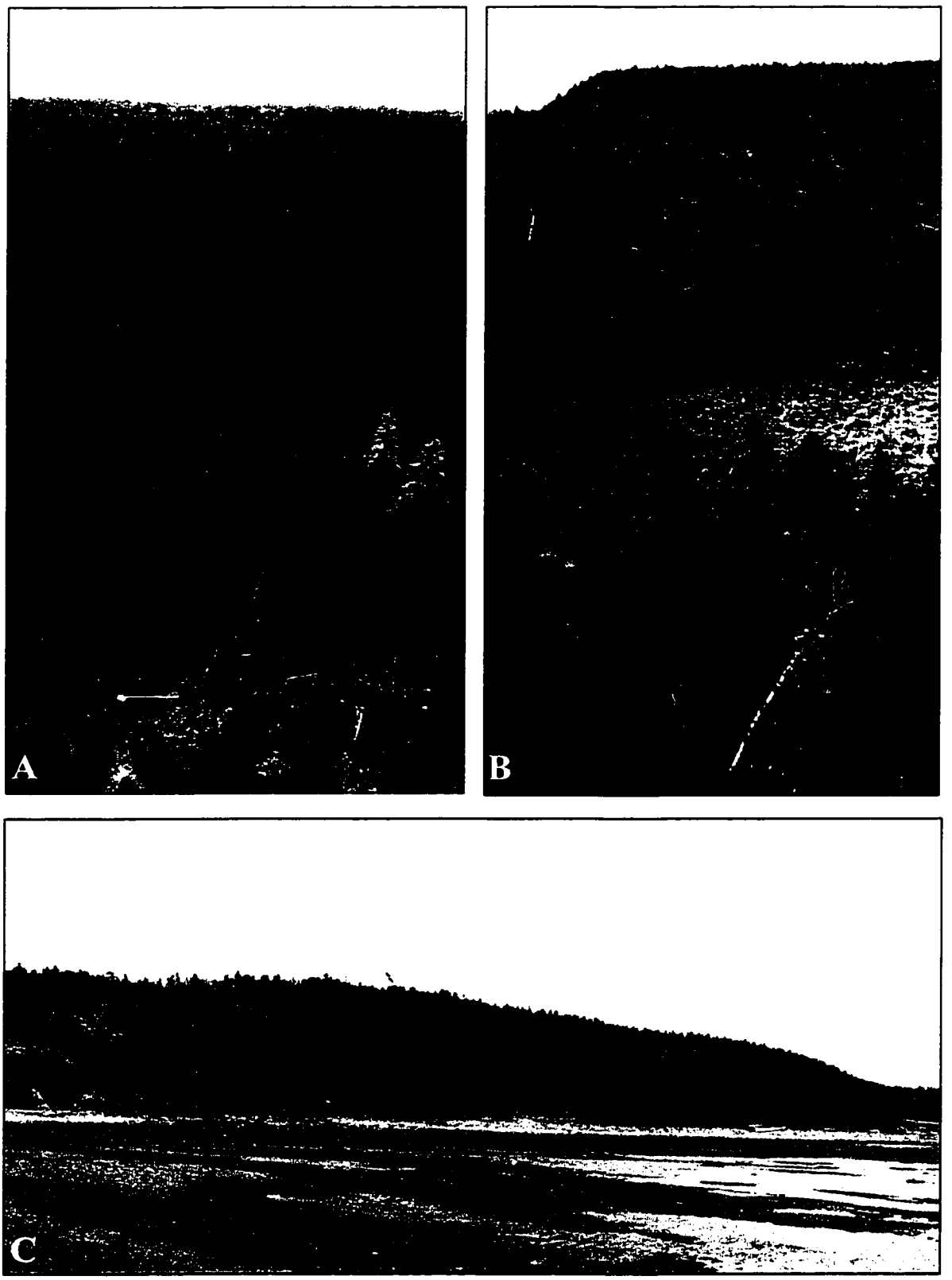
A
B
C

Figure 2-2: Field pictures showing the two types of herbaceous vegetation present on Anticosti Island:

(A) wet herbaceous vegetation in minerotrophic fens often associated with topographic depressions (due to soft-weathering strata) located in front of cuesta ridges (near Cap-de-la-Table);
(B) dry herbaceous vegetation in areas of ombrotrophic bogs and open forest (northeast corner of the island central plateau).

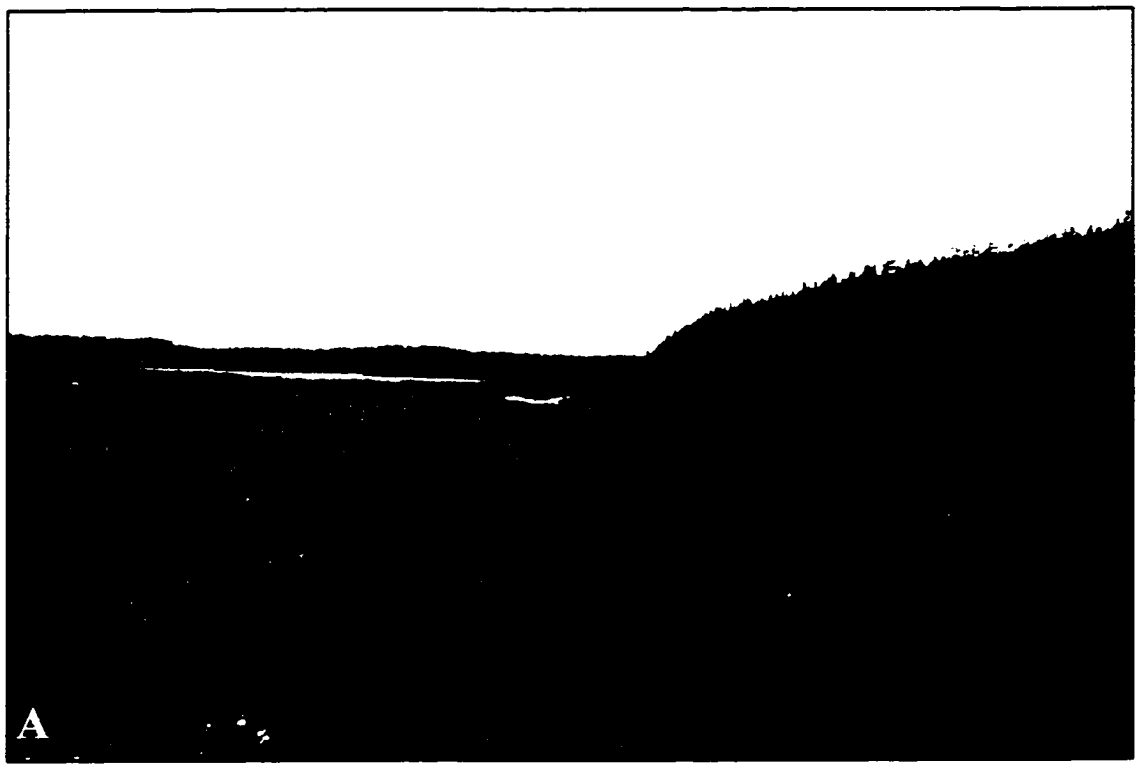
A

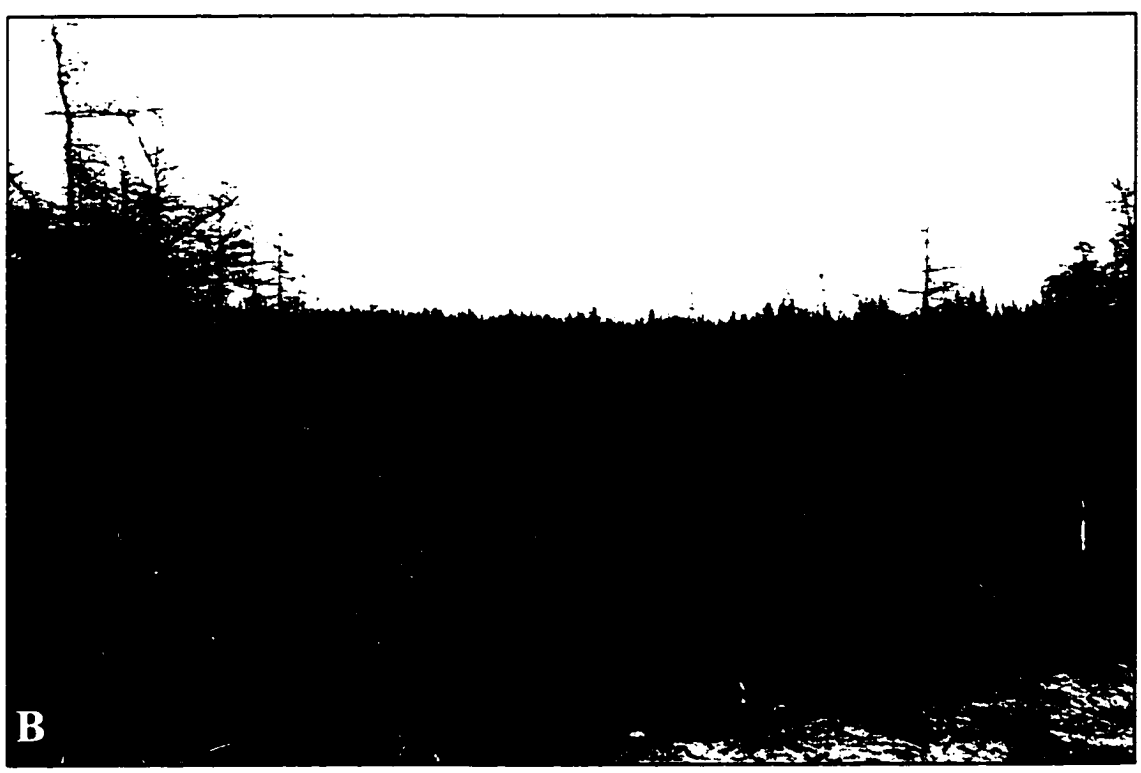
B

be the most ravaging. For example, nearly 8 % of the forest cover in the north central part of the island was destroyed by fire in 1955, without including the 1964 and 1983 fires that ravaged important stretches of forest in other sectors. Four major insect outbreaks occurred since 1925. The most important one was the hemlock looper (*Lambdina fiscellaria*) in 1971-1973 that killed 1400 km^2 of mature balsam fir stands in the south central part of the island (Lavoie and Filion, 2001). The white-tailed deer introduced in the island in the early century is another source of forest perturbation to consider since severe balsam fir browsing suppresses its regeneration permitting the white spruce to take over instead (Lavoie and Filion, 2001). Figure 2-3, adapted from a 1:250 000 map produced in 1992 by the *Ministère des Forêts du Québec, Direction de la Côte-Nord*, illustrates the extent of the principal forest stands along with the most important perturbations.

On a regional scale, the climate is certainly the most important factor that determines the distribution of vegetation cover, however, the natural and artificial perturbations along with the surface deposits, the hydrology, and the topography are all important factors that can influence local distribution. Understanding the terrain characteristics of Anticosti Island is therefore essential to appreciate the vegetation distribution and consequently the SAR responses.

Figure 2-3: Distribution of the principal forest stands along with associated perturbations. Adapted from a 1: 250 000 map produced in 1992 by the *Ministère des forêts du Québec, Direction de la Côte-Nord.*

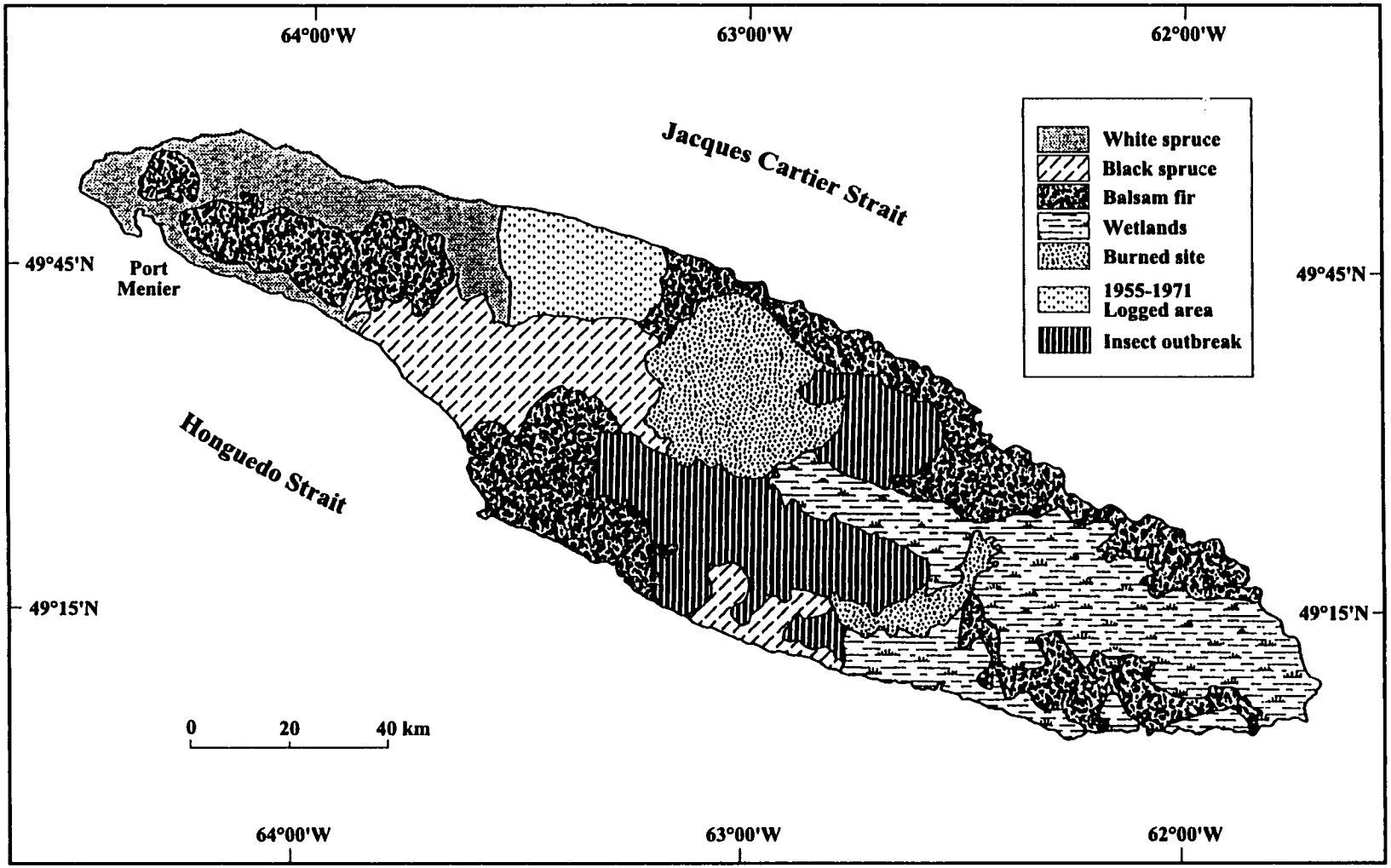
64°00'W
63°00'W
62°00'W
Jacques Cartier Strait
49°45'N
Port
Menier
Honguedo Strait
49°15'N
0
20
40 km
White spruce
Black spruce
Balsam fir
Wetlands
Burned site
1955-1971
Logged area
Insect outbreak

2.3 Surface Deposits

A relatively thin and discontinuous cover of Quaternary deposits is present above the Anticosti strata especially in the central plateau (Figure 1-4 and Figure 2-4a). The thickest superficial deposits can be found locally near the coastal areas or in river valleys below the 75 m of altitude (Painchaud *et al.*, 1984; Roberge, 1996). The Quaternary deposits are grouped into two major categories: 1) the glacial (Wisconsinian) deposits and 2) the post-glacial (Holocene) deposits, both described in Table 2-1, which was modified after Dubois *et al.* (1990) and Roberge (1996).

The few accumulations of glacial deposits are not contributing to the island topography and are barely masking its bedrock geology. The multiple Wisconsinian advances and retreats of the Laurentide ice sheet that have reached the Anticosti Island (Gratton *et al.*, 1984 and 1986; Painchaud *et al.*, 1984; St-Pierre *et al.*, 1987) have left almost no glacial deposits and fluvio-glacial erosion traces. Only a thin basal till and some thicker fluvio-glacial drift associated to constructional landforms such as morainic ridges, eskers, and kames are present locally (Figure 2-4b).

As illustrated in Figure 1-4, the surface geology map of Dubois *et al.* (1990), the most common Holocene deposits consist of organic materials (humus and peat) and of littoral sediments. The littoral sediments are restricted to the coastal areas whereas the relatively

Figure 2-4: Field pictures showing the thin and discontinuous organic soil and the glacial till resting on bedrock:

(A) thin organic layer resting directly on bedrock fragments (picture taken in the Gun River Formation near the western edge of Anticosti central plateau);
(B) thin organic soil resting on think stratified proglacial sediments near the Sainte-Marie moraine in the northwestern part of the island.


A


B

Table 2-1: List of the most common Quaternary deposits present on Anticosti Island. Modified after Dubois *et al.* (1990) and Roberge (1996).

QUATERNARY DEPOSITS		
HOLOCENE		
Unconsolidated Deposits		
	Organic Deposits	Humus and peat moss of 1 to 2 m of thickness mostly found in minerotrophic fens and ombrotrophic bogs.
	Fluvial Deposits	Gravely sand sediments of alluvial terraces exceeding rarely 2 m in thickness deposited by watercourses.
Marine Deposits		
	Littoral Sediments	A veneer of sandy gravels and pebbles up to 10 m in thickness covering the pediment.
	Deltaic Sediments	Stratified sandy gravels of 30 m of thickness up to 75 m of altitude in major river valleys.
	Deep Water Sediments	Not stratified clayey to sandy silts with few gravel lens that can reach up to 20 m of thickness and located near the coast under 90 m of altitude.
WISCONSINIAN		
Fluvioglacial Deposits		
	Proglacial Sediments	Stratified sandy gravel sometimes fossiliferous in outwash plains never exceeding 2 m in thickness.
	Ice-contact Sediments	Sandy limonitic gravels not stratified and of undefined thickness forming eskers, kames, and morainic ridges.
Glacial Deposits		
	Glaciomarine Sediments	Silts to clayey silts mixed with pebbly sands of 1 to 3 m of thickness mostly located in major valleys on the south side of the island not exceeding 70 m of altitude.
	Accretion Till	Poorly sorted unconsolidated silty to clayey glacial sediments in veneer of 1m of thickness in average.

thin organic deposits are present throughout the island, with the exception of the central plateau. The thickest organic deposits are located within topographic depressions between cuesta ridges and are often associated to minerotrophic fens (Figure 2-2a).

These Wisconsinian and Holocene deposits along with their associated constructional landforms have partly contributed to the radar responses acquired by the Convair-580 SAR system over the Anticosti Island. Understanding their spatial distribution will facilitate the image interpretation of the wide-swath SAR data and the quantitative analysis of the fully polarimetric SAR data conducted in this study.

2.4 Geological Context

The Lower Paleozoic continental margin of Laurentia in eastern Canada consists of the Québec Reentrant and the St. Lawrence Promontory (Figure 1-1). Aeromagnetic, gravity, and seismic reflection surveys have demonstrated that this margin sit on highly deformed, metamorphosed, and intruded Grenville Orogen rocks (Haworth and MacIntyre, 1977; Haworth, 1978; Hayward *et al.*, 2001; Séguin and Petryk, 1984). Along this margin Sloss's Sauk (Early Cambrian – Early Ordovician) and Tippecanoe (Middle Ordovician – Early Devonian) sequences are nicely recorded in various platforms/shelves and deeper marine settings. For the overall margin, the Sauk sequence is associated with the passive margin development whereas the Tippecanoe Sequence consists of the Tippecanoe I (Middle to Late Ordovician) and II (Early Silurian – Early Devonian) sub-sequence representing the

Taconian – Acadian foreland basins. The Upper Ordovician and Lower Silurian Anticosti succession is associated with a foreland basin (i.e. Tippecanoe succession) in the northeastern part of the continental margin, called the Anticosti Basin, where hydrocarbon potential has been suspected by Bertrand (1990), Nowlan and Barnes (1987), Roliff (1968), Sanford and Grant (1990), Sandford, 1998, and Williams (1973).

Few tectonic events have structurally affected the sedimentary platform of Anticosti. There has been the Precambrian basement uplift after the Acadian orogeny (Middle to Late Devonian) followed by the intrusion of diabase dikes outcropping on the island during the Jurassic Period (Bédard, 1992; Wanless and Stevens, 1971). The sedimentary platform was gently tilted to the southwest as a result of the basement uplift, allowing deeper erosion of its northern end to expose the metamorphic rocks of the Canadian Shield on the north shore of Québec and to preserve its lower Paleozoic strata on Anticosti Island.

2.5 Stratigraphic Succession

The Lower Paleozoic stratigraphic succession exposed on Anticosti Island is composed of approximately 900 m of Upper Ordovician (late Ashgill: from ca. 442 Ma to 439 Ma) and Lower Silurian (Llandovery: from ca. 439 Ma to 430 Ma) fossiliferous carbonate rocks (Copper and Jisuo, 1995; Desrochers *et al.*, 1998). The overall succession consists of shallow marine lime carbonates interbedded by minor calcareous shales, siliciclastic siltstones and sandstones being more common in the eastern part (Petryk, 1981a). It is the

most complete and exposed sequence in the world where no lithological break can be recognised at the Ordovician/Silurian boundary. That Ordovician/Silurian boundary was even considered by the Commission on Stratigraphic Classification of the International Union of Geological Sciences to represent a world stratotype (Barnes and McCraken, 1981; Barnes, 1988 and 1989; Lespérance, 1985; Petryk, 1981a).

Figure 2-5 and Table 2-2 were adapted after Copper and Jisuo (1995), Long and Copper (1994) and various discussions with Drs. D. Long and P. Copper[4] *(personal communication*, 1999 and 2001). They illustrate and provide a description of the stratigraphic subdivisions of the island succession as well as showing their thickness and relative weathering characteristics (recessive versus resistant units) according to the latest stratigraphic framework. The weathering profile of the composite section was subjectively generated based on the lithological properties of every member within each stratigraphic formation.

In the following section, each stratigraphic formation and their respective members are described according to the latest stratigraphic framework of Long and Copper (1994). The readers are referred to Long and Copper (1994) for additional information on the formations and their internal members and to Barnes (1989), Bolton (1970 and 1972), Copper (1981), Copper and Jisuo (1995), Copper and Long (1990), Desrochers *et al.* (1998), Duffield and Legault (1981), Fahraeus and Barnes (1981), Lespérance (1985), McCracken and Barnes

[4] *Department of Earth Sciences, Laurentian University, Sudbury, Ontario.*

Figure 2-5: Stratigraphic section of Anticosti Island adapted after Copper and Jisuo (1995) and Long and Copper (1994). Members in *italic* are informal.

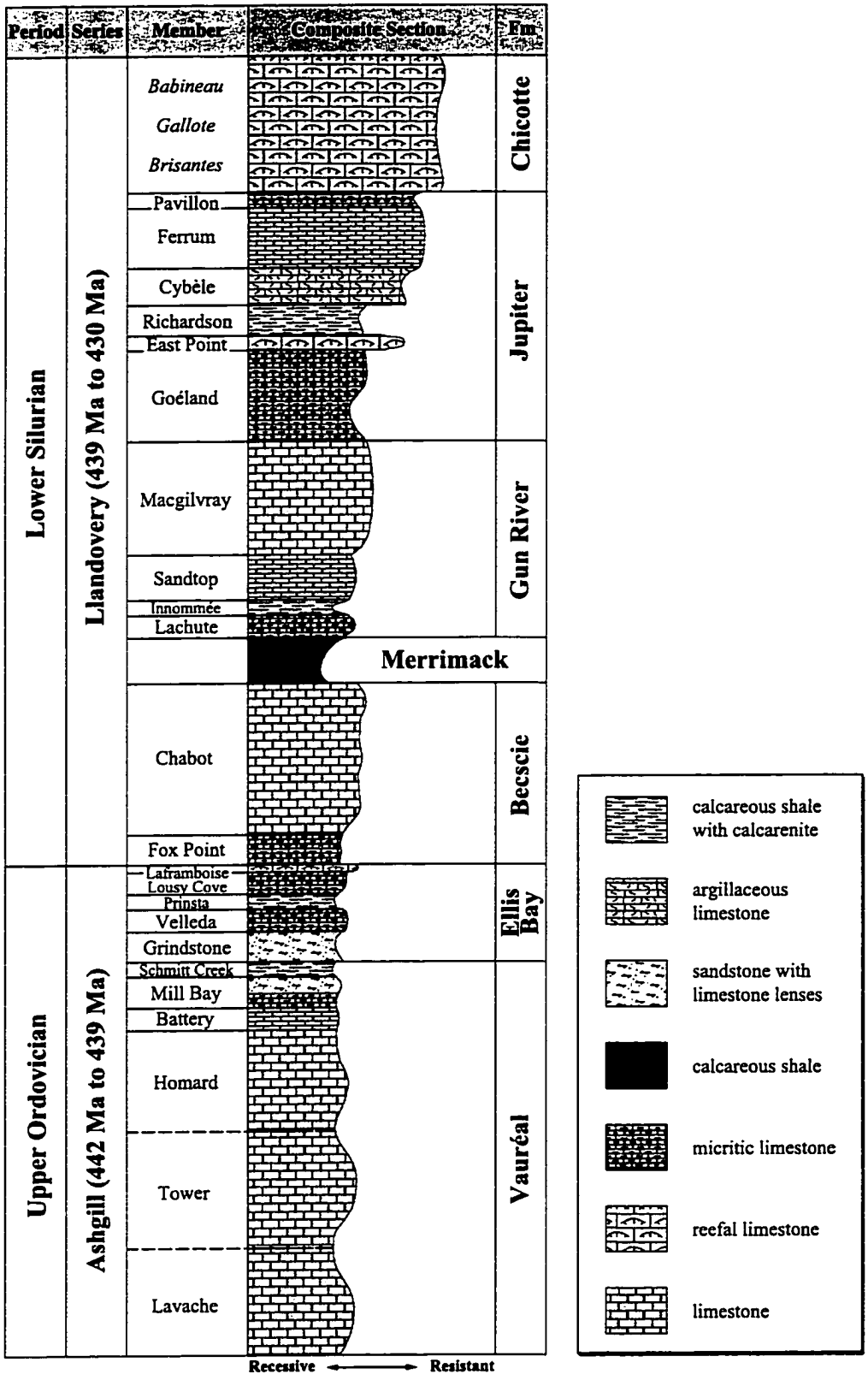
Period
Series
Member
Composite Section
Fm
Lower Silurian
Upper Ordovician
Llandovery (439 Ma to 430 Ma)
Ashgill (442 Ma to 439 Ma)
Babineau
Gallote
Brisantes
Pavillon
Ferrum
Cybèle
Richardson
East Point
Goéland
Macgilvray
Sandtop
Innommée
Lachute
Merrimack
Chabot
Fox Point
Laframboise
Lousy Cove
Prinsta
Velleda
Grindstone
Schmitt Creek
Mill Bay
Battery
Homard
Tower
Lavache
Chicotte
Jupiter
Gun River
Becscie
Ellis Bay
Vauréal
Recessive
Resistant
calcareous shale with calcarenite
argillaceous limestone
sandstone with limestone lenses
calcareous shale
micritic limestone
reefal limestone
limestone

Table 2-2: Description of the seven stratigraphic formations part of the island succession. Modified after Copper and Jisuo (1995), and Copper and Long (1994). Members in *italic* are informal.

ERA	PERIOD	SERIRES	SEQUENCES	MEMBERS	FORMATIONS	DESCRIPTION
Paleozoic	Lower Silurian	Llandovery (439 Ma to 430 Ma)	Tippecanoe II	*Babineau* *Gallote* *Brisantes*	**Chicotte** ± 90 m	Thick-bedded encrinites (limestone with >80 % of crinoid bioclasts) with bioherm horizons.
				Pavillon[1] Ferrum Cybèle Richardson[3] East Point[2] Goéland[1]	**Jupiter** ± 167 m	Calcareous mudstone, micrite, grainstone and minor intra-formational conglomerate. *(1)* Recessive weathering calcareous mudstones and micritic limestone; *(2)* Basal calcarenite overlain by massive bioherms; *(3)* Soft-weathering argillaceous limestone.
				Macgilvray[1] Sandtop Innommée Lachute[1]	**Gun River** ± 130 m	Rhythmic thin to thick calcarenite, rudite packstone to grainstone. *(1)* Resistant weathering massive micrites.
				Merrimack ± 30 m		Recessive weathering calcareous mudstones with minor micrites and calcarenites.
				Chabot[2] Fox Point[1]	**Becscie** ± 130 m	Micrite and calcarenite units. *(1)* Less resistant thin bedded micrite; *(2)* Weathering resistant grainstone to intraformational conglomerate.
	Upper Ordovician	Ashgill (442 Ma to 439 Ma)	Tippecanoe I	Laframboise[1] Lousy Cove[1] Prinsta Velleda[1] Grindstone	**Ellis Bay** ± 62 m	Carbonate-siliciclastic sandstone alternating with micritic limestones and calcareous mudstones. *(1)* Resistant members due to the presence of bioherms or fine to coarse sandstone units.
				Schmitt Creek[2] Mill Bay[1] Battery Homard Tower Lavache	**Vauréal** > 275 m	Interbedded micrite, calcarenite, rudite, and calcareous mudstone. *(1)* Resistant weathering coarse-grained sandstones; *(2)* Recessive weathering calcareous mudstones and muddy limestones.

(1981), Riva and Petryk (1981), and Twenhofel (1914 and 1928) for details on the formations bio- and chrono-stratigraphy.

2.5.1 Vauréal Formation (Upper Ordovician)

The actual thickness of the exposed Vauréal Formation is somewhat variable, but seems to range between 275 to 350 m, which makes it the thickest formation on the island. It consists of interbedded micrites, calcarenite rudites, and calcareous mudstones. Six members were recognised within that formation including from base to top the Lavache, Tower, Homard, Battery, Mill Bay, and Schmitt Creek members.

The lithology of these six members is very similar, especially for the Lavache, Tower, Homard, and Battery members. Their variation comes mostly from the interbedded siliciclastic content whereas the difference in the carbonate content is from the depositional texture (muddy versus coarser grained). These variations are, however, significant enough for the bedrock topography to be influenced by differential weathering and developed a stair-stepped morphology. The more massive sandstone beds, such as these encountered in the Mill Bay Member, are relatively more resistant than the laminated calcareous mudstone and muddy limestone beds of the Schmitt Creek Member, which can explain the presence of the resistant bulge below the lip of the Vauréal falls (Long and Copper, 1994).

2.5.2 Ellis Bay Formation (Upper Ordovician)

The Ellis Bay Formation consists of approximately 52 to 72 m of alternating argillaceous (relatively recessive) and less argillaceous (relatively resistant) units. It is lithologically the most variable formation on the island. Its easternmost strata are dominated by abundant mixed of micrites and carbonate-siliciclastic sandstones that are wedging up to the other end of the island to strata dominated by micritic limestones interbedded with calcareous mudstones.

Five members were recognised in the Ellis Bay Formation, which are in ascending order the Grindstone, Velleda, Prinsta, Lousy Cove, and Laframboise members. The Velleda, Lousy Cove, and Laframboise members are relatively more resistant than the Grindstone and Prinsta members because of the presence of coarse sandstone units or patches of small coral reefs (bioherms).

The lowermost Grindstone Member is slightly more resistant to weathering than the Schmitt Creek Member of the Vauréal Formation resulting in a minimum of topographic contrast between the two units. It consists of laminated thin beds of fine sandstones and calcareous mudstones to the east and laminated thin-bedded micrites interbedded with calcarenites with abundant bioturbation to the west. The uppermost Laframboise Member ranges between 0.5 and 8.0 m in thickness and consists of thin basal oncolitic «platform bed» as defined by Petryk (1981a). That oncolite rich bed is present throughout the island along with local

bioherms, which makes it a good stratigraphic marker. The top of the coral reef bed actually corresponds to the location of the Ordovician/Silurian boundary within the Anticosti succession (Barnes, 1988; Cocks and Copper, 1981; Copper, 1981 and 1989; Copper and Long, 1989; Long and Copper, 1994; Petryk, 1987). It is relatively more resistant than the underlying Lousy Cove Member within the Ellis Bay Formation or the basal Fox Point Member of the upper Becscie Formation.

2.5.3 Becscie Formation (Lower Silurian)

The first Lower Silurian formation on Anticosti Island overlying the Ordovician/Silurian boundary is the Becscie Formation. It consists of approximately 130m of limestone (mainly micrite and calcarenite) interbedded with minor shales. Two members have been recognised in the formation, which are the Fox Point and the Chabot members. The Fox Point Member is dominated by thin-bedded sets of micrite separated by thin siliciclastic rich carbonate mudstones. The weathering resistant Chabot Member is the thickest of the two members and is characterized by very fossiliferous grainstone and intraformational conglomerate units. (Copper and Jisuo,1995; Copeland and Bolton, 1975).

2.5.4 Merrimack Formation (Lower Silurian)

The 30 m thick Merrimack Formation consists of recessive weathering calcareous mudstones, with minor micrites and calcarenites. It is the thinner formation on the island with

no internal members due to its relatively homogeneous lithology. It is poorly exposed because of its soft weathering characteristic, but its topographic expression makes it easier to distinguish between the relatively more resistant strata of the adjacent formations.

2.5.5 Gun River Formation (Lower Silurian)

The Gun River Formation is up to 130 m thick and consists of rhythmic thin to thick calcarenite/rudite packstone to grainstone. Four members can be found in the Gun River Formation, which are the Lachute, Innommée, Sandtop, and Macgilvray members. The lowermost Lachute Member is composed of relatively hard-weathering, thin-bedded micrites with mudstone partings. Following the Lachute Member is the soft-weathering, thus poorly exposed, Innommée Member of less than 10 m of laminated calcareous mudstone. Finally, the uppermost Sandtop and Macgilvray members are relatively more resistant than their counterparts due to the presence of thicker beds of massive calcarenite/rudite with only thin sets of calcareous shales.

2.5.6 Jupiter Formation (Lower Silurian)

The Jupiter Formation has a total thickness of 167 m and consists of calcareous mudstone, micrite, grainstone and minor intraformational conglomerate. It has been divided into six members by Copper and Long (1990), including the Goéland, East Point, Richardson, Cybèle, Ferrum and Pavillon Members. The lowermost Goéland Member consists of soft-

weathering, calcareous mudstones and lesser interbedded micritic limestone and bioclastic grainstones. The East Point Member consists of basal calcarenite overlain by a massive lenticular biohermal unit. Lithologically, it is the more resistant unit within the Jupiter Formation. The Richardson Member is the less resistant unit with its argillaceous limestones and few micrite and calcarenite units. The Cybèle Member resembles that of the Gun River Formation as well as the upper Ferrum Member where no dominant limestone lithology prevails. Finally, at the top of the Jupiter Formation lies the Pavillon Member, which consists of recessive calcareous mudstone and interbedded micrite with discontinuous lenses of calcarenite.

2.5.7 Chicotte Formation (Lower Silurian)

The Chicotte Formation, exposed along the south-central and south-eastern coasts of Anticosti Island, consists predominantly of 90 m of massive to wavy, thick bedded, crinoidal grainstone. Three informal members were suggested by Brunton and Copper (1994) including the Brisantes, Gallote, and Babineau members, but with no particular lithological definitions. The Chicotte Formation is lithologically the most resistant of the whole island succession and its identification in the field is the easiest since abundant crinoid fragments representing over 80 % of its rock volume can be find everywhere. Clusters of coral reefs are also common in the formation and can reach up to 25 m in thickness and 250 m in diameter. At least two horizons of coral reefs were already recognised in the Chicotte Formation with a third one under investigation (Desrochers *et al.*, 1998).

2.6 Structural Geology

The monoclinal structure of the island is the result of a very gentle south-southwest dip (0.5° to 3°) associated with the sedimentary platform of Anticosti Island (Petryk, 1981b). This gentle dip is also responsible for the parallelism of the formation contacts, which are more or less trending in the same NW-SE direction as the longitudinal axis of the island. Only minor deformation structures such as normal faults, fractures (or joints), and local folds have been reported and mapped (Bolton, 1972; Desrochers *et al.*, 1997; Petryk, 1981b). Linear topographic features, such as elongated river valleys developed in a rectangular or parallelism pattern, are the result of those structural elements.

One of the most remarkable structural features on Anticosti Island is the diabase intrusion of Jurassic age originally recognised by Bédard, (1992), Bolton (1970), Larochelle (1971), Long and Copper (1994), Petryk (1981b), and Wanless and Stevens (1971) to cut only the Vauréal Formation (Figure 1-2). It is now known to cut at least five of the seven stratigraphic formations with the exception of the Jupiter and Chicotte formations for a distance no less than 40 km (Desrochers *et al.*, 1997). The two dykes, part of that intrusion, are outcropping only at the Puyjalon Cliff along the north central coast of the island.

3. Methodology

Two different approaches were considered in this study to evaluate the potential of the airborne C-band SAR data for mapping more precisely the geology of the densely forested Anticosti Island. The first approach consists of identifying and tracing every formation contact of the island succession by visually interpreting the intensity image derived from wide-swath, single polarimetric SAR data. The second approach consists of quantitatively discriminating the lithological formations of the island using fully polarimetric SAR data. Such discrimination is possible by considering the influence terrain characteristics have on the preferential distribution of vegetation and therefore on its polarimetric appearance. Both approaches are further described in sections 3.3 and 3.4 following the data description.

3.1 Airborne SAR Data Description

The airborne SAR data of Anticosti Island were acquired during three distinct flight missions with the SAR system on board of the Convair-580 aircraft (Figure 3-1a). The Convair-580 SAR system (Figure 3-1b and 3-1c) was originally developed by the CCRS, Natural Resources Canada, who maintained and operated it until 1996 (Livingstone *et al.*, 1987 and 1995). Since then, the Emergencies Science Division of Environment Canada owns, maintains, and operates the system. CCRS is, however, contributing in the maintenance and participate in its operation when needed.

Figure 3-1: Convair-580 aircraft and its SAR antennas (Livingstone *et al.*, 1995):

(A) picture of the Convair-580 aircraft showing the main C/X –SAR antenna radome mounted below its fuselage to the rear;
(B) illustration of the two antenna radomes part of the dual mode SAR system of the Convair-580;
(C) close-up of the rear end of the Convair-580 aircraft showing both SAR antennas with their protective radome removed;
(D) polarimetric active radar calibrator (PARC) and trihedral corner reflector (CR) devices used to calibrate radar signal.


CANADA

B

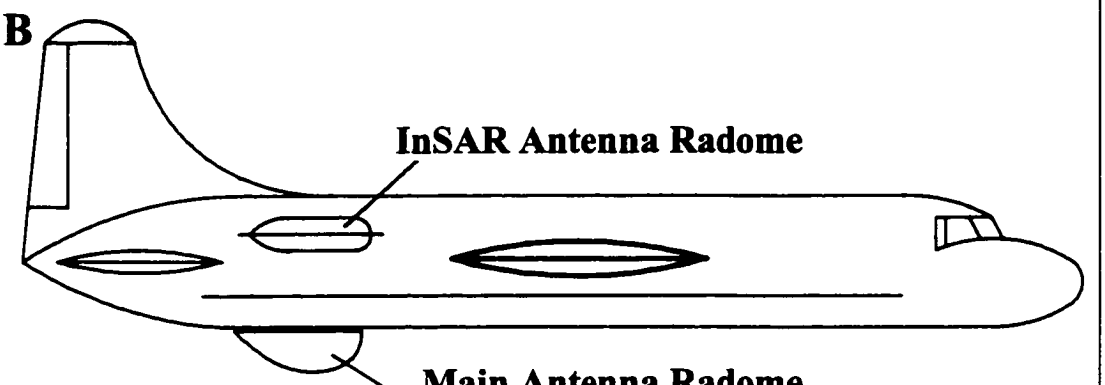
InSAR Antenna Radome
Main Antenna Radome
(C/X-SAR)


DANGER
RADIATION

C

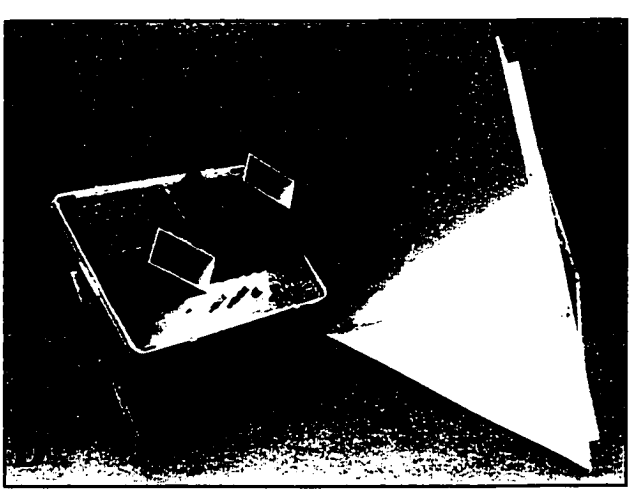

The acquisition of the various SAR flight lines over Anticosti Island would have been impossible without the valuable financial and logistic support provided by CCRS.

3.1.1 SAR Data Acquisition

The first SAR acquisition over Anticosti Island took place in the fall of 1991 during a radar mission conducted by CCRS in the Atlantic region. Even though no specific pre-flight planning was prepared for Anticosti, the SAR acquisition turned out to be successful and the data of high quality. Only one flight line parallel to the longitudinal axis of the island and with a NNE look-direction was acquired in a wide-swath configuration and in a single polarisation (HH) mode as illustrated in Figure 3.2a and listed in Table 3-1. It is on these particular SAR data converted into an intensity image that the geological interpretation was conducted.

Five new flight lines with a special narrow-swath configuration (Figure 3.2b) were acquired in November 1998 and April 2000 in a fully polarimetric mode (HH, HV, VH, and VV) in addition to the wide-swath data. Table 3-1 lists the characteristics of these new flight lines whereas Figure 3-3 shows their distribution with respect to the 1991 acquisition. They were all considered for the polarimetric analysis, but due to constraints only the 1998 *L4P3* flight line was used.

Figure 3-2: The two most common operating geometries for land applications with the Convair-580 SAR system (taken from Livingstone *et al.*, 1995):

(A) wide-swath mode providing low resolution (20 m x 10 m) imagery with shallow incidence angles varying from 44° to 85° to maximize the area of coverage (63 km);

(B) special narrow-swath mode providing high resolution (6 m x 6 m) imagery with steeper incidence angles ranging from 36° to 67° in the near range ideal for fully polarimetric SAR acquisitions.

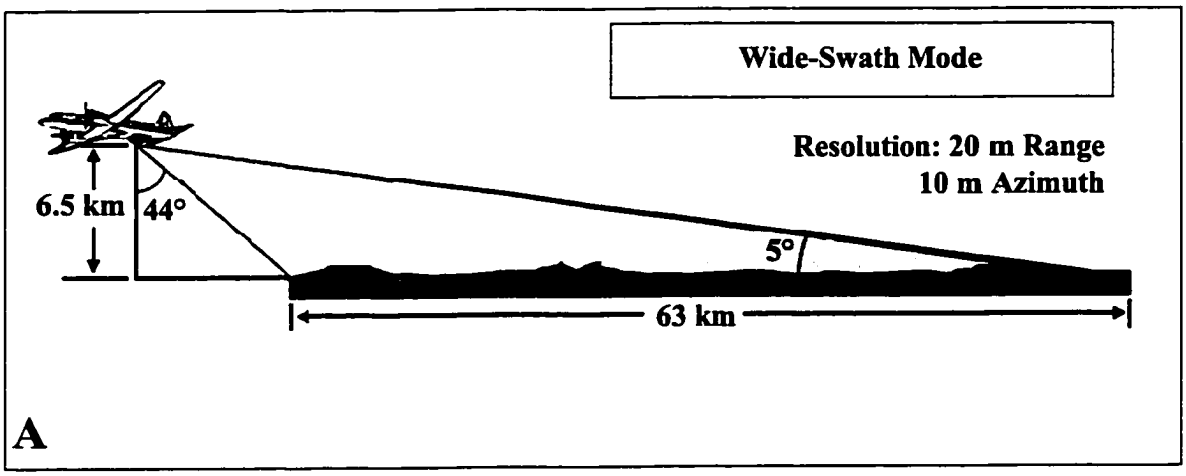
Wide-Swath Mode
Resolution: 20 m Range
10 m Azimuth
6.5 km
44°
5°
63 km
A

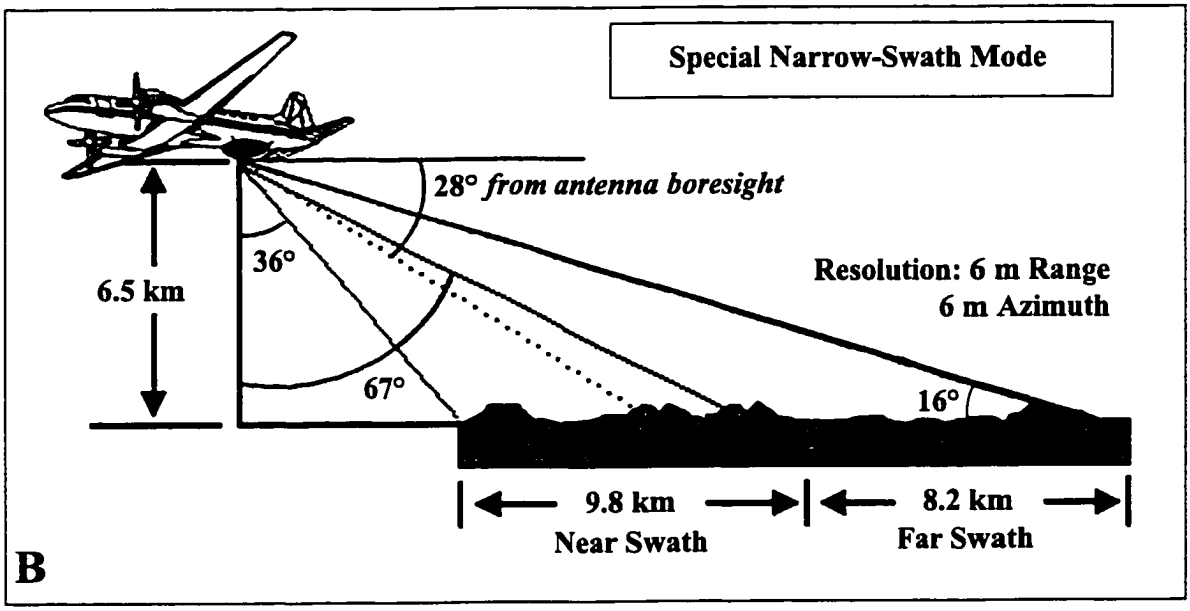
Special Narrow-Swath Mode
28° from antenna boresight
Resolution: 6 m Range
6 m Azimuth
6.5 km
36°
67°
16°
9.8 km
Near Swath
8.2 km
Far Swath
B

Table 3-1: Characteristics of the various SAR flight lines acquired over Anticosti Island.

	L1P1	L4P3	L7P2	L2P4	L1P2	L2P1
Acquisition Date	29-nov-91	22-Nov-98	22-Nov-98	22-Nov-98	01-Apr-00	01-Apr-00
Viewing Geometry	Wide Swath	Narrow Swath	Narrow Swath	Narrow Swath	Narrow Swath	Narrow Swath
Azimuth Range Resolution	20 m	6 m	6 m	6 m	6 m	6 m
Ground Range Resolution	10 m	6 m	6 m	6 m	6 m	6 m
Pixel Spacing (Range)	15.54 m	4.88 m	4.88 m	4.88 m	4.88 m	4.88 m
Line Spacing (Azimuth)	6.90 m	3.89 m	3.89 m	3.89 m	3.89 m	3.89 m
Incidence Angle Range	44° - 85°	36° - 67°	36° - 67°	36° - 67°	36° - 67°	36° - 67°
Polarization Mode	HH	HH-HV VH-VV	HH-HV VH-VV	HH-HV VH-VV	HH-HV VH-VV	HH-HV VH-VV
Flight Line Direction	93°	280°	286°	107°	180°	135°
Look Direction	3°	370°	376°	197°	270°	225°
Number of Looks	7	7	7	7	7	7

Figure 3-3: Distribution of the 1998 and 2000 fully polarimetric SAR flight lines in relationship to the 1991 wide-swath SAR image.

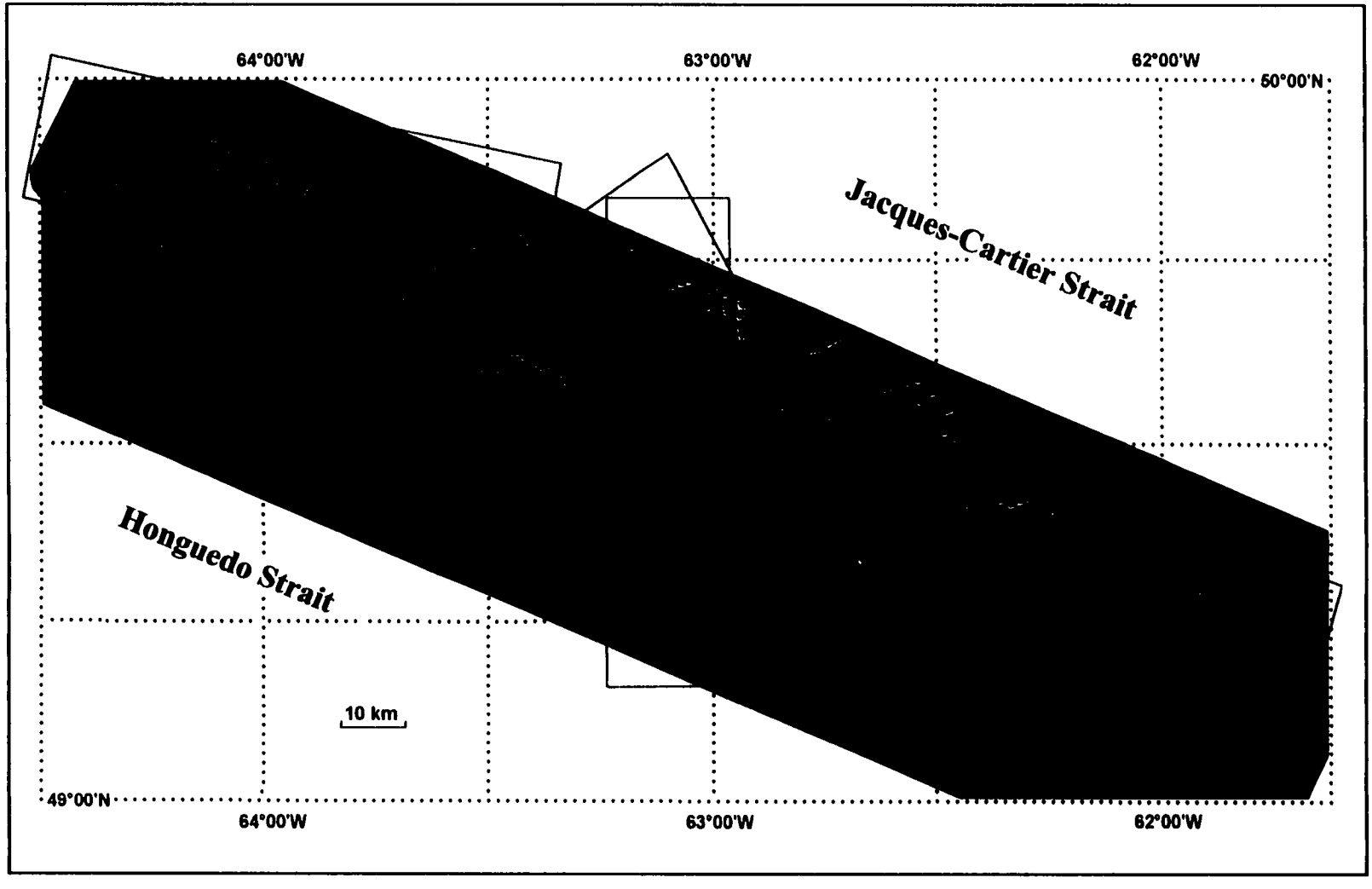
64°00'W
63°00'W
62°00'W
50°00'N
Jacques-Cartier Strait
Honguedo Strait
10 km
49°00'N
64°00'W
63°00'W
62°00'W

3.1.2 Signal Calibration and Data Pre-Processing

Signal calibration and data pre-processing are both essential to extract reliable polarimetric parameters from the fully polarimetric SAR data and were done in this study by CCRS before the delivery of the data. As described by Hawkins *et al.* (1999a and 1999b), the calibration of the radar signal involved calibrating the amplitude and the phase information and the registration of the four polarised channels (HH, HV, VH, and VV) in the range and the azimuth directions. External polarimetric active radar calibrators (PARCs) and passive trihedral corner reflectors (CRs) deployed across the imaging swath during the acquisition were required to achieve proper signal calibration (Figure 3-1d). The CRs provide calibration results for the amplitude and phase components of the co-polarized channels (HH and VV) whereas the PARCs provide equal backscatter in all polarisations, thus allowing as well the calibration of the cross-polarised channels (HV and VH). Only the 1998 fully polarimetric flight lines were completely calibrated using CRs and PARCs (Hawkins and Murnaghan, 1998).

The radiometric calibration error of the 1998 fully polarimetric SAR data was estimated to be less than 1.0 dB for all polarisations within ± 20° of the antenna boresight angle at 28° (Figure 3-2b) and the phase calibration accuracy for all polarisations was estimated to be less than 10° (Hawkins *et al.*, 1999a). These calibration errors are more than acceptable when compared to similar polarimetric data sets also acquired by the Convair-580 SAR system and

calibrated by the CCRS. The other flight lines acquired for this study were not fully calibrated and pre-processed since they were not considered for the polarimetric analysis.

Once calibrated, the fully polarimetric SAR data were pre-processed using the CCRS PolGASP processor (Hawkins *et al.*, 2002). The PolGASP processor allows data stripping, motion processing, gain normalization, channel registration, motion compensation, and azimuth correlation. All those steps are needed in order to eliminate any signal errors (noise) generated internally by the imaging system itself or by external perturbations of the platform. Any uncorrected signal errors may result in false magnitude and phase information. The transformation of the magnitude and phase information into a scattering matrix (also called the Stoke matrix) from which the polarimetric parameters are derived was also performed during the PolGASP pre-processing of the data.

3.1.3 Radiometric and Geometric Corrections

In this study, radiometric correction involves the enhancement of the intensity image generated from the magnitude information of the 1991 wide-swath SAR image whereas geometric correction consists of projecting the same SAR image onto a regular, two-dimensional cartesian grid. Both corrections were required to facilitate the image interpretation and to map in their respective ground location the various geological elements of Anticosti Island. The 1998 fully polarimetric SAR data were not radiometrically and

geometrically corrected since the polarimetric analysis was preferably done on the calibrated and pre-processed data alone.

Several applications within the remote sensing visualisation and analysis package developed by *PCI Geomatics* (PCI 6.2, 1998) were used in order to perform the radiometric and geometric corrections of the 1991 SAR data. The various steps along with the corresponding *PCI* applications used to extract, visualise, enhance and geocode the wide-swath SAR data are summarised in the flow charts of Figure 3-4, and the details on how these two corrections were performed are provided in Appendix A. It should be noted here that the geometric correction involved the projection of the intensity image to a 25 m spatial resolution on a UTM (Universial Transversal Mercator) co-ordinate system by means of GCPs (Ground Control Points) and a polynomial function. The positional error obtained with the geometric correction of the intensity image falls in the order of 29.9 m (or 2.0 pixel) in Easting and 37.8 m (or 2.5 lines) in Northing.

3.2 Ancillary Data Description

The utility of the various ancillary geoscience data sets in this study was to perform the radiometric and geometric corrections of the intensity image, but also to support the image interpretation and the polarimetric analysis of the SAR data. Four geoscience data sets were considered important, including: 1) the three 1:100 000 geology map sheets of Petryk (1981b), 2) the 1:250 000 superficial geology map of Dubois *et al.* (1990), 3) a modified

Figure 3-4: Schematic overview of the steps involved in the radiometric and geometric corrections of the 1991 wide-swath SAR image of Anticosti Island.

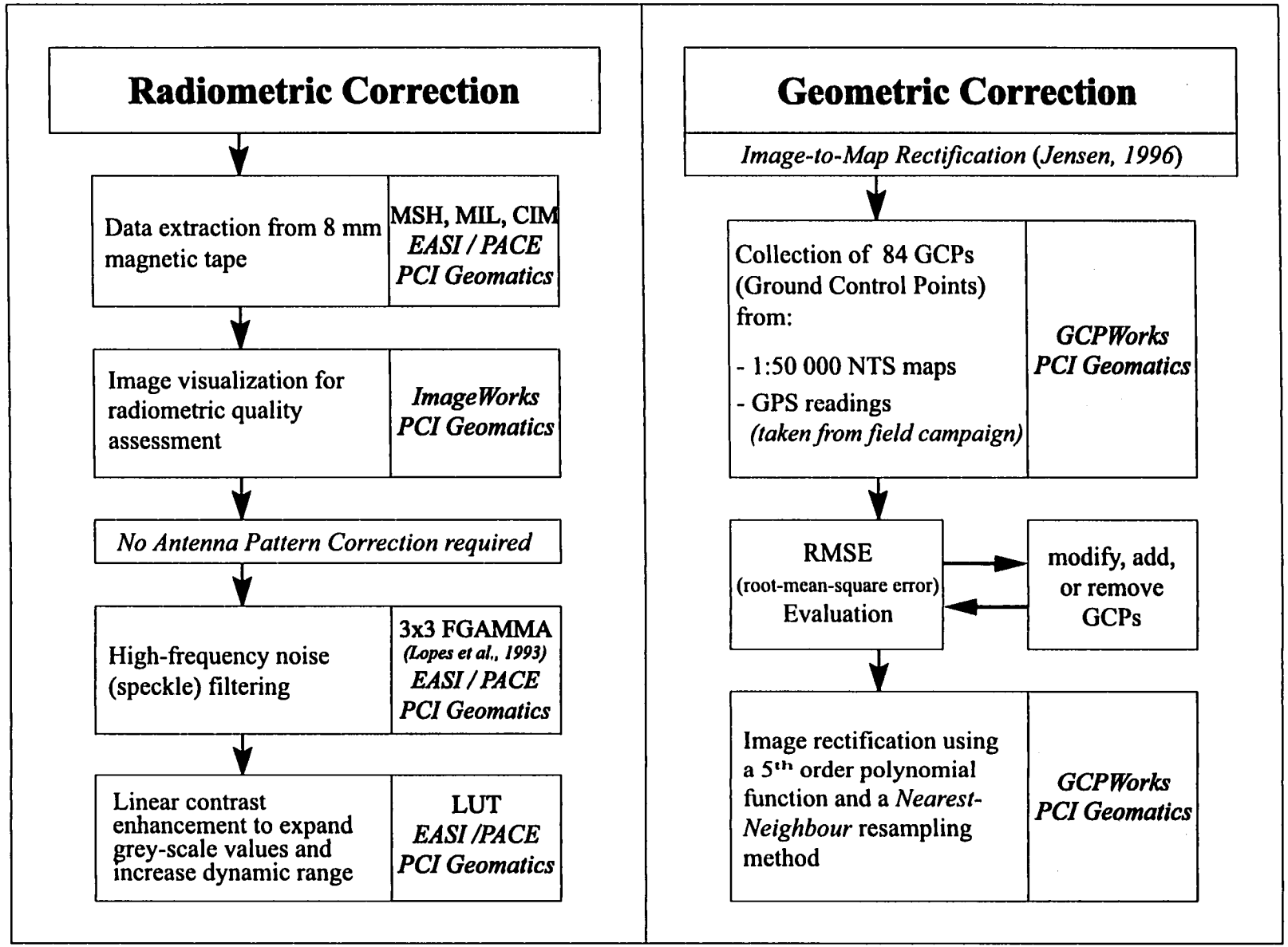
Radiometric Correction
Data extraction from 8 mm magnetic tape
MSH, MIL, CIM
EASI / PACE
PCI Geomatics
Image visualization for radiometric quality assessment
ImageWorks
PCI Geomatics
No Antenna Pattern Correction required
High-frequency noise (speckle) filtering
3x3 FGAMMA
(Lopes et al., 1993)
EASI / PACE
PCI Geomatics
Linear contrast enhancement to expand grey-scale values and increase dynamic range
LUT
EASI /PACE
PCI Geomatics
Geometric Correction
Image-to-Map Rectification (Jensen, 1996)
Collection of 84 GCPs (Ground Control Points) from:
- 1:50 000 NTS maps
- GPS readings
(taken from field campaign)
GCPWorks
PCI Geomatics
RMSE
(root-mean-square error)
Evaluation
modify, add, or remove GCPs
Image rectification using a 5th order polynomial function and a Nearest-Neighbour resampling method
GCPWorks
PCI Geomatics

version of the third decennial vegetation inventory conducted by the *Ministère des Ressources Naturelles du Québec*, and 4) topographic data sets available from 1:50 000 NTS and NTDB maps covering the entire island.

The digitised version of the 1:100 000 geology map of Petryk (1981b), along with the latest stratigraphic framework of Long and Copper (1994), was used to assist the image interpretation and to perform a geological comparison with the results obtained in this study.

The surface geology map of Dubois *et al.* (1990) and the third decennial vegetation inventory conducted by the *Ministère des Ressources Naturelles du Québec* were both indispensable in the extraction of polarimetric parameters part of the quantitative analysis of the fully polarimetric SAR data. The partial coverage of the vegetation inventory database provided by *Produit Forestier Anticosti* (*PFA*), a logging company exploiting the forest of the island, is presented in Figure 3-5 along with a description of the various field attributes available in that GIS structured database.

The 1:50 000 National Topographic System (NTS) and National Topographic Database (NTDB) maps covering the entire island were used to geocode the wide-swath SAR image and to extract a Digital Elevation Model (DEM) representing the island elevation. Since both sources of topographic data have a horizontal accuracy of ± 50 m, it could be assumed that the resulting DEM and its derivative products fall in the same order of accuracy. Appendix B gives the details on how the DEM was generated whereas Figure 3-6 is a small-scale

Figure 3-5: Partial coverage of the GIS structured third decennial vegetation inventory conducted by the *Ministère des Ressources Naturelles du Québec* along with a description of the its field attributes.

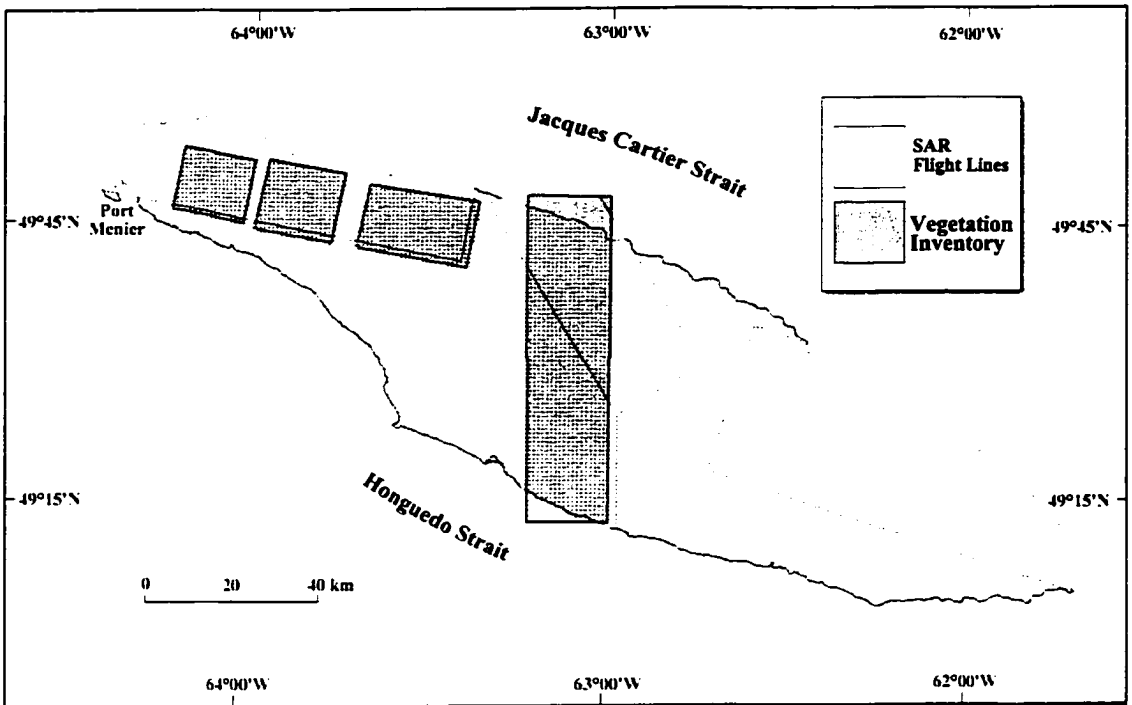

Field Attribute	Description	Content
Canopy	Type of forest stand	- Softwood - Hardwood - Mixed
Identity	Statement of identity	- Forest cover (> 50 % dominating species) - balsam fir, white spruce, black spruce, others - Terrain - water, wetland, baresoil, others - Perturbation - burn site, insect outbreak, clear cut, others
Year of perturbation	When available, it is the year the perturbation started, otherwise it is extrapolated from the age of the forest stand (*below*)	
Age	Age of the forest stand	- Old uneven-aged -Young uneven-aged - Even-aged
Tree Height	Height of the dominating forest stand in metres	
Density	Ground projection of the tree crown in percentage	

Figure 3-6: Grey-scale Digital Elevation Model (DEM) derived from the 1: 50 000 digital maps of the National Topographic Database (NTDB) of Anticosti Island. The dark grey tones are low altitude values whereas the bright tones are representing the higher altitudes.

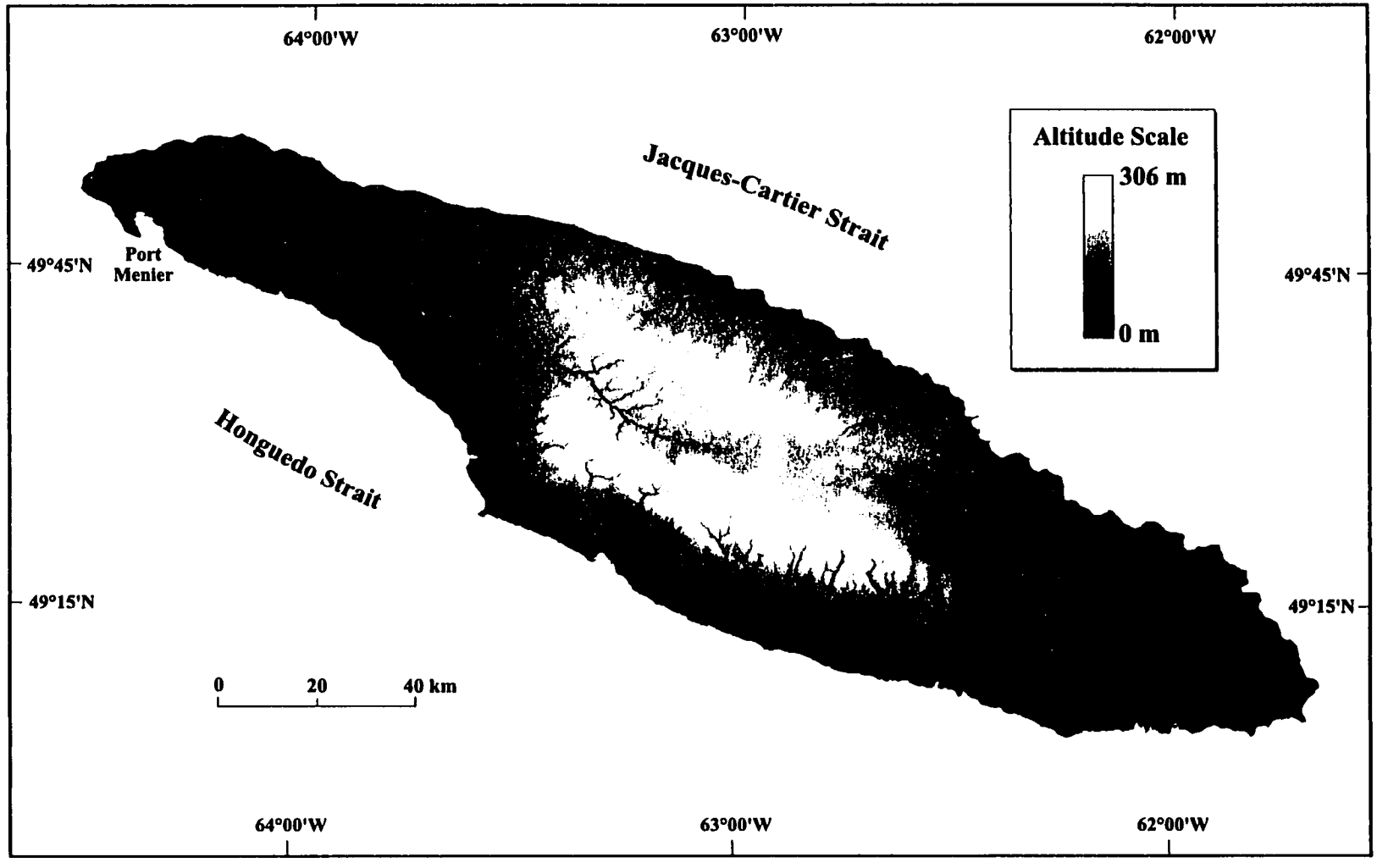
64°00'W
63°00'W
62°00'W
Altitude Scale
306 m
0 m
Jacques-Cartier Strait
49°45'N
Port
Menier
49°45'N
Honguedo Strait
49°15'N
49°15'N
0
20
40 km
64°00'W
63°00'W
62°00'W

representation of the DEM where each grey-scale image pixel represents an elevation value in meters. The DEM was of great value in this study since topographic related products were derived from it to assist the image interpretation. It was also used to enhance even more the radiometry of the SAR image prior to its interpretation. The following section describes the derivative products and their integration with the wide-swath SAR image for improving its radiometry.

3.2.1 Derivative Products and Data Integration

Three derivative products were extracted from the 1:50 000 DEM. The first product is a shaded relief image accentuating with highlight and shadow effects the topographic relief of Anticosti Island (Figure 3-7). It was generated using the PCI applications (PCI 6.2, 1998). Each image pixel of the shaded relief represents the amount of «light» reflected from a surface and a point light source positioned at an azimuth angle of 200° and an elevation angle of 15° from the horizontal. Such configuration was selected to coincide as much as possible with the look-direction of the wide-swath SAR data and create a constructional topographic effect when integrating both data sets. The fusion of the two data sets was done using an arithmetic function where 25 % of the shaded relief values were multiplied to the intensity values of the SAR data. The result is a shaded relief SAR image with a significant radiometric improvement, as demonstrated in Figure 3-8, for which the radar responses of the terrain elements were preserved. A 1:250 000 scale map of the SAR image enhanced with the shaded relief was inserted in the map pocket (*Map-Image 1*) at the end of this manuscript.

Figure 3-7: Shaded relief derived from the 1: 50 000 DEM to enhance the radiometry of the 1991 wide-swath SAR image when integrated with it. The indented sub-scenes (A & B) are close-ups showing the highlighted topographic relief of Anticosti Island with a simulated light source positioned at an azimuth angle of 200° and an elevation angle of 15° above the horizon.

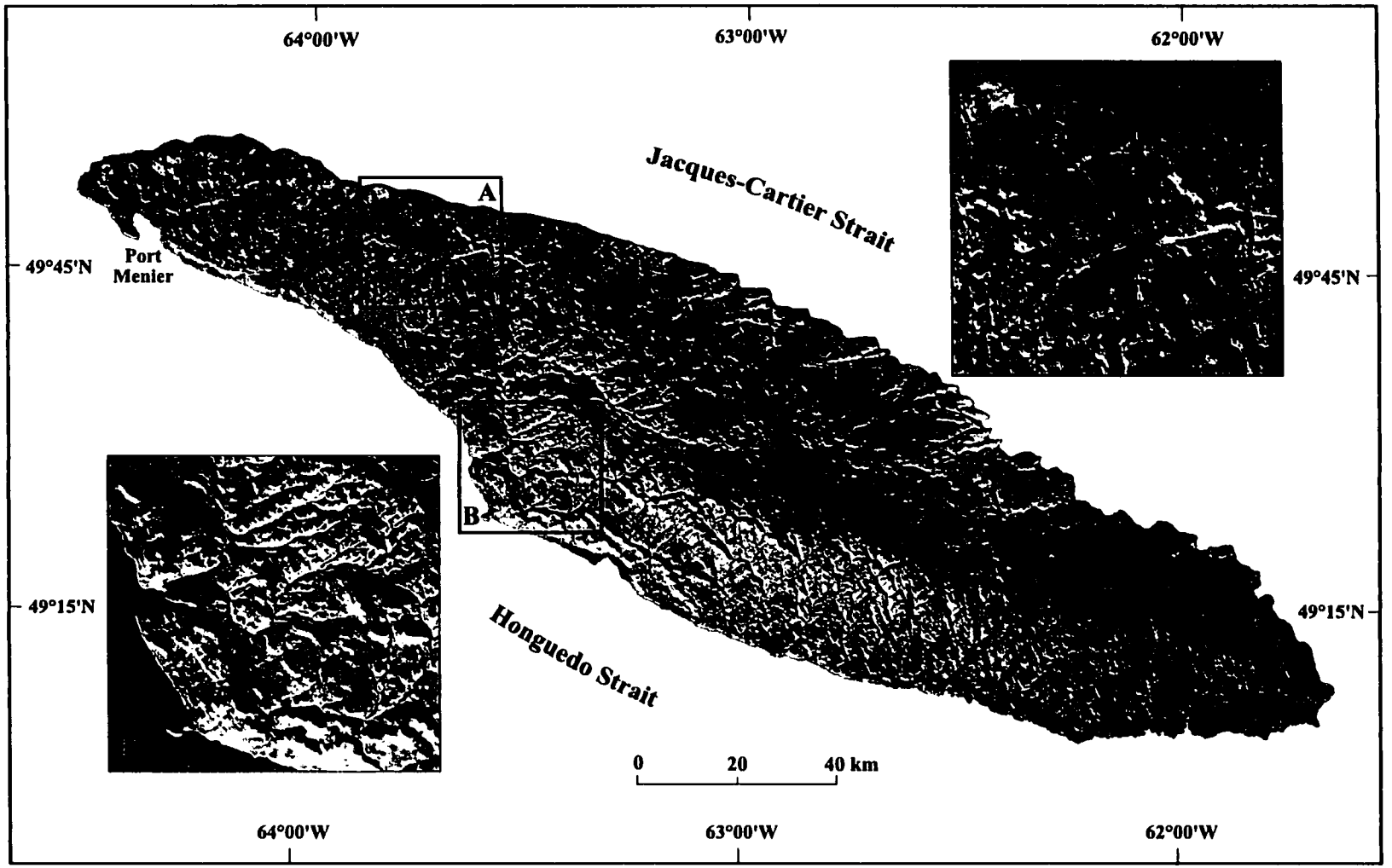
64°00'W
63°00'W
62°00'W
49°45'N
49°15'N
Port
Menier
Jacques-Cartier Strait
Honguedo Strait
A
B
0
20
40 km

Figure 3-8: Comparison of two sub-scenes taken before (A & B) and after (A' & B') the radiometric enhancement by the integration of the shaded relief with the wide-swath SAR image:

(A) sub-scene taken over the Chicotte Formation for which the arrow points out a coral reef horizon significantly enhanced in A';
(B) sub-scene taken in the northwestern part of the island showing the well-developed cuesta morphology and a morainic ridge (*arrow*) nicely highlighted in B';

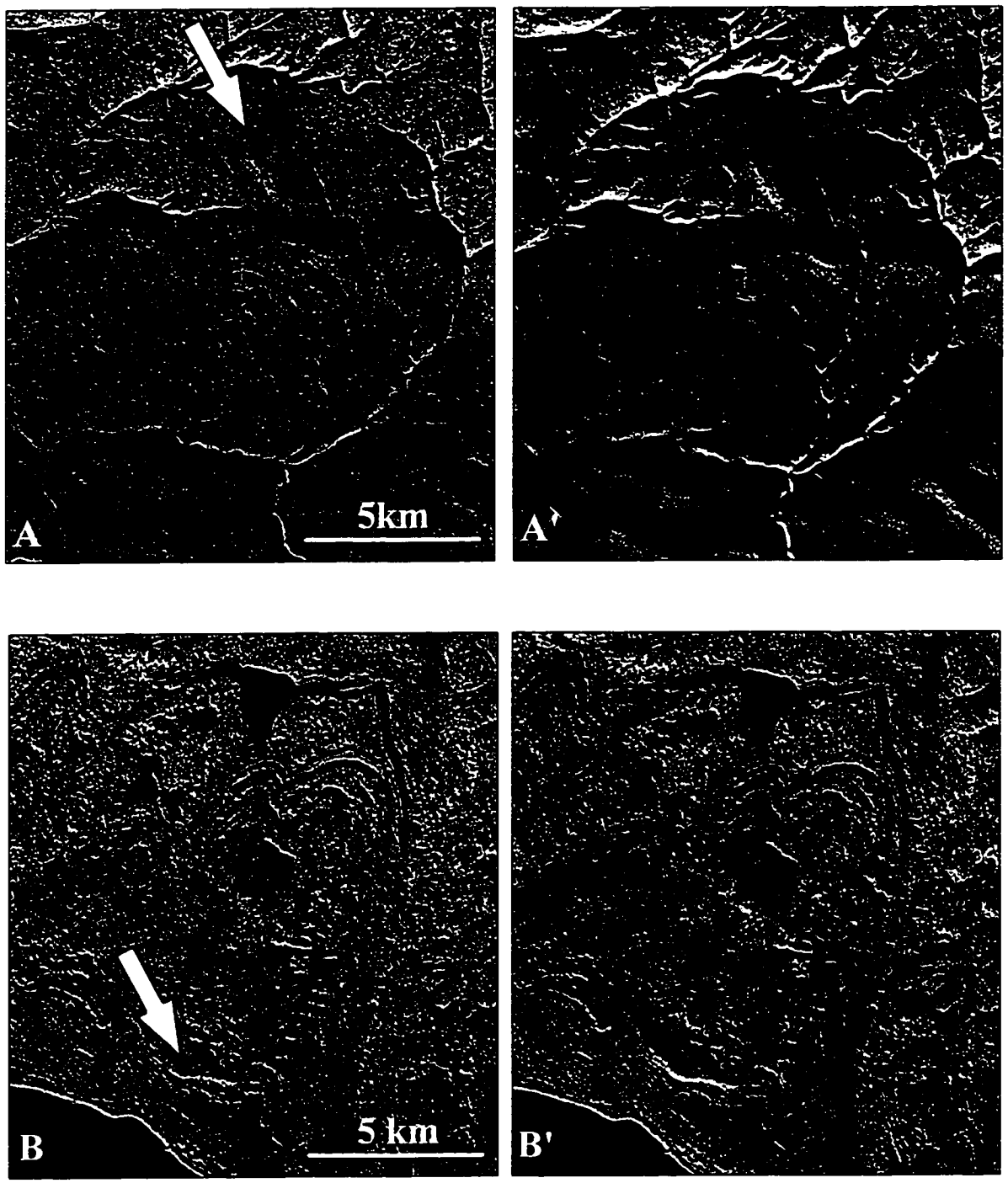
A
5km
A'
B
5 km
B'

It is on a similar image product that the image interpretation of the island geology was conducted.

The second set of products derived from the DEM is grey-scale images containing the slope and the aspect (orientation) angles characterizing the island's topographic relief. These products were also generated using PCI applications (PCI 6.2, 1998). The slope and aspect derivative products were not integrated to the SAR data, but were used separately as a source of complementary information to locate and trace more precisely the lithological contacts between the island formations. They allowed adjusting the interpreted contacts where the point of rupture between the dipslope and the antidip scarps of the bedding plane is likely associated to the lithological changes between formations.

The last derivative product is a 3D chromo-stereoscopic image produced with PCI applications (PCI 6.2, 1998) by integrating the DEM with the shaded relief SAR image as described in Toutin and Rivard (1995) and Toutin (1997). A 3D chromo-stereoscopic image is simply a tool in this study to qualitatively perceive depth of the SAR data based on the principle of colour vision in order to better appreciate the existing relationship between the litho-stratigraphic units and the topographic relief of the island as well as locating and tracing more precisely the formation contacts. Figure 3-9 is a small-scale representation of the chromo-stereoscopic SAR image.

Figure 3-9: Small-scale representation of the 3D chromo-stereoscopic image derived by integrating the 1:50 000 DEM with the wide-swath SAR image.

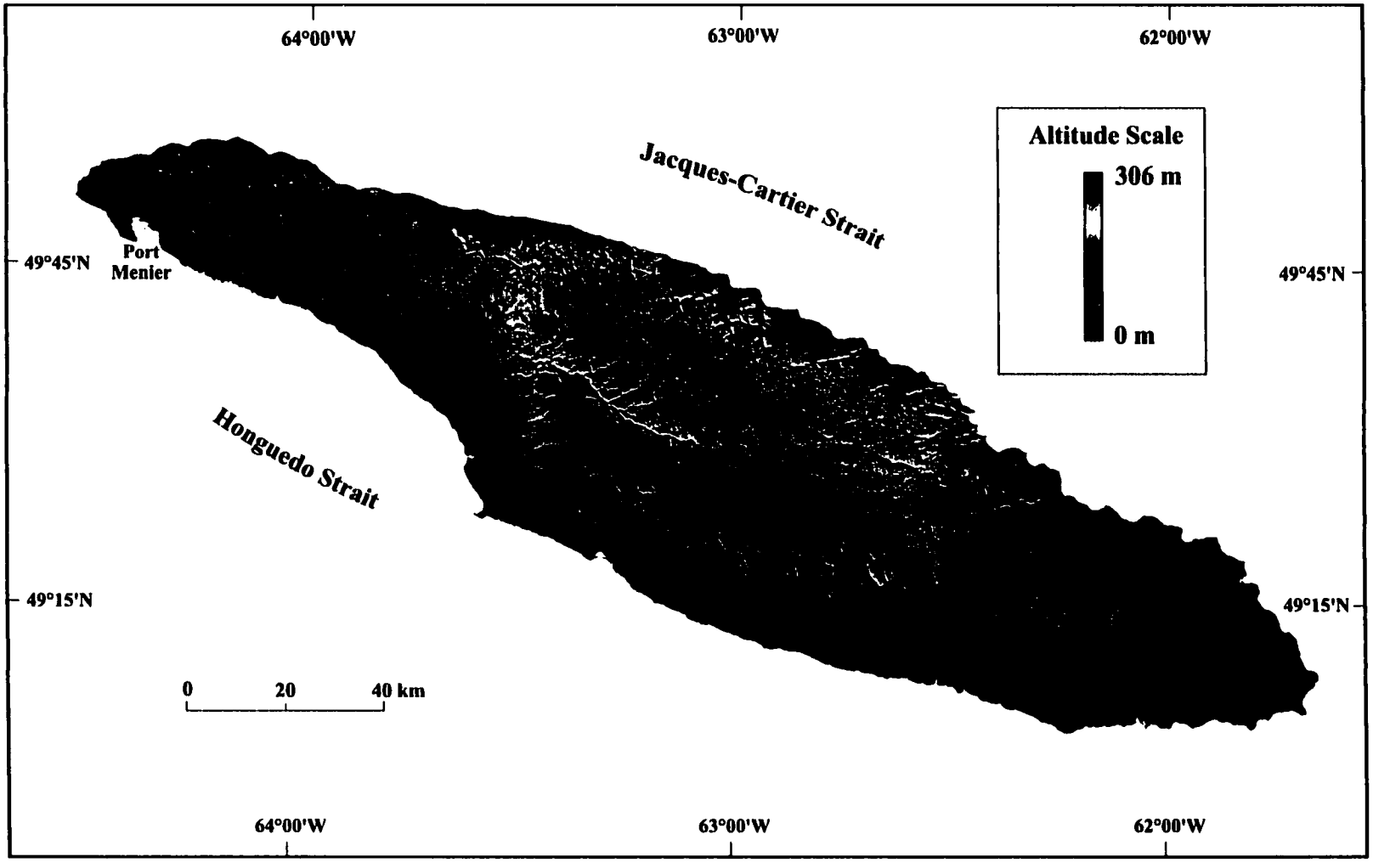
64°00'W
63°00'W
62°00'W
Altitude Scale
306 m
0 m
Jacques-Cartier Strait
49°45'N
Port
Menier
49°45'N
Honguedo Strait
49°15'N
49°15'N
0
20
40 km
64°00'W
63°00'W
62°00'W

3.3 Image Interpretation

The image interpretation methodology consisted of identifying radar clues such as tones, textures, shapes, sizes, shadows, highlights, and patterns present in the shaded relief SAR image in order to locate and trace the formation contacts and map the structural geology of the island. A good understanding of the radar fundamentals, thus the significance of the acquired radar responses with respect to the terrain characteristics, particularly with the island cuesta morphology associated to the bedrock geology, was essential.

The image interpretation, based on the stratigraphic framework proposed by Petryk (1981b) and later revised by Long and Copper (1994), was first conducted on a paper copy of the shaded relief SAR image. Topographic markers associated to all formation boundaries were first located in the field during the three weeks of ground truth investigations conducted in 1999 and then identified on the SAR image. Tracing their precise location from one end of the island to the other was sometimes difficult, especially in areas of subtle topography, and required the extrapolation of the contacts based on expert knowledge and field observations.

Once the preliminary interpretation was completed, it was digitised in order to integrate it with the various ancillary geoscience data sets. The derivative products extracted from the DEM, aided by discussions with Long and Copper (1999 and 2001) allowed adjusting digitally the interpretation with a higher degree of precision. It was then used to produce a new geology map as presented in section 4.

3.4 Fully Polarimetric SAR Data Analysis

The quantitative analysis of the fully polarimetric SAR data was done on the 1998 *L4P3* flight line over a restricted study area located in the northwestern end of Anticosti Island as illustrated in Figure 3-10. It covers the Vauréal and the Ellis Bay formations where ground controls exist and where vegetation and surface geology data are available (Figure 3-11).

The polarimetric analysis was conducted using the *Polarimetric Workstation* (*PW*) software developed by Touzi and Charbonneau (2002), which runs under the *MATLAB*® application. The *PW* software allows the extraction of the co- and cross-polarisation responses, the pedestal height, the backscatter coefficient ($\sigma°$), as well as many others advanced polarimetric parameters such as the Cloude's entropy/anisotropy/alpha (H/A/α) parameters, the phase correlation, and the extrema of the completely-polarised and completely-unpolarised wave components. Since a lot of research is still required to fully understand the true meaning of all these polarimetric parameters, only the co- and cross-polarisation responses, the pedestal height, and the backscatter coefficient ($\sigma°$), thus the basic parameters, were considered in this study.

Understanding the meaning of these basic parameters before extracting them for analysis is essential. Therefore, the utility of the co- and cross-polarisation responses is to characterize, in terms of orientation (ψ) and ellipticity (χ) angles, the polarised signal at linear, circular, and elliptically configurations. In other words, the co- and cross-polarisation responses are

Figure 3-10: Location of the restricted study area (*red box*) where the extraction of the polarimetric parameters was conducted. The *L4P3* colour composite mosaicked to the wide-swath SAR image was created from the HH, HV, and VV polarisation channels.

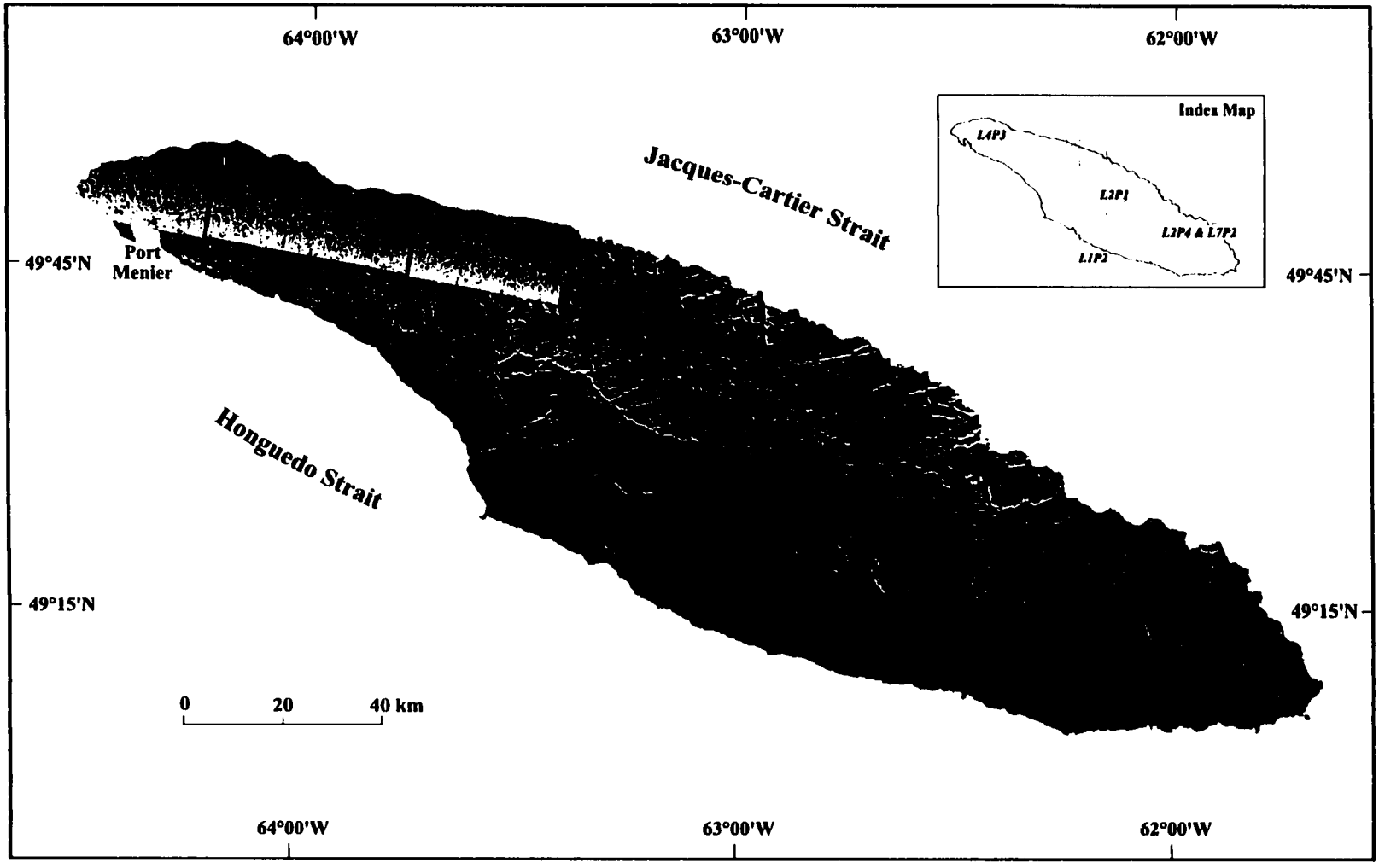
64°00'W
63°00'W
62°00'W
Index Map
L4P3
L3P1
L2P4 & L7P2
L1P2
Jacques-Cartier Strait
49°45'N
Port
Menier
Honguedo Strait
49°15'N
0
20
40 km

Figure 3-11: Partial coverage of the GIS-structured vegetation inventory used for the polarimetric analysis of the *L4P3* SAR flight line over the restricted study area.

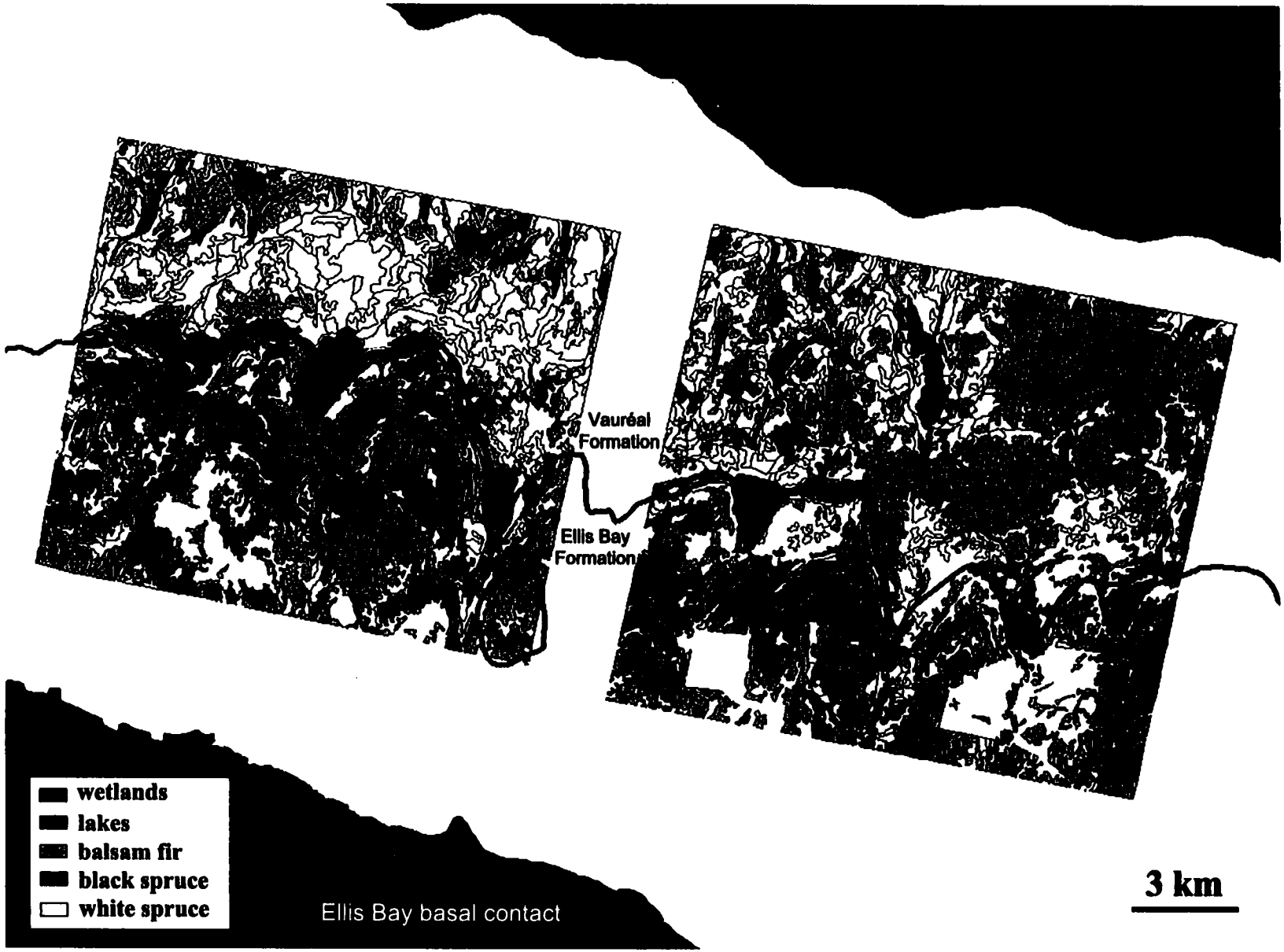
Vauréal Formation
Ellis Bay Formation
wetlands
lakes
balsam fir
black spruce
white spruce
Ellis Bay basal contact
3 km

indicators of the scattering mechanisms dominating the ground targets. The pedestal height is a normalized measure of the importance of the radar unpolarised scattering component, whereas the backscatter coefficient (σ°) is a normalized measure of the radar return from a distributed target, which is defined as per unit area on the ground (Boerner *et al.*, 1998). With these three polarimetric parameters in hand, enough information exits in order to define the ground targets and perhaps distinguish in this study any preferential distribution of the vegetation cover with respect to the underlying surface and bedrock geology.

The systematic extraction of the polarimetric parameters was conducted on 5 to 10 samples of radar responses within the balsam fir, white spruce, and black spruce forest stands overlying locally glacial till or thin organic soil on the Vauréal or the Ellis Bay strata. Cross-referencing the vegetation inventory with the surface geology map and the newly interpreted geology of the island allowed collecting these scattering samples. A schematic overview of the methodology used to select the various bedrock, soil, and vegetation scattering samples in order to extract the polarimetric parameters of the fully polarimetric SAR data is presented in Figure 3-12.

Figure 3-12: Schematic overview of the systematic extraction of the polarimetric samples taken from the 12 vegetation, soil, and bedrock scattering categories.

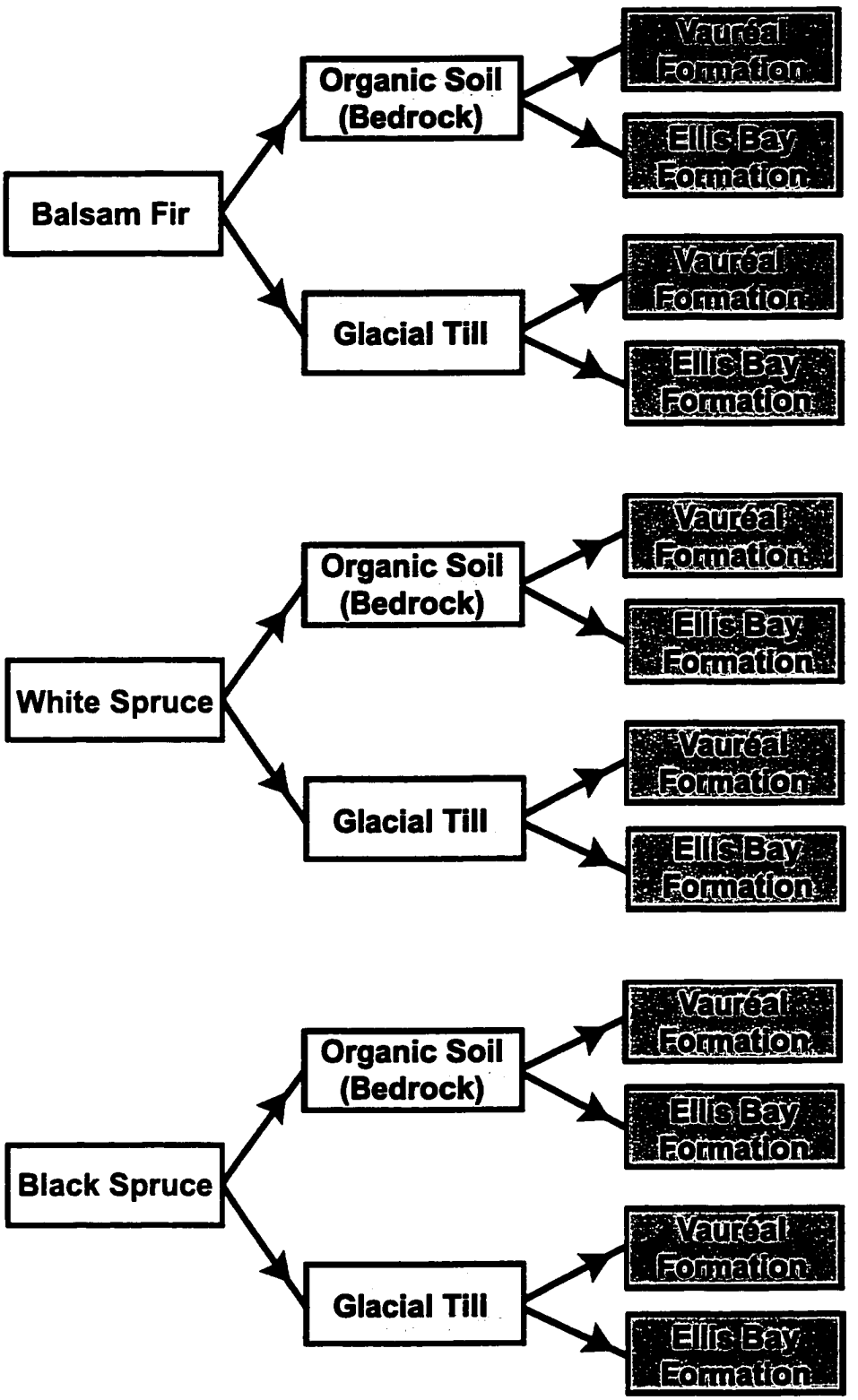
Balsam Fir
Organic Soil (Bedrock)
Vauréal Formation
Ellis Bay Formation
Glacial Till
Vauréal Formation
Ellis Bay Formation
White Spruce
Organic Soil (Bedrock)
Vauréal Formation
Ellis Bay Formation
Glacial Till
Vauréal Formation
Ellis Bay Formation
Black Spruce
Organic Soil (Bedrock)
Vauréal Formation
Ellis Bay Formation
Glacial Till
Vauréal Formation
Ellis Bay Formation

4. Presentation of Results

This section presents the results of the two approaches used to improve the geological mapping of Anticosti Island. The geology map derived from the shaded relief SAR image interpretation supported by derivative products will be first presented. The contribution of the SAR image enhanced by the shaded relief to gain more precision in the geological mapping of the island will be illustrated by means of comparisons between the newly interpreted formation contacts and those digitised from the geology map of Petryk (1981b). The presentation of the structural geology derived from the lineament interpretation of the SAR image will follow. Finally, the resulting polarimetric parameters extracted from the fully polarimetric SAR data will be analysed in order to understand their potential in mapping the island geology.

4.1 Improved Geology Map

Appended to this manuscript (see map pocket) is a map-image printed at a scale of 1:250 000 illustrating the improved geology of Anticosti Island while respecting the latest stratigraphic framework proposed by Long and Copper (1994). The new formation boundaries and the most important structural lineaments were overlaid in ArcMap®, along with the hydrology, the road network, the contour lines, and other thematic elements derived from the NTDB, on top of the SAR image enhanced by the shaded relief. A simplified version of that new geology map is presented in Figure 4-1.

Figure 4-1: Small-scale geology map of Anticosti Island derived from the image interpretation of the wide-swath SAR image enhanced with the shaded relief.

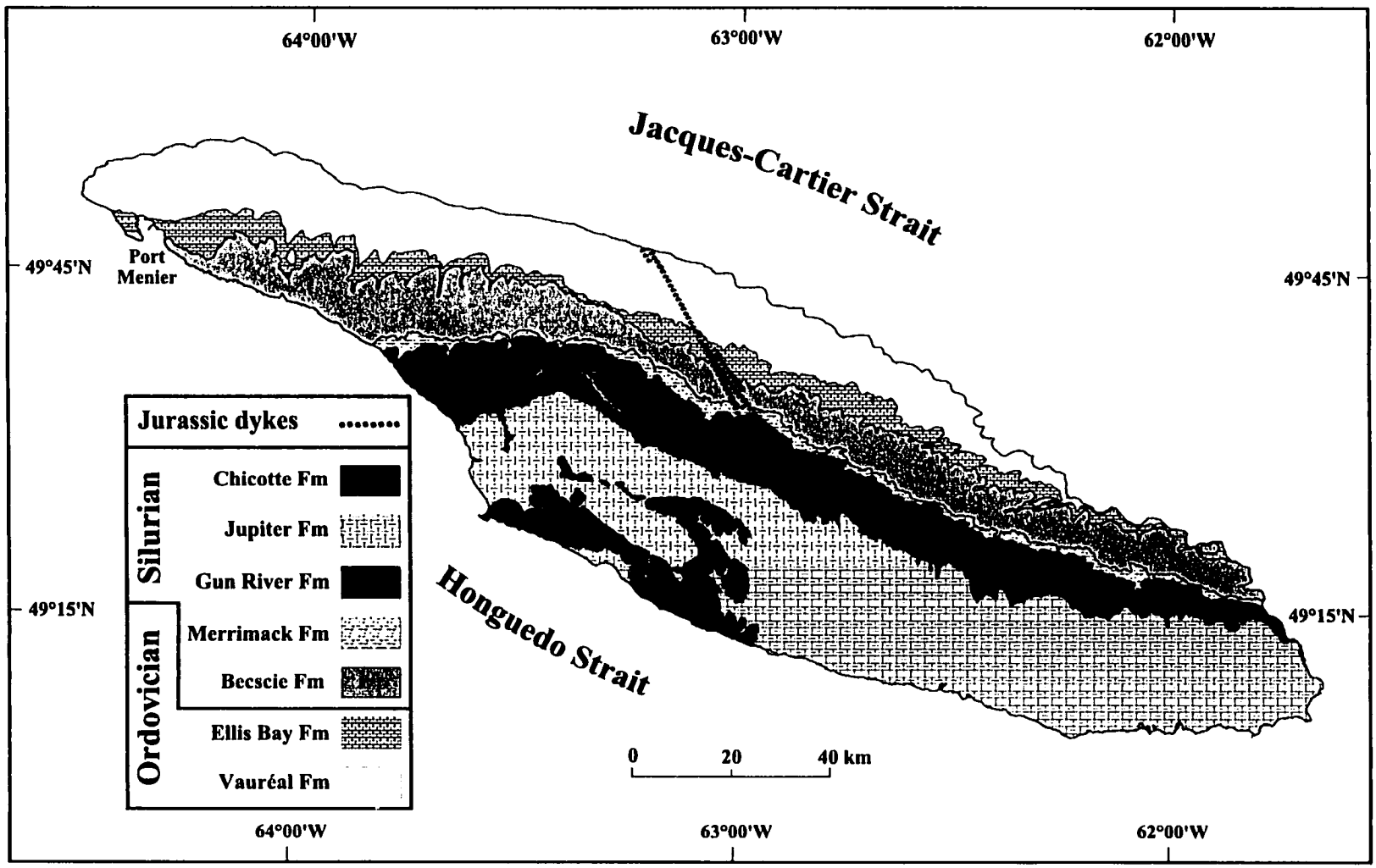
64°00'W
63°00'W
62°00'W
Jacques-Cartier Strait
49°45'N
Port
Menier
49°15'N
Honguedo Strait
Jurassic dykes
Silurian
Chicotte Fm
Jupiter Fm
Gun River Fm
Ordovician
Merrimack Fm
Becscie Fm
Ellis Bay Fm
Vauréal Fm
0
20
40 km

The new geology map reflects more precisely the actual stratigraphy of the island in many ways. The addition of the Merrimack Formation is one of them, but several other examples demonstrating the mapping improvement will be hereafter presented by comparing the newly interpreted geology to the one previously proposed by Petryk (1981b).

4.1.1 Contact Uncertainty

Before comparing the two sets of formation contacts, it is important to understand the level of confidence to which they were distinctively mapped. As listed in Table 4-1 and calculated using *ArcGIS*® tools, less than 5% of Petryk's contacts were mapped as certain while the remaining contacts were either mapped as expected (54 %) or as presumed (41 %). It also shows the percentage of certain, expected, and presumed contacts for each of his formations. The percentage of contacts mapped as certain is surprisingly low even in areas where geological controls were available from accessible outcrops. Figure 4-2, which is a subset of the scanned and digitized versions of Petryk's geology map, illustrates how accessible outcrops did not necessarily increase the contact certainty. The uninterrupted and gradational aspect of the island stratigraphy is partly responsible for that uncertainty, but the lack of lateral ground control along the formation boundaries had also something to do with it.

The new interpreted contacts were mapped more precisely than what Petryk was able to propose because of the additional mapping control provided by the SAR image and the

Table 4-1: Percentage of Petryk's basal contacts mapped as certain, probable, and suggested (Petryk, 1981b). Percentages are not available (*NA*) for the Vauréal and Merrimack basal contacts since they are either not exposed or were unrecognised.

Basal Contacts of Petryk's Formations	Certain	Probable	Suggested	Total Length
Vauréal *(not exposed)*	*NA*	*NA*	*NA*	*NA*
Ellis Bay	**0.0 %**	**59.0 %**	**41.0 %**	**322.9 km**
Becscie	**0.0 %**	**73.6 %**	**27.4 %**	**383.1 km**
Merrimack *(not recognised)*	*NA*	*NA*	*NA*	*NA*
Gun River	**6.4 %**	**48.4 %**	**45.2 %**	**243.1 km**
Jupiter	**0.0 %**	**29.3 %**	**71.7 %**	**260.0 km**
Chicotte	**29.1 %**	**50.1 %**	**20.8 %**	**142.5 km**
All Formations	**4.2 %**	**54.3 %**	**41.5 %**	**1351.5 km**

Figure 4-2: Subset of Petryk's geology map scanned (A) and digitised (B) showing his contact uncertainty due to few lateral ground controls. Yellow dots represent the visited outcrops located mostly along the road network near Lac-aux-Cailloux in the northwestern Anticosti Island.


A
Petit lac Sainte-Marie
Index Map
Anticosti Island
N

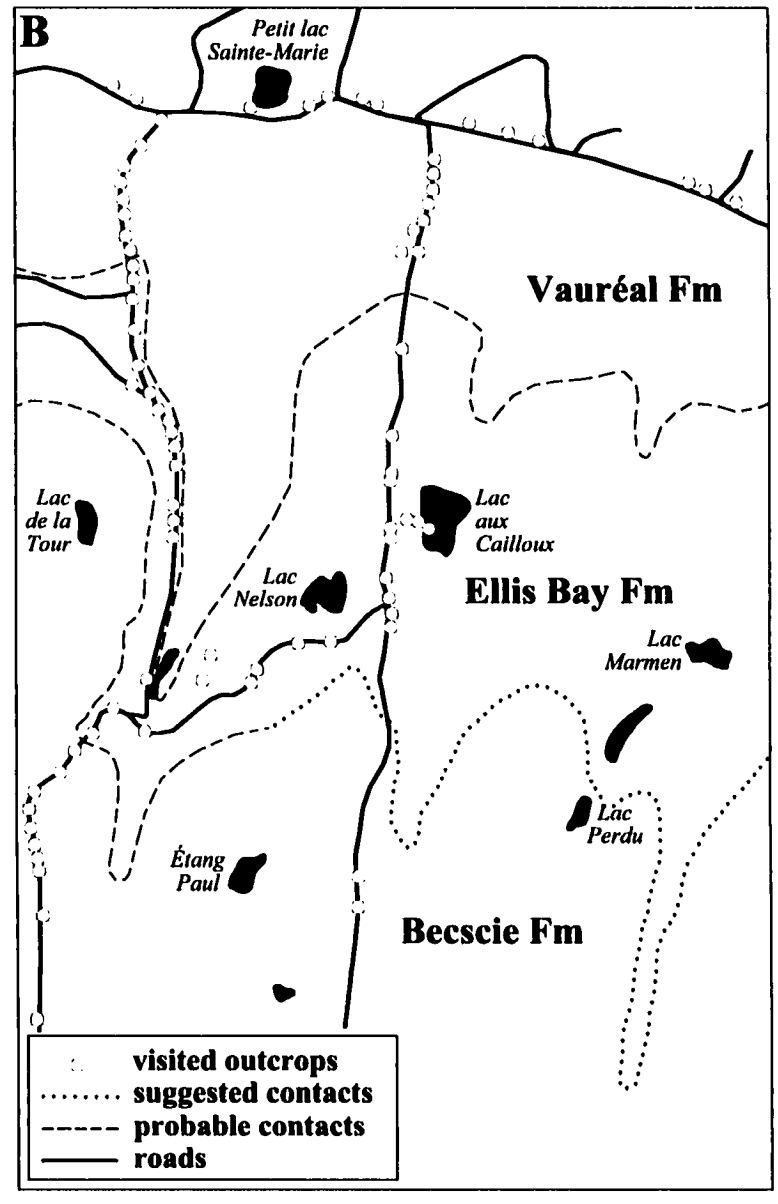
B
Petit lac Sainte-Marie
Vauréal Fm
Lac de la Tour
Lac aux Cailloux
Lac Nelson
Ellis Bay Fm
Lac Marmen
Lac Perdu
Étang Paul
Becscie Fm
visited outcrops
suggested contacts
probable contacts
roads

derivative products (Figure 4-3). The SAR image was very useful in extrapolating laterally the formation contacts in areas of few ground controls. Field observations along with personal communications with Long and Copper (1999 and 2001) allowed validating the higher level of precision to which the new contacts were mapped. Even though it was impossible to quantify the precision gained, the percentage of certain contacts was estimated to exceed the 5 % offered by Petryk. It is only in inaccessible areas with no topographic markers and no radar clues that the newly interpreted contacts were mapped as uncertain.

To illustrate the increase of confidence gained from the new interpretation, the two versions of the Ellis Bay and Becscie basal contacts were plotted on a SAR sub scene (Figure 4-3) centred on Lake Faure located in the northwestern end of Anticosti Island. The newly interpreted contact of the Ellis Bay Formation is following thoroughly the same topographic feature enhanced by the highlights and shadows of the SAR data. The same approach was used to trace the Becscie contact and all the other formation contacts of the island succession. However, Petryk's contacts display no obvious correlation between his interpretation and the topographic expression of the island strata.

4.1.2 Accuracy Assessment

It is essential to demonstrate how well the digitised contacts of Petryk overlay the rectified SAR image in order to appreciate the comparison between both interpretations. Knowing the different sources of positional errors (Table 4-2) and their spatial distribution, thus the

Figure 4-3: Comparison of the cartographic location of the new Ellis Bay and Becscie basal contacts with respect to Petryk's interpretation. Note how the new contacts follow more closely the topographic expression of the stratigraphic units in comparison with Petryk's contacts.

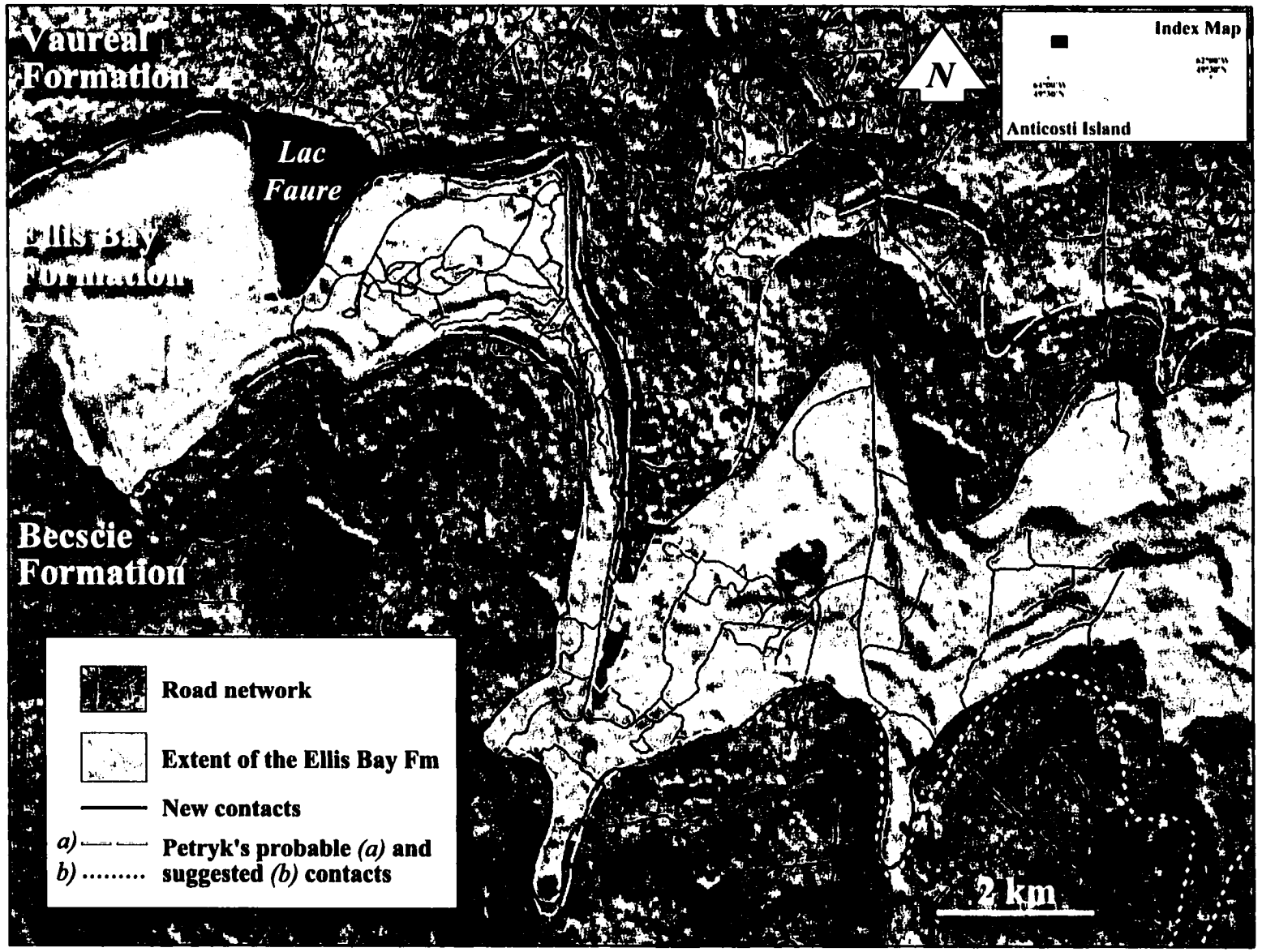
Vaureal Formation
Lac Faure
Ellis Bay Formation
Becscie Formation
N
Index Map
Anticosti Island
Road network
Extent of the Ellis Bay Fm
New contacts
a) Petryk's probable (a) and
b) suggested (b) contacts
2 km

Table 4-2: List of the different sources of cartographic errors and their inherited and calculated positional accuracy essential to know in order to compare interpretations.

Sources of Errors	Scale	Horizontal Accuracy
Geometric correction of SAR data	*NA*	**± 29.9 m in Easting** (~2.0 pixel) **± 37.8 m in Northing** (~2.5 lines)
NTS paper maps (with insignificant paper distortion)	**1:50 000**	**± 50 m**
NTDB digital maps (and extracted DEM)	**1:50 000**	**± 50 m**
Paper distortion (geology map of Petryk, 1981b)	**1:100 000**	**± 100 m** (1 mm)
Scale precision (geology map of Petryk, 1981b)	**1:100 000**	**± 50 m** (1/2 mm)
Geology map registration on digitising tablet	*NA*	**± 50 m** (1/2 mm)
Digitising tablet accuracy	*NA*	**± 1/2 mm** (or ± 50 m on a 1:100 000 map scale)
Overall accuracy of the digitised geology map of Petryk (1981b)	*NA*	**130 m** (or 5 pixel on SAR image)

accuracy of both sets of contacts, will allow understanding the precision gained from mapping the island geology using SAR data.

The accuracy of the newly interpreted geology depends on the positional error of the SAR image, but also on the meticulousness and the level of confidence to which the visual interpretation was conducted. The positional error of the SAR image is in the range of 29.9 m (or 2.0 pixel) in Easting and of 37.8 m (or 2.5 lines) in Northing as calculated during the geometric correction of the data (Appendix A). It is, however, safer to define the positional error of the newly interpreted contacts to the least accurate source of data used to rectify the SAR image. Therefore, the ± 50 m accuracy of the NTS map sheets, which is equivalent to the accuracy of the NTDB used to generate the DEM and the derivative products, better represents the positional error of the interpreted contacts.

The digitised contacts, for their part, are not perfect and do not always reflect exactly what appears on Petryk's maps. The physiological differences between the paper and digital versions are partly caused by involuntary and inevitable agitation of the operator's hand during the digitising process, but also from various sources of random and systematic errors. Random errors are the most difficult and sometimes impossible to calculate. Paper distortion is one of them and was partly responsible for the planimetric irregularities observed on Petryk's maps. It was arbitrarily estimated, based on the condition of Petryk's map sheets, to be no more than 1 mm or ± 100 m on a 1:100 000 map scale. The precision to which these map sheets can be read is another source of random error to consider and is usually half the

smallest map unit or in this particular case ± 50 m. The map registration on the digitising tablet has also resulted in a random error falling in the range of ± 50 m. The only systematic error to be considered here is the one coming from the precision of the digitising tablet. As provided by the manufacturer, the accuracy of the *Altek-AC30* digitising tablet is ± 0.5 mm, which translates to ± 50 m on Petryk's map sheets. The overall accuracy of the digitised contacts is the result of these independent random and systematic errors combined together. It was calculated by summing the squares of each of these error components and then by taking the square root of that sum. The overall accuracy was therefore calculated to be ± 130 m, which is the equivalent of ± 5 pixel on the rectified SAR image. The ± 50 m positional error of the SAR image on which Petryk's contacts were overlaid for comparison purposes was not used in the above calculation since it affects equally both sets of contacts and therefore cancels out.

4.1.3 Geological Comparison

Buffer zones and analytical tools in ArcGIS® allowed calculating how much of the new contacts fall inside the error interval of the digitised contacts. Both sets of contacts are comparable 23 % of the time, but with the new interpretation respecting more precisely the topographic expression of the island strata. The remaining 77 % of the interpreted contacts are either the result of a completely different interpretation or simply a better fit to the topography falling outside the calculated error interval as illustrated in Figure 4-4. Table 4-3

Figure 4-4: Representation of the overlapping basal contacts of the Ellis Bay and Becscie formations falling inside the buffer zone corresponding to the of positional error of Petryk's interpretation.

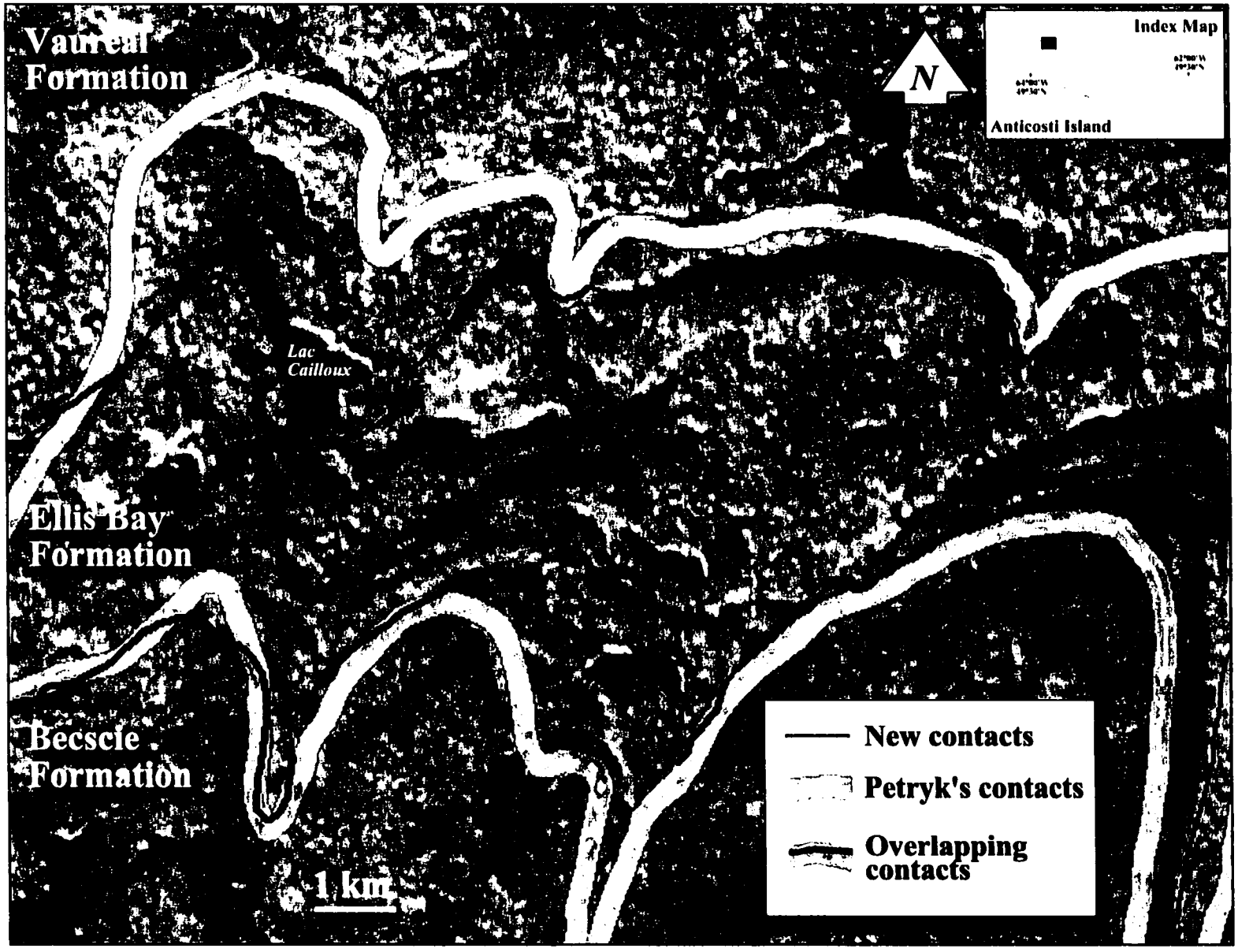
Vauréal Formation
Lac Cailloux
Ellis Bay Formation
Becscie Formation
1 km
N
Index Map
Anticosti Island
New contacts
Petryk's contacts
Overlapping contacts

Table 4-3: Percentage of overlapping contacts between the new and former interpretations. No percentage is available (*NA*) for the Vauréal and Merrimack formation contacts because they are either not exposed or previously unrecognised.

Basal Contact Comparison	**Total Length** *(new contacts)*	**Overlapping Contacts** *(132.3m buffer zone)*	**%**
Vauréal *(not exposed)*	*NA*	*NA*	*NA*
Ellis Bay	**255.8 km**	**61.9 km**	**24.2 %**
Becscie	**344.5 km**	**128.7 km**	**37.4 %**
Merrimack *(not originally recognised)*	*NA*	*NA*	*NA*
Gun River	**292.1 km**	**54.3 km**	**18.6 %**
Jupiter	**228.2 km**	**22.0 km**	**9.6 %**
Chicotte	**329.0 km**	**67.1 km**	**20.4 %**
All Formations	**1449.6 km**	**334.0 km**	**23.0 %**

lists the percentage of contact for each formation comparable to Petryk's interpretation. Obviously, the Vauréal basal contact was not compared since it is not even exposed on the island, the same with the Merrimack contact since it was added only recently to the stratigraphic framework defining the island succession.

The topographic marker associated to the basal contact of the Ellis Bay Formation in the northwestern part of the island was easily identified on the intensity image due to the effect of radar highlights and shadows. The topographic contrast between the uppermost recessive Schmitt Creek Member of the Vauréal Formation and the more resistant Grindstone Member at the base of the Ellis Bay Formation allowed locating and tracing precisely the stratigraphic contact between the two units. Slope angles extracted from the DEM were also used to better locate the formation contact. As illustrated in Figure 4-5, areas of shallow slope angles are associated with dipslopes of dipping beds whereas areas of steep slope angles are part of antidip scarps. The slope rupture between the dipslopes and the antidip scarps at the base of the topographic marker is where the recessive Schmitt Creek beds alternate with the relatively more resistant Grindstone strata and where the Ellis Bay contact was precisely mapped.

The recognition of the Ellis Bay basal contact in the north central and northeastern parts of the island between the Rivière-à-l'Huile and the Rivière-aux-Saumons was not obvious due to topographic inconsistency related to the marker beds.

Figure 4-5: Ellis Bay basal contact interpretation (*green line*) near Lac Simonne in the northwestern part of Anticosti Island:

(A) topographic SAR expression of the relatively more weathering resistant Ellis Bay basal members in comparison to the uppermost Vauréal units;
(B) contact adjustment in accordance to the slope angles image derived from the DEM.

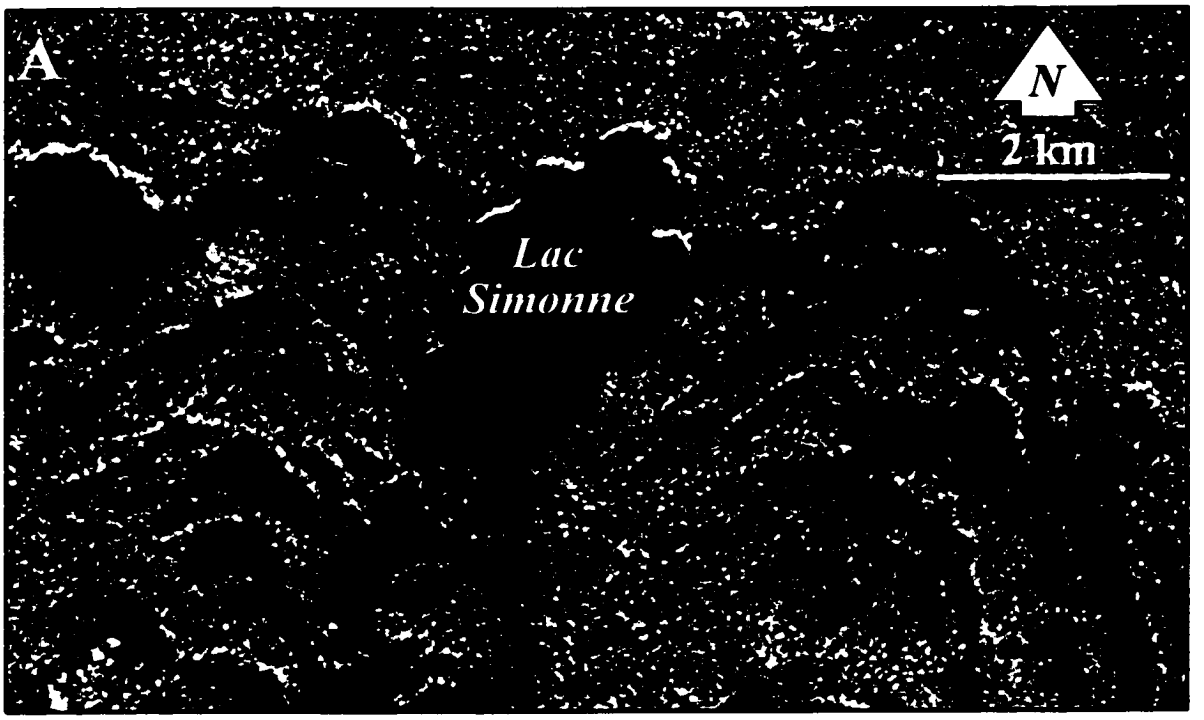
A
N
2 km
Lac
Simonne

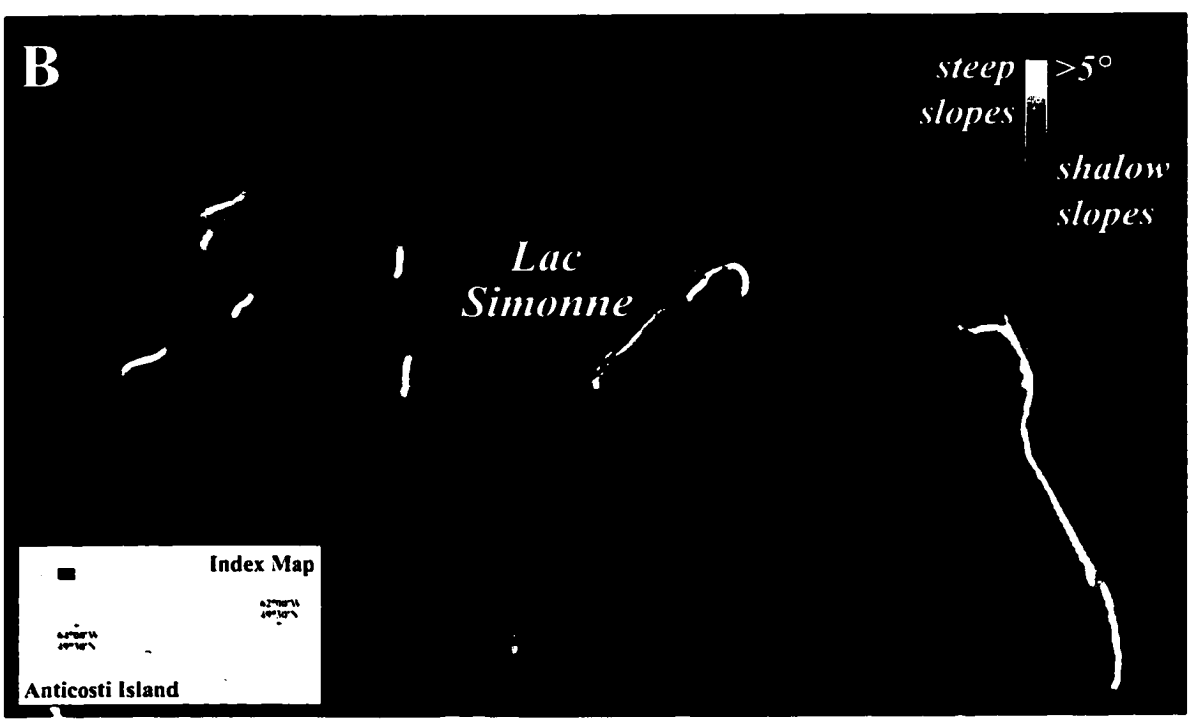
B
steep
slopes
>5°
shalow
slopes
Lac
Simonne
Index Map
Anticosti Island

Field observations and expert knowledge were essential to support the SAR interpretation in that particular region. It is also in that area that the most dissimilarity between the two sets of contacts was noticed. The new contact is, however, more reliable mainly in the surrounding of Rivière Vauréal where the former contact was simply mapped as presumed.

The Becscie basal contact, also corresponding to the Ordovician/Silurian boundary, is the formation contact that most matches Petryk's interpretation; 37.4 % of the time (Table 4-3). Like the Ellis Bay basal contact, its recognition in the north central part of the island was somewhat ambiguous, but it was nicely located in the northwestern and northeastern sectors of Anticosti. At Cap-de-la-Table, in the northeast, it was pegged to Petryk's contact where accessible coastal outcrops confirmed its position. Inland, however, the two sets of contacts were interpreted differently as illustrated in Figure 4-6. The new contact is more reliable since it follows nicely the escarpment produced by the resistant oncolite bed of the Laframboise Member within the Ellis Bay Formation and by the lowermost strata of the Becscie Formation. The topographic depression at the base of the escarpment is the result of the soft weathering Lousy Cove Member underlying the oncolite bed located near the top of the escarpment. It is based on the recognition of the topographic depression followed by the escarpment that the precise location of the contact was mapped. The SAR interpretation was validated at a number of sites along the newly developed road going east from Rivière-aux-Saumons to Cap-de-la-Table where it intersects several times the contact (Figure 4-6).

Figure 4-6: Contact locations of the new and former Becscie Formation near Cap-de-la-Table located in the northeastern part of Anticosti Island. Both contacts are identical at the coast, but are significantly different inland where the new Becscie (Ordovician/Silurian) contact follows in close relationship the SAR topographic expression.

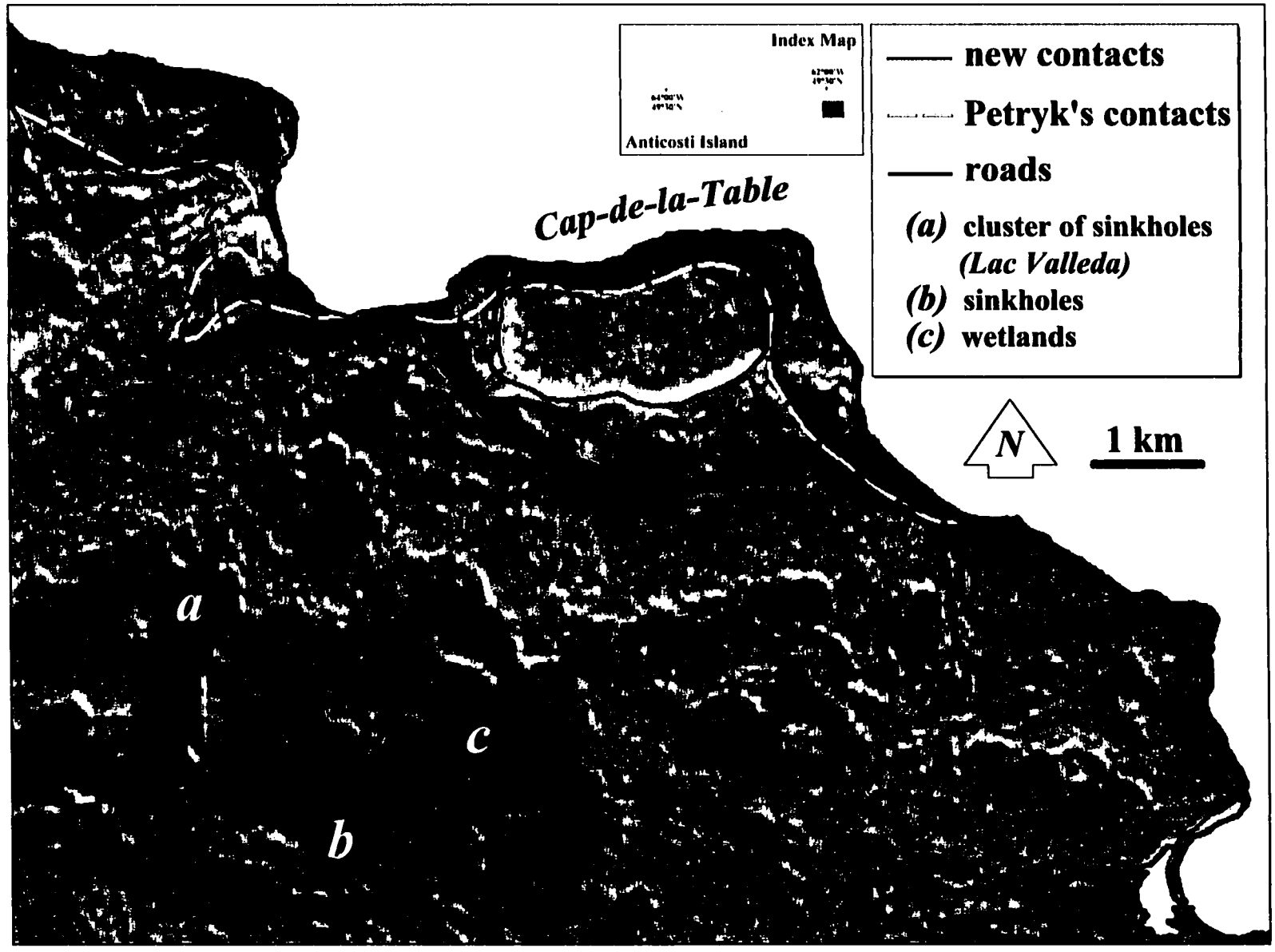
Index Map
Anticosti Island
Cap-de-la-Table
new contacts
Petryk's contacts
roads
(a) cluster of sinkholes
(Lac Valleda)
(b) sinkholes
(c) wetlands
N
1 km
a
b
c

It is fortunate that the Ordovician/Silurian boundary corresponds closely to the basal contact of the Becscie Formation; otherwise it would have been impossible to identify its existence by means of radar-mapping techniques alone. It should be noted here that such boundaries are defined on the basis of fossil content (biostratigraphy principles), but also on the ages of rocks where known stratigraphic units of worldwide extent can be related to geologic time (chronostratigraphy principles). SAR data are therefore unsuitable for such identifications since it cannot provide any information on fossil content, nor on the absolute age of the various stratigraphic units.

The Merrimack type section located along the eastern coast of Anticosti Island between Pointe Merrimack and Baie Innommée, as presented by Copper and Long (1989), was used to identify on the SAR image the topographic marker associated with its basal contact (Figure 4-7a). That topographic marker is the result of the soft weathering calcareous shales of the Merrimack Formation resting upon the resistant beds of the upper Chabot Member of the Becscie Formation. Unfortunately, it fades out rapidly inland to barely reappears to the west of the central plateau where the last calcareous shales of the formation outcrop at the mouth of Rivière-aux-Cailloux. Extrapolating the contact from one coast to the other with almost no topographic evidence and limited ground control required a great deal of assumptions based on different clues provided by the SAR image. For example, in the northeastern corner of the central plateau within the vicinity of Lake Wickenden and to the south of Rivière-aux-Saumons, the density of lakes and wetland areas appearing on the SAR

Figure 4-7: Topographic expression of the Merrimack (*green*) and Gun River (*red*) basal contacts on the wide-swath SAR image:

(A) SAR sub-scene showing the newly interpreted basal contacts of the two formations near Baie Innommée where the lowermost Lachute Member of the Gun River Formation is easily detectable;

(B) SAR sub-scene taken in the northeastern corner of the Anticosti central plateau showing the subtle topographic expression of the soft-weathering Merrimack Formation, but from which the density of lakes and their shape were used as radar clues to trace the basal contacts of both formations.

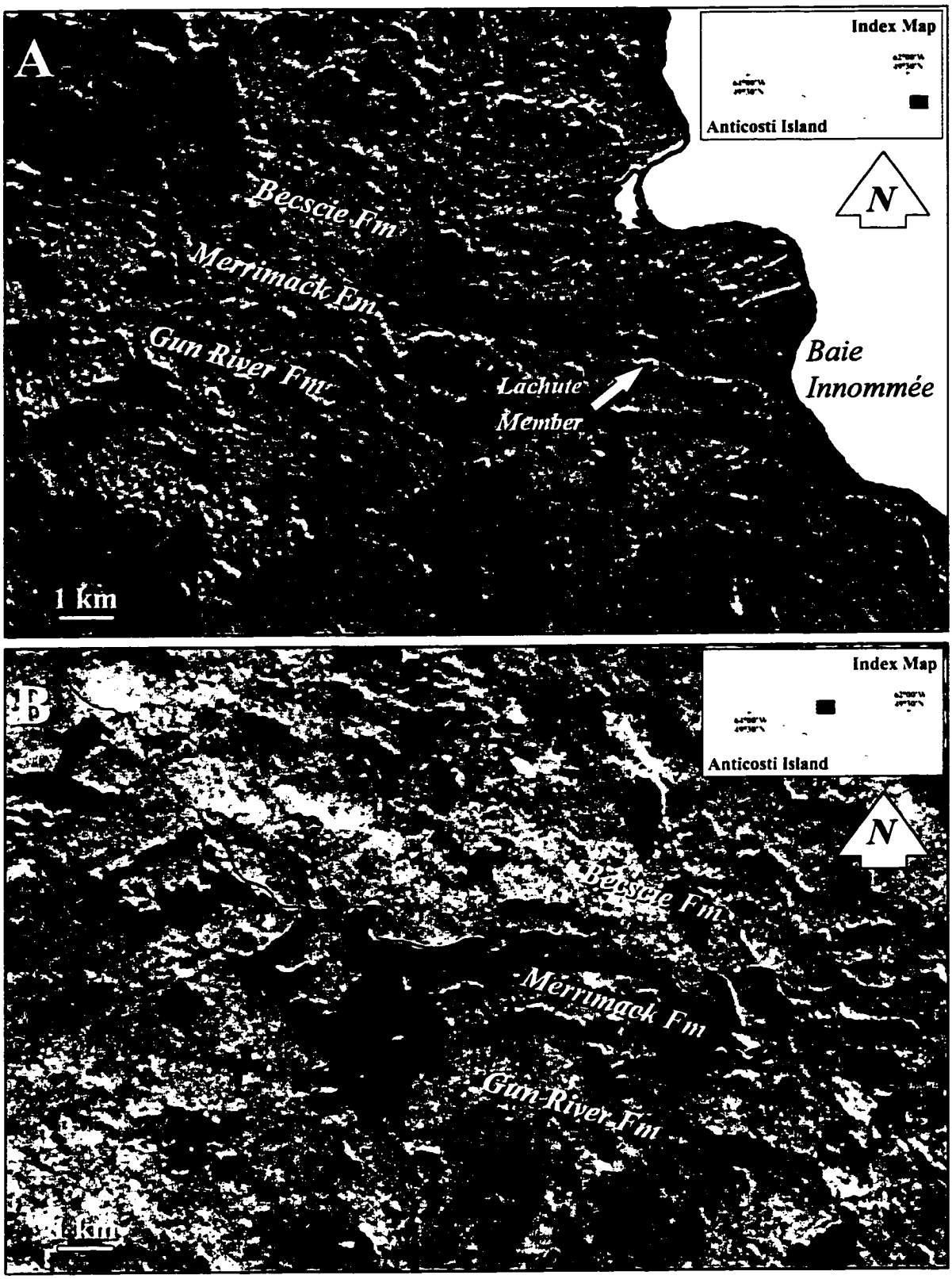
A
Index Map
Anticosti Island
N
Becscie Fm
Merrimack Fm
Gun River Fm
Lachute
Member
Baie
Innommée
1 km
B
Index Map
Anticosti Island
N
Becscie Fm
Merrimack Fm
Gun River Fm
1 km

image within the topographic depression associated with the soft weathering Merrimack Formation allowed locating its basal contact (Figure 4-7b).

The basal contact of the Gun River Formation concords 18.6 % of the time with Petryk's interpretation (Table 4-3). Once again, the mapping improvement is noticeable in areas where the topographic marker associated to the relatively more resistant Lachute Member was recognised on the SAR image (Figure 4-7a). However, in areas of subtle topography and where no ground control exits, the contact of the Gun River Formation was presumed to follow more or less in parallel the contact of the underlying Merrimack strata. That assumption was based on the fact that the Merrimack Formation is relatively thin (< 40 m) and that these two formations are conformable. It should be noted here that the basal contact of the Gun River did not changed much stratigraphically with the addition of the Merrimack Formation since the calcareous shales of the latest formation belonged originally to the Becscie Formation (Copper and Long, 1989).

Among all contacts, it is the Jupiter basal contact that shows the most differences with Petryk's interpretation since Copper and Long (1990) identified it 40 m lower in the island succession than where it was originally recognised. This could explain why 71.7 % of the former Jupiter contact was mapped as suggested only (Table 4-1). The only similarity between the two interpretations lies in the identification of the gigantic cuesta front within the central plateau as part of the formation contact.

Finally, the contact of the Chicotte Formation was the easiest one to identify in the field due to the abrupt change in lithology caused by the presence of abundant crinoid fragments. Unfortunately, that characteristic does not translate into any particular SAR response such as a distinct radar texture. The major improvement associated to the Chicotte contact comes mostly from the identification of an additional coral reef horizon within the formation that was uncertain until recently. The hard-weathering properties of these coral reefs influenced locally the topographic relief of the island, thus allowing their possible recognition on the SAR image and the derivative products. Figure 4-8a shows the new extent of the Chicotte Formation plotted on a SAR sub scene whereas Figure 4-8b points out the topographic expression of the new coral reef horizon.

By evaluating the mapping uncertainty and the positional error of the two sets of contacts, and by comparing them using specific examples, it was demonstrated that the SAR interpretation increased the precision to which the formation contacts were mapped.

4.1.4 Structural Interpretation

Only the most important structural lineaments interpreted from the SAR image were integrated into the new geology map presented earlier. This is including the full extent of the Jurassic dyke system originally recognised as two distinct vertical diabase intrusions locally outcropping near the Puyjalon Cliff on the north shore. It also includes lineaments

Figure 4-8A: SAR interpretation of the basal contact of the Chicotte Formation.

Figure 4-8B: SAR expression of the weathering resistant coral reef horizons (*arrows*) part of the Chicotte Formation.

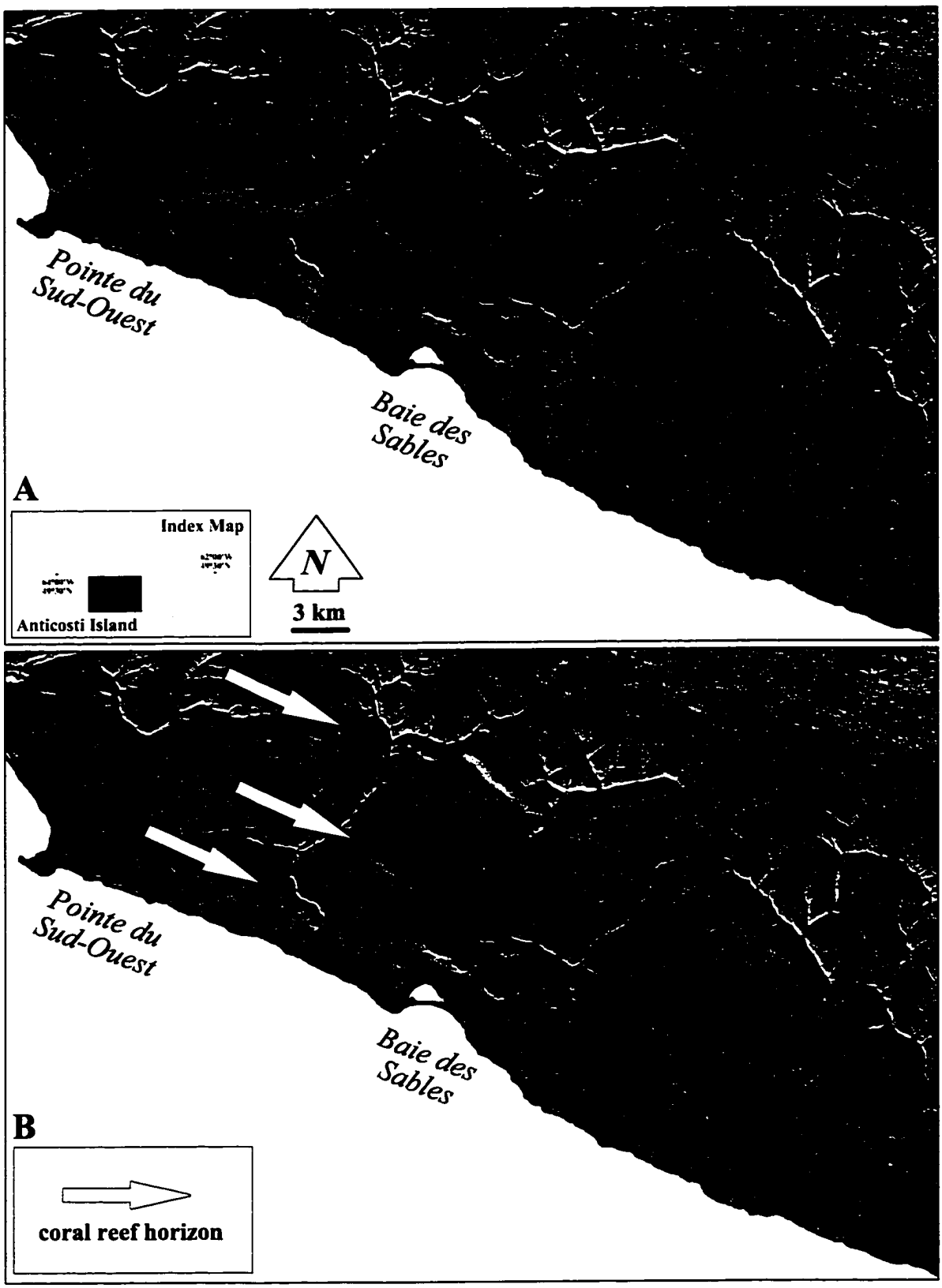
Pointe du Sud-Ouest
Baie des Sables
A
Index Map
Anticosti Island
N
3 km
Pointe du Sud-Ouest
Baie des Sables
B
coral reef horizon

interpreted as presumed minor normal faults with limited lateral extent and fractures of NNW and NE predominance, which have partly controlled the drainage network on Anticosti Island. Folds, like the ones identified on the geology map of Petryk, were not represented on the new map since the visual interpretation of the SAR image did not allow their recognition. Their occurrence is probably the result of deposition or compaction rather than the effect of a ductile deformation as originally presumed.

High-resolution aeromagnetic data would have been ideal to map in details the subsurface extent of the diabase intrusion; however, such geophysics information was not available here. Despite that limitation, the SAR image turned out to be quite useful in mapping the surface expression of the intrusion for a distance of approximately 40 km inland (Figure 4-9). The recognition of the dyke extension was possible because of a topographic depression associated to it (Figure 4-10a). It resulted from a combination of processes including the chemical weathering of the subsurface diabase rocks and the deformation of the enclosing carbonate rocks. Through dissolution, oxidation, and hydrolysis processes, the unstable ferromagnesian silicate parts of the diabase rocks were dissolved and altered by carbonic acid. The acid is the result of groundwater picking up the carbon dioxide from decaying organic matter within the thin layer of soil underneath the vegetation cover of Anticosti Island. It reaches the diabase by infiltrating the overlying carbonate rocks that were locally deformed by the increase of pressure and temperature during the dyke intrusion. Figure 4-10b shows two rock samples taken within the Vauréal Formation along the trans-Anticosti

Figure 4-9A: Topographic expression of the diabase dyke intrusion running from Puyjalon Cliff to the southeast sector of Lake Wikenden.

Figure 4-9B: SAR interpretation of the diabase dyke intrusion.

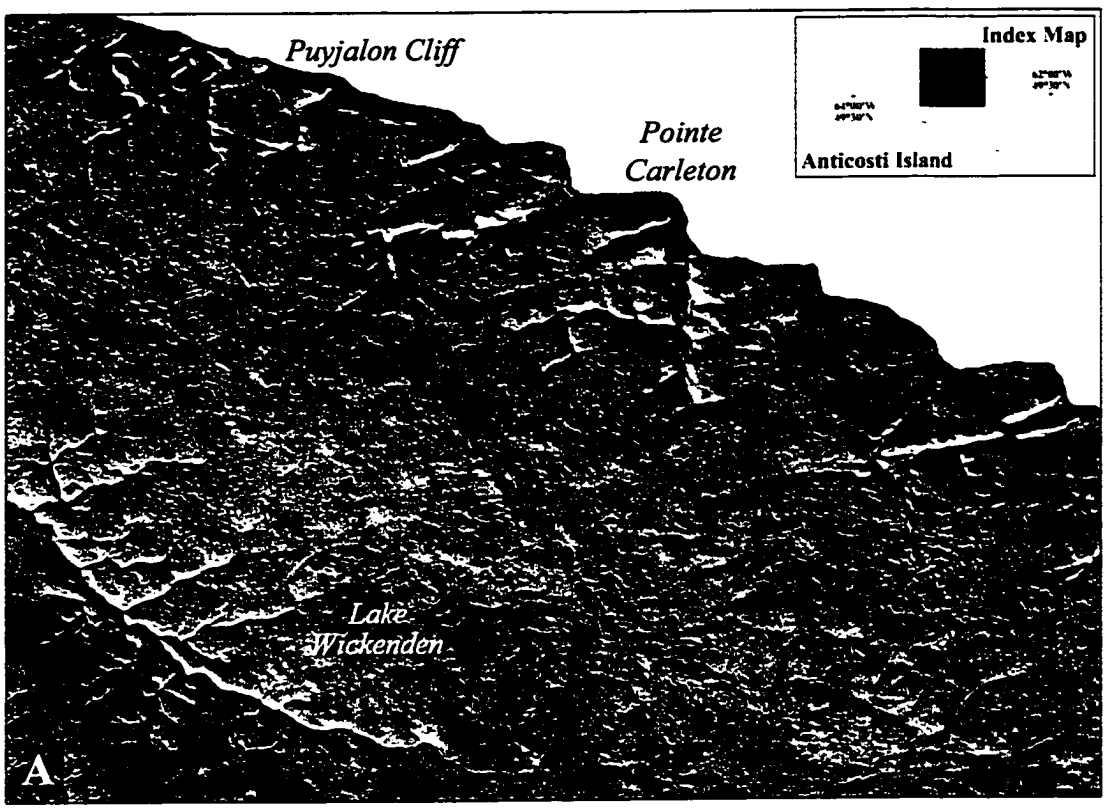
Puyjalon Cliff
Pointe
Carleton
Index Map
Anticosti Island
Lake
Wickenden
A

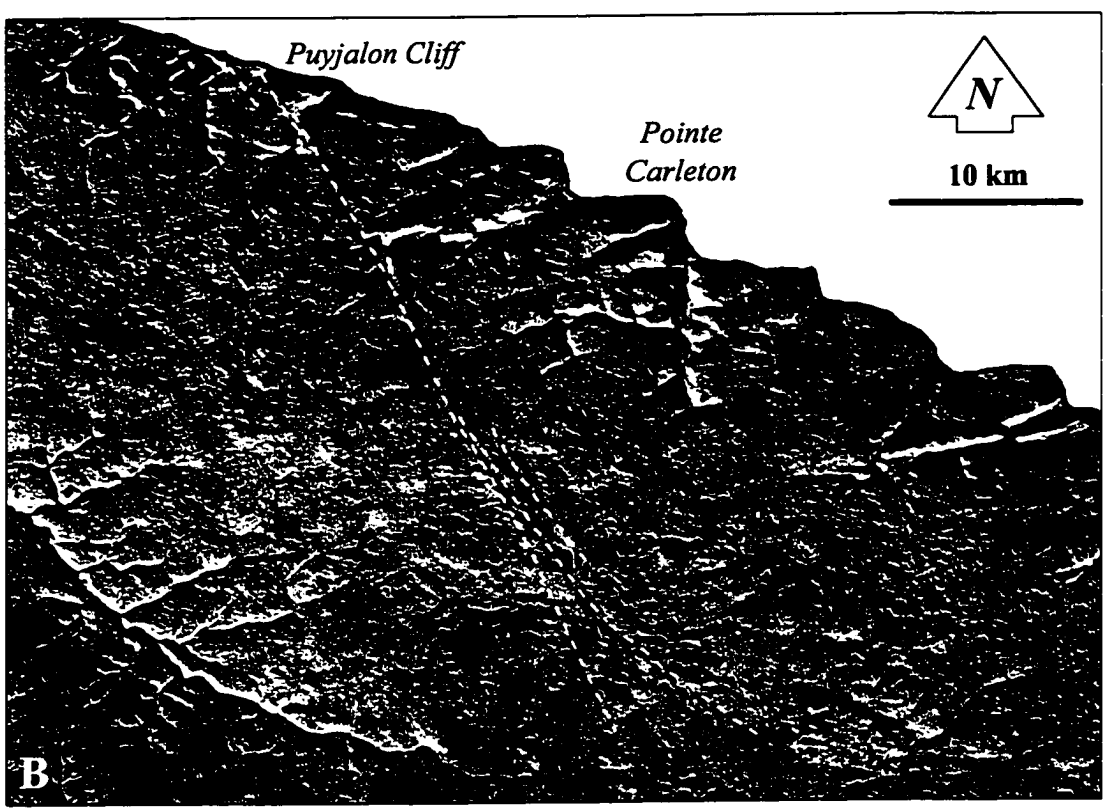
Puyjalon Cliff
Pointe
Carleton
N
10 km
B

Figure 4-10A: Field picture taken at the Puyjalon Cliff showing the locally outcropping diabase dyke. The arrowhead points out the topographic depression associated to the dyke intrusion.

Figure 4-10B: Two rock samples taken within the Vauréal Formation near the Puyjalon Cliff showing the structural fabric left by the deformation produced during the intrusion of the diabase dykes.

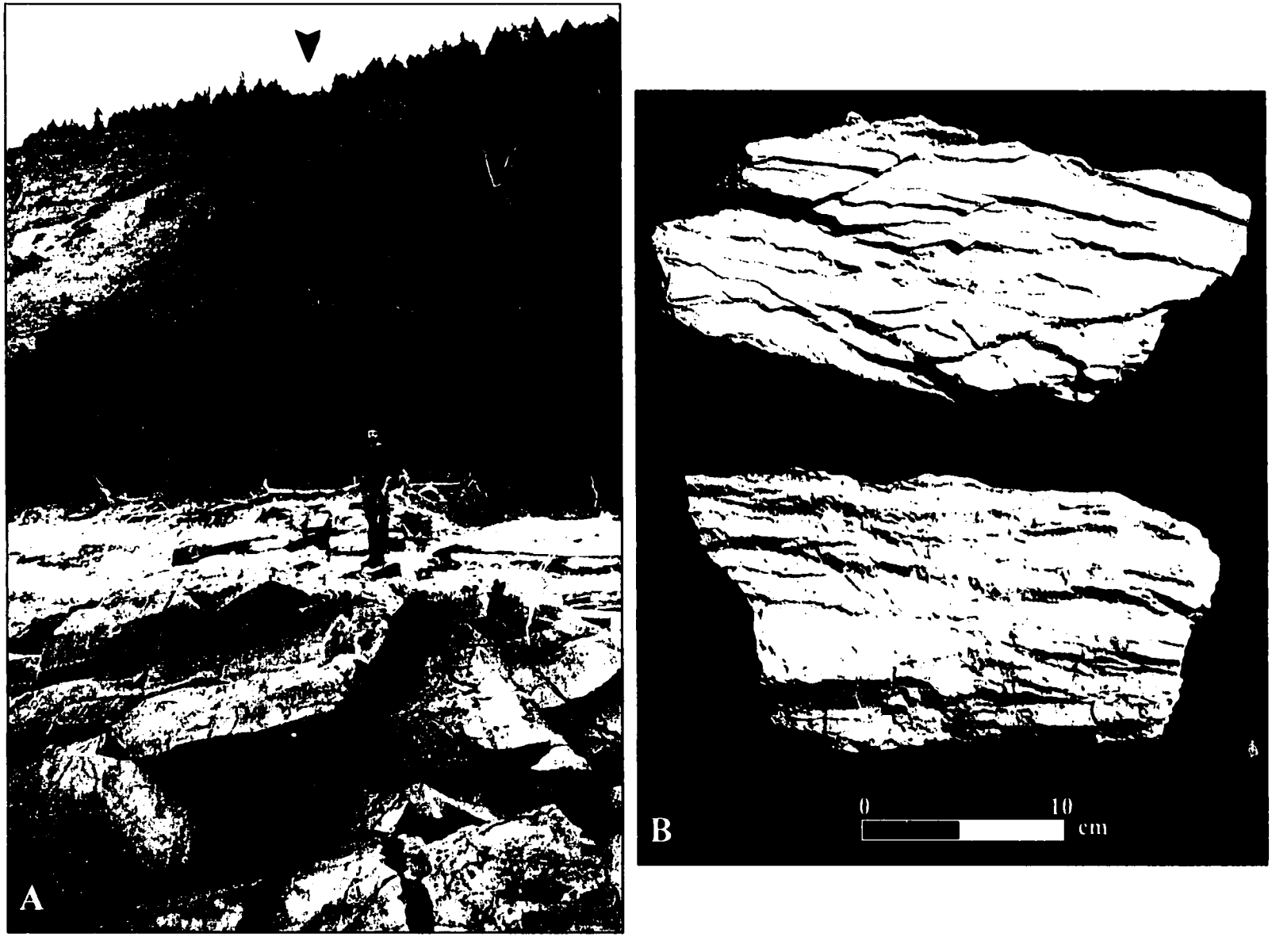
A
B
0
10
cm

road crossing over the dyke intrusion southeast of the Puyjalon Cliff where the structural fabric left by the deformation can be nicely recognised. The combination of the carbonate rock deformation and the diabase dissolution and alteration has therefore resulted in a zone of weakness. With differential erosion, a topographic depression detectable on the SAR image was produced along the dyke system (Figure 4-9). This is another good example showing the potential of SAR data to improve the geology in forested areas like Anticosti Island.

4.2 Results of the Fully Polarimetric SAR Data Analysis

This section presents the results obtained from the analysis of the fully polarimetric SAR data acquired in 1998 over the northwestern part of Anticosti Island. These results were not used to produce the new geology map of the island, but instead to evaluate the mapping potential of SAR polarisation over densely forested areas.

The co- and cross-polarisation responses, the pedestal height, and the backscatter coefficients (σ°) at linear and circular polarisations were considered sufficient to investigate any existing relationships between the preferential distribution of the three most important forest stands over two different types of soil covering both Vauréal and Ellis Bay formations. Combining these three forest stands with the two types of soil, and the two stratigraphic formations allowed defining 12 different categories of scattering elements (Figure 3-12) from which 5 to 10 polarimetric samples per category were collected. Unfortunately, no samples were found within the category consisting of white spruce stand growing on thin organic soil over the

bedrock of the Ellis Bay Formation (Appendix C), and as a consequence, it was not used for comparison purposes. The extracted polarimetric information for the 11 remaining classes is hereafter described.

4.2.1 Co- and Cross-Polarimetric Responses and Pedestal Heights

The extracted co- and cross-polarisation responses for each radar sample are provided in 3D polarisation plots. These plots characterize the SAR responses at linear, circular, and elliptically polarised configurations. They sit on a pedestal where its normalized height is a measure of the importance of the radar unpolarised scattering component. The shape of the plots is controlled by the maximum and minimum values of the co- and cross-polarisations in every possible orientation (ψ) and ellipticity (χ) angles. It is an indicator of the scattering mechanisms dominating the target response.

The mean value of the maximum and minimum co- and cross-polarisations along with the pedestal heights and the incidence angles for each category are listed in Table 4-4. Their analysis and interpretation are hereafter supported with typical 3D plots. Since it was impossible to synthesise the calculated mean values into new 3D plots, only the most representative plots for each category were selected (Figures 4-11a, b, c, and d). The original statistics of every extracted polarimetric sample within each scattering category can be found in Appendix C.

Table 4-4: List of the mean values for the linear and circular co- and cross-polarisations, pedestal heights, and incidence angles of the polarimetric responses extracted from the 12 scattering categories of vegetation, soil, bedrock.

Vegetation	Surface Geology	Formation	HH σ°	HV σ°	VV σ°	RR σ°	RL σ°	LL σ°	Co-Pol Max Ψ	Co-Pol Max γ	Co-Pol Min Ψ	Co-Pol Min γ	Pedestal (Co-Pol)	X-Pol Max Ψ	X-Pol Max γ	X-Pol Min Ψ	X-Pol Min γ	Pedestal (Cross-Pol)	Mean Inc. Angle (°)
Balsam Fir	Organic Soil	Vauréal	-11.52	-19.63	-12.58	-16.60	-12.82	-17.08	175	0	63	-40	0.30	45	-43	8	1	0.21	65.1
		Ellis Bay	-9.10	-16.96	-10.20	-13.43	-10.72	-13.56	174	-1	115	-37	0.32	45	-38	107	-4	0.22	52.3
	Glacial Till	Vauréal	-11.71	-19.73	-12.76	-16.56	-13.10	-16.56	179	0	113	-44	0.31	46	-40	13	2	0.21	66.4
		Ellis Bay	-9.52	-17.41	-10.31	-14.14	-10.87	-14.13	179	0	58	-39	0.32	45	-40	85	1	0.21	55.6
Black Spruce	Organic Soil	Vauréal	-10.60	-18.47	-11.48	-15.36	-11.92	-15.33	175	-1	63	-41	0.32	48	-43	21	2	0.22	62.8
		Ellis Bay	-8.48	-16.33	-9.67	-13.00	-10.05	-13.12	178	-1	122	39	0.32	48	-39	160	-4	0.23	52.0
	Glacial Till	Vauréal	-11.81	-20.32	-13.60	-16.99	-13.57	-16.96	177	-1	63	-37	0.27	45	-39	85	1	0.21	69.1
		Ellis Bay	-9.39	-17.05	-10.31	-13.81	-10.85	-13.86	173	0	58	-41	0.34	43	-44	101	0	0.24	55.4
White Spruce	Organic Soil	Vauréal	-11.27	-19.34	-12.48	-16.15	-12.76	-16.13	179	0	65	-41	0.31	45	-43	0	0	0.22	66.1
		Ellis Bay	/	/	/	/	/	/	/	/	/	/	/	/	/	/	/	/	/
	Glacial Till	Vauréal	-11.87	-20.24	-13.42	-16.83	-13.58	-16.77	0	0	65	-37	0.29	45	-39	0	0	0.21	68.6
		Ellis Bay	-9.31	-17.18	-10.31	-13.91	-10.77	-13.92	179	0	115	41	0.32	45	-42	41	0	0.22	55.4

Figure 4-11A: 3D plots of the co- and cross-polarimetric responses of the balsam fir, black spruce, and white spruce forest stands growing on organic soil within the Vauréal Formation.

Figure 4-11B: 3D plots of the co- and cross-polarimetric responses of the balsam fir, black spruce, and white spruce forest stands growing on glacial till within the Vauréal Formation.

Figure 4-11C: 3D plots of the co- and cross-polarimetric responses of the balsam fir, black spruce, and white spruce forest stands growing on organic soil within the Ellis Bay Formation.

Figure 4-11D: 3D plots of the co- and cross-polarimetric responses of the balsam fir, black spruce, and white spruce forest stands growing on glacial till within the Ellis Bay Formation.

(A) Vauréal Formation

Organic Soil

Balsam Fir

Black Spruce

White Spruce

(B) Vauréal Formation

Glacial Till

Balsam Fir

Black Spruce

White Spruce

(C) Ellis Bay Formation

Organic Soil

Balsam Fir

Black Spruce

White Spruce

No Polarimetric Response

(D) Ellis Bay Formation

Glacial Till

Balsam Fir

Black Spruce

White Spruce

As illustrated in table 4-4 and in the associated 3D plots, all polarimetric responses are linearly polarised with a stronger component in HH ($\psi = 0°$ or $180°$) than in VV ($\psi = 90°$). Consequently, the saddle shape similarity between the co-polarisation plots suggests a comparable scattering mechanism for all coniferous species independently of the type of soils and the stratigraphy. The architecture of the coniferous trees is not that different from one another since it is the horizontal predominance of the twigs and branches that influenced the most the radar energy. The vertical component of the polarimetric responses occurred only when the radar signal was able to reach the trunk of the trees. The linearity of the polarisation responses suggests that almost no significant depolarisation of the radar signal occurred. Among the typical 3D plots, it is the minimum cross-polarisation that shows the more variables in orientation angles (ψ) between the 11 categories (Table 4-4) suggesting a greater sensitivity of that component to the selected targets.

The pedestal heights on which the 3D plots sit are also similar between the 11 sampled categories. On average, the pedestal heights of the three coniferous species are identical independently of the type of soils and the stratigraphy. The only difference comes from the co- and the cross-polarisations with mean normalized pedestal heights of 0.31 and 0.22 respectively. Such pedestal heights suggest that 31 % of the co-polarisation response and 22 % of the cross-polarisation response are in fact unpolarised. It also confirms that surface scattering within the upper part of the forest canopy contributed the most to the polarimetric responses than volume scattering. The short wavelength of the C-band SAR data, thus the limited radar penetration through the forest canopy, is responsible for that.

4.2.2 Backscatter Coefficient (σ°)

The mean backscatter coefficients (σ°) at linear and circular polarisations for the 11 categories are illustrated in Figure 4-12. As it can be seen, the HH, VV, and RL polarisations are similar with less than 2.0 dB in σ° variations. On average, they have the strongest returned signals at -12.4 dB in the Vauréal Formation and at -10.0 dB in the Ellis Bay Formation. Once again, that strong signal return in HH and VV is the result of the predominating horizontal twigs and branches of the coniferous trees supported by a vertical trunk. The RL cross-circular polarisation is also sensitive to the scattering architecture of the coniferous trees. The RR and LL co-circular polarisations are identical with less than 0.5 dB of σ° variations. Their signal is 4 to 5 dB weaker than the RL cross-circular polarisation. This difference is suggesting that double bounce effect representative of the volume scattering is less significant than the predominating single bounce effect of the surface scattering. The HV polarisation, for its part, shows the lowest σ° with an average of -19.6 dB in the Vauréal Formation and -17.0 dB in the Ellis Bay Formation.

Independently of the type of polarisation and of the stratigraphic formation, the black spruce growing directly on a thin organic soil (bedrock) shows a subtle, but stronger backscatter coefficient than the two other coniferous species growing on organic soil or on glacial till. Even the same black spruce growing on glacial till does not show such strong backscatter coefficient. It can be therefore presumed that the type of soil on which the black spruce is

Figure 4-12: Diagram representing the backscatter coefficient (σ°) of the 12 scattering categories extracted from the *L4P3* fully polarimetric SAR data.

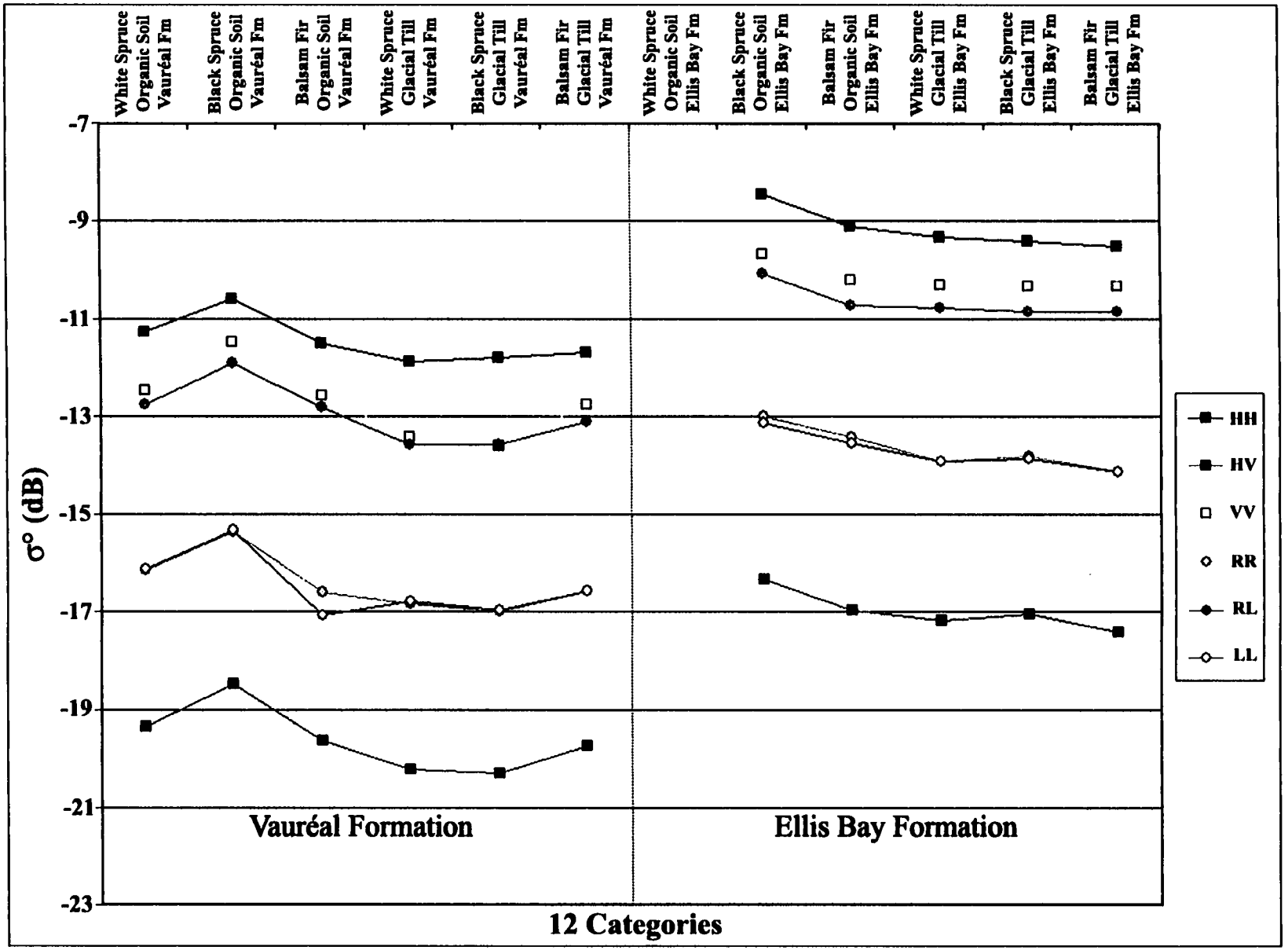
White Spruce Organic Soil Vauréal Fm
Black Spruce Organic Soil Vauréal Fm
Balsam Fir Organic Soil Vauréal Fm
White Spruce Glacial Till Vauréal Fm
Black Spruce Glacial Till Vauréal Fm
Balsam Fir Glacial Till Vauréal Fm
White Spruce Organic Soil Ellis Bay Fm
Black Spruce Organic Soil Ellis Bay Fm
Balsam Fir Organic Soil Ellis Bay Fm
White Spruce Glacial Till Ellis Bay Fm
Black Spruce Glacial Till Ellis Bay Fm
Balsam Fir Glacial Till Ellis Bay Fm
-7
-9
-11
-13
-15
-17
-19
-21
-23
σ° (dB)
Vauréal Formation
Ellis Bay Formation
12 Categories
HH
HV
VV
RR
RL
LL

growing has something to do with its spatial distribution and consequently influenced its scattering mechanisms. It is certainly not the result of a polarimetric error since several samples in each category were used to calculate the mean σ° and since the same backscatter profile appears in both formations. Further investigations are, however, required in order to determine if forest perturbations of natural or artificial causes could be responsible for such σ° variation.

One last, but very important observation is the σ° difference of 2.0 to 3.0 dB between the Ellis Bay and Vauréal formations. This could suggest a preferential distribution of the coniferous trees with respect to bedrock geology, however, it is impossible at this point to determine if it is really the case. One thing for sure is that the incidence angle of the SAR data contributed partially to that backscatter offset. The parallelism of the northwest trending formations with the flight direction of the *L4P3* fully polarimetric SAR data resulted in an inadequate configuration where the Ellis Bay basal contact fell quite pretty close to the limit between the near range and the far range of the radar swath. Therefore, all polarimetric samples within the Vauréal Formation were taken between 63° to 69° of incidence angles whereas these taken in the Ellis Bay Formation were ranging between 52° and 62° (Table 4-4).

4.2.3 Polarimetric Recommendations

The absence of a strong polarimetric discrimination among the various selected categories was expected since the three forest stands of coniferous trees have a similar scattering mechanism as well as the two carbonate formations that are lithologically similar. To overcome that lack of variability, fully polarimetric SAR data acquired in multi-frequency mode (X-, C-, and L-band for example) would have probably allowed a greater discrimination of the vegetation cover, the type of soil, and the bedrock geology on Anticosti Island. Since such multi-frequency data sets were not available for this study, the only possible way to determine the source of 2.0 to 3.0 dB variations between the σ° of the Vauréal and the Ellis Bay formations would be to analyze the fully polarimetric SAR data acquired perpendicularly to the formation contacts. With such configuration, radar samples taken in different formations could have the same incidence angle since the swath range would vary in the direction as the orientation of bedding planes. Advanced polarimetric parameters along with more detailed vegetation and surface geology maps including information on the topographic relief, the hydrology, and the natural and artificial forest perturbations of the island, should all be considered to better evaluate the potential of fully polarimetric SAR data for mapping the geology of the forested Anticosti Island.

5. Conclusions

The use of airborne C-band SAR data acquired in a wide-swath configuration and in a single polarisation (HH) mode was proven valuable for the first approach of this study to support the geological mapping of the densely forested Anticosti Island. The distinctive cuesta morphology associated with the weathering resistant and recessive gently dipping strata of the island was nicely enhanced with the radar highlight and shadow effects provided by the side-looking capability of the Convair-580 SAR system and its sensitivity to the low frequency details defined by the macro-scale surface roughness of the island topography. Furthermore, the dense and homogeneous boreal forest covering almost 95 % of the Anticosti territory did not prevent the C-band SAR system from imaging the terrain characteristics, even though rapid saturation occurred in the forest canopy. This is due to the relatively uniform tree height of the forest stands mimicking closely the underlying bedrock topography. Therefore, locating and tracing the formation contacts along with the structural geology, including the full inland extent of the diabase dyke, was possible based on the radar principles and using the appropriate system configuration with respect to the terrain characteristics.

The accuracy at which the new stratigraphic mapping was achieved in this study was not quantified because of the qualitative approach of the wide-swath SAR image interpretation; however, it was proven by means of expert knowledge and field validations to be more consistent than what traditional mapping campaigns failed to achieve. The close relationship

between the new formation contacts and the topographic expression of the dipping strata also supports this argument of higher mapping accuracy using radar image interpretation techniques.

Similar interpretation techniques can be used to conduct geological mapping over densely forested regions of different geological setting as long as the underlying bedrock geology has some control on the topographic expression of the terrain and that adequate SAR system parameters are selected accordingly (more specifically those defining the system viewing geometry). SAR can be even more valuable in regions where a lack of topographic information exists, since DEM can be generated from radargrammetric techniques using stereoscopic SAR images.

The second approach of this study, even though only experimental, was inconclusive. The lack of results in the polarimetric analysis of the fully polarimetric SAR data did not allowed to identify any preferential distribution of the vegetation cover with respect to the underlying surface deposits and bedrock geology of Anticosti Island. However, the backscatter variation of 2.0 to 3.0 dB between the Vauréal and the Ellis Bay polarimetric samples, independently of the type of coniferous trees and soils, is significant enough to continue the research in that domain. In the future, it would be preferable to use fully polarimetric flight lines acquired perpendicularly to the formation contacts and in multi-frequency polarisation mode in order to eliminate the incidence angle effect and to increase radar penetration.

References

BARNES, C.R. and A.D. McCracken, 1981. Early Silurian Chronostratigraphy and a Proposed Ordovician-Silurian Boundary, Ellis Bay Formation, Anticosti Island, Québec. *In* P.J. Lespérance (editor) I.U.G.S. Field meeting, Anticosti-Gaspé, Québec, 1981. Volume II. Stratigraphy and Paleontology. Département de géologie, université de Montréal, pp. 71-80.

BARNES, C.R., 1988. Stratigraphy and Palaeontology of the Ordovician-Silurian Boundary Interval, Anticosti Island, Québec, Canada. Bulletin British Museum Natural History (Geology), Vol. 43, pp. 195-219.

BARNES, C.R., 1989. Lower Silurian Chronostratigraphy of Anticosti Island, Quebec. *In* C.H. Holland and M.G. Basset (editors) A Global Standard for the Silurian System. National Museum of Wales, Geological Series 9, pp. 101-108.

BÉDARD, J.H., 1992. Jurassic quartz-normalative tholeiite dykes from Anticosti Island, Québec. *In* J.H. Puffer and P.C. Ragland (editors), Eastern North American Mesozoic magmatism. Geological Society of America, Special Paper 268, pp. 161-167.

BERTRAND, R., 1990. Maturation thermique et histoire de l'enfouissement et de la génération des hydrocarbures du bassin de l'archipel de Mingan et de l'île d'Anticosti, Canada. Canadian Journal of Earth Sciences, Vol. 27, pp. 731-741.

BLOM, R.G., L.R., Schenck, and R.E. Alley, 1987. What are the Best Radar Wavelengths, Incidence Angles, and Polarizations for Discrimination Among Lava Flows and Sedimentary Rocks? A Statistical Approach. IEEE Transactions on Geoscience and Remote Sensing, Vol. GE-25, No. 2, pp. 208-213.

BOERNER, W.-M., H. Mott, E. Luneburg, C. Livingstone, B. Brisco, R.J. Brown, and J.C. Patterson, 1998. Polarimetry in Radar Remote Sensing: Basic and Applied Concepts. Chapter 5, *In* F.M. Henderson and A.J. Lewis (editors), Principles and Applications of Imaging Radar, Manual of Remote Sensing, John Wiley and Sons Inc., 3rd Edition, Vol. 2, pp. 511-565.

BOLTON, T.E., 1961. Ordovician and Silurian Formations of Anticosti Island, Québec. Geological Survey of Canada, Paper 61-26, 18 p.

BOLTON, T.E., 1965. Stratigraphy of Anticosti Island, Québec. Geological Survey of Canada, Paper 65-1, pp. 113-114.

BOLTON, T.E., 1970. Silurian-Ordovician Macrobiostratigraphy of Anticosti Island, Québec (12E,F). Geological Survey of Canada, Paper 70-1, pp. 107-108.

BOLTON, T.E., 1972. Geological Map and Notes on the Ordovician and Silurian Litho- and Biostratigraphy, Anticosti Island, Québec. Geological Survey of Canada, Paper 71-19, 45 p. (Map 2-1971).

BRUNTON, F.R. and P. Copper, 1994. Paleoecologic, Temporal, and Spatial Analysis of Early Silurian Reefs of the Chicotte Formation, Anticosti Island, Quebec, Canada. Facies, Vol. 31, pp. 57-80.

CARBONI, S., 1988. Photointerpretation et analyse d'image des linéaments photogéologiques de l'île d'Anticosti, Québec. M.Sc. thesis, École Polytechnique, Montréal, 126 p.

COCKS, L.R.M. and P. Copper, 1981. The Ordovician-Silurian Boundary at the Eastern End of Anticosti Island. Canadian Journal of Earth Sciences, Vol. 18, pp. 1029-1034.

COPELAND, M.J. and T.E. Bolton, 1975. Geology of the Central Part of Anticosti Island, Québec. Geological Survey of Canada, Paper 75-1, pp. 519-523.

COPPER, P., 1981. Atrypoid brachiopods and their distribution in the Ordovician – Silurian sequence of Anticosti Island. *In* P.J. Lespérance (editor) I.U.G.S. Field meeting, Anticosti-Gaspé, Québec, 1981. Volume II Stratigraphy and paleontology. Département de géologie, Université de Montréal, pp. 137-142.

COPPER, P., 1989. Upper Ordovician and Lower Silurian Reefs of Anticosti Island, Québec. *In* H.H.J. Geldsetzer, N.P. James, and G.E.Tebbutt (editors), Reefs, Canada and adjacent areas. Canadian Society of Petroleum Geologists, Memoir 13, pp. 271-276.

COPPER, P. and D.G.F. Long, 1989. Stratigraphic revision of a key Ordovician-Silurian boundary section, Anticosti Island, Canada. Newsletters in Stratigraphy, Vol. 21, pp. 59-73.

COPPER, P. and D.G.F. Long, 1990. Stratigraphic revision of the Jupiter Formation, Anticosti Island, Canada: a major reference section above the Ordovician-Silurian boundary. Newsletter of Stratigraphy, Vol. 23, No. 1, pp. 11-36.

COPPER, P. and J. Jisuo, 1995. Field Guide to the Ordovician-Silurian Brachiopods of Anticosti Island, Eastern Canada. 3rd International Brachiopod Congress, 25-30 August 1995, 28 p.

CÔTÉ, D., J.M.M. Dubois, and Q.H.J. Gwyn, 1990. Mysterious Lakes; Anticosti Island, a unique example of karst topography in eastern Canada, has lakes that vary in level and even disappear. GEOS, Vol. 19, No. 3, pp. 20-25.

DESROCHERS, A., E. Gauthier, and M. D'Iorio, 1997. Enhancement of the Geological Mapping of Anticosti Island, Gulf of St-Lawrence Using Airborne SAR Data. *In* Proceedings of the International Symposium on Geomatics in the Era of RADARSAT, Ottawa, Ontario, 1997, 16 p.

DESROCHERS, A., P. Copper, and D.G.F. Long, 1998. Sedimentology and Paleontology of the Early Ordovician Through Early Silurian Shallow Water Carbonates of the Mingan Islands National Park and Anticosti Island, Québec. Field Trip Guidebook B8. Geological Association of Canada/Mineralogical Association of Canada, Joint Annual Meeting, Québec, Québec, 20-26 May 1998, 97 p.

DUBOIS, J.-M.M., Q.H.J. Gwyn, P. Bigras, D. Gratton, S. Perras, and L. St-Pierre, 1990. Géologie des formations en surface, île d'Anticosti, Québec. Geological Survey of Canada, Map 1660A, 1:250 000.

DUFFIELD, S.L. and Legault, J.A., 1981. Acritarch biostratigraphy of Upper Ordovician – Lower Silurian rocks, Anticosti Island, Québec; preliminary results. *In* P.J. Lespérance (editor) I.U.G.S. Field meeting, Anticosti-Gaspé, Québec, 1981. Volume II Stratigraphy and paleontology. Département de géologie, Université de Montréal, pp. 91-99.

EVANS, D.L., T.G. Farr, J.P. Ford, T.W. Thompson, and C.L. Werner, 1986. Multipolarization Radar Images for Geologic Mapping and Vegetation Discrimination. IEEE Transactions on Geoscience and Remote Sensing, Vol. GE-24, No. 2, pp. 246-257.

EVANS, D.L., T.G. Farr, J.J. Van Zyl, and H.A. Zebker, 1988. Radar Polarimetry: Analysis Tools and Applications. IEEE Transactions on Geoscience and Remote Sensing, Vol. 26, number 6, pp. 774-789.

FAHRAEUS, L. and C.R. Barnes, 1981. Conodonts from the Becscie and Gun River formations (Lower Silurian) of Anticosti Island, Qu/bec. *In* P.J. Lespérance (editor) I.U.G.S. Field meeting, Anticosti-Gaspé, Québec, 1981. Volume II Stratigraphy and paleontology. Département de géologie, Université de Montréal, pp. 165-172.

FORD, J.P., R.G. Blom, J.L. Coleman, T.G. Farr, J.J. Plaut, H.A. Pohn, and F.F. Sabins, 1998. Radar Geology. Chapter 10, *In* Henderson, F.M., and A.J. Lewis (editors), Principles and Applications of Imaging Radar, Manual of Remote Sensing, John Wiley and Sons Inc., 3rd Edition, Vol. 2, pp. 511-565.

GRATTON, D., Q.H.J. Gwyn, and J.M.M. Dubois, 1984. Les paléoenvironnements sédimentaires au Wisconsinien Moyen et Supérieur, île d'Anticosti, Golfe du Saint-Laurent, Québec. Géographie physique et Quaternaire, Vol. 38, No. 3, pp. 229-242.

GRATTON, D., J.M.M. Dubois, A. Painchaud, and Q.H.J. Gwyn, 1986. Did the Laurentide Ice Sheet Reach Anticosti Island? GEOS, Vol. 15, No. 1, pp. 21-23.

HAWKINS, R.K. and K.P. Murnaghan, 1998. Data Report and Analysis Recommendations for SAR-580 Acquisition - November 22-26, 1998. Canada Centre for Remote Sensing, Internal Data Report # CCRS-TN-1998-26, 21 p.

HAWKINS, R.K., R. Touzi, A. Wind, K.P. Murnaghan, and C.E. Livingstone, 1999a. Polarimetric Calibration Results and Error Budget for SAR-580 System. *In* Proceedings of the CEOS SAR Workshop, ESA SP-450, October 1999, 6 p.

HAWKINS, R.K., R. Touzi, and C.E. Livingstone, 1999b. Calibration and Use of CV-580 airborne Polarimetric SAR Data. Presented at the 14th International Airborne Remote Sensing Conference and exhibition, 21st Canadian Symposium on remote Sensing, Ottawa, Ontario, 21-24 June 1999, pp. II32-II40.

HAWKINS, R.K., A. Wind, K.P. Murnaghan, J.R. Gibson, S. Nedelcu, and C.E. Brown, 2002. Processing of the C-Band Polarimeter on the Environment Canada CV-580 – A Review. *Submitted to* «Advances in Space Research», 10 p.

HAWORTH, R.T. and J.B. MacIntyre, 1977. Gravity and Magnetic Fields of the Gulf of St.Lawrence, Canada. Marine Sciences Paper 15, Geological Survey of Canada, Paper 75-42, 11 p.

HAWORTH, R.T., 1978. Interpretation of geophysical data in the northern Gulf of St. Lawrence and its relevance to lower Paleozoic geology. Geological Society of America Bulletin, Vol. 89, p. 1091 – 1110.

HAYWARD, N., S.A. Dehler, and G.N. Oakey, 2001. The Structure of the Northeastern Gulf of St.Lawrence, Canada: New Insight from Geophysical Data analysis. Canadian Journal of Earth Sciences, Vol. 38, pp. 1495-1516.

JENSEN, J.R., 1996. Introductory Digital Image Processing: A Remote Sensing Perspective. 2nd Edition, Prentice Hall Series in Geographic Information Science, K.C. Clarke (Editor), Upper Saddle River, New Jersey, 316 p.

LAROCHELLE, A., 1971. Note on the paleomagnetism of two diabase dykes, Anticosti Island, Québec. Geological Association of Canada, Proceedings 23, pp. 73-76.

LAURIOL, B., B. Hétu, D. Côté, and Q.H.J. Gwyn, 1985. Phénomènes karstiques et périglaciaires dans un lac à niveau variable de l'île d'Anticosti-Québec-Canada. Zeitschrift für Geomorphologie, Vol. 29, pp. 353-365.

LAVOIE, M. and L. Filion, 2001. Holocene Vegetation Dynamics of Anticosti Island, Québec, and Consequences of Remoteness on Ecological Succession. Quaternary Research, Vol. 56, pp.112-127.

LECKIE, D.G. and K.J. Ranson, 1998. Forestry Applications Using Imaging Radar. Chapter 9, *In* F.M Henderson and A.J. Lewis (editors), Principles and Applications of Imaging Radar, Manual of Remote Sensing, John Wiley and Sons Inc., 3rd Edition, Vol. 2, pp. 461-509.

LESPÉRANCE, P.J., 1985. Faunal distributions across the Ordovician-Silurian boundary, Anticosti Island and Percé, Québec, Canada. Canadian Journal of Earth Sciences, Vol. 22, p. 838–849.

LEWIS, A.J., F.M., HENSERSON, AND D.W. HOLCOMB. 1998. Radar Fundamentals: The Geoscience Perspective. Chapter 3 *In* F.M. Henderson and A.J. Lewis (editors), Principles and Applications of Imaging Radar, Manual of Remote Sensing, John Wiley and Sons Inc., 3rd Edition, Vol. 2, pp. 131-181.

LIVINGSTONE, C.E., A.L. Gray, R.K. Hawkins, J.E. Halbertsma, R.A. Dean, and R.B. Olsen, 1987. CCRS C-Band Airborne Radar: Systems Description and Test Results. *In* Proceedings, 11th Canadian Symposium on Remote Sensing, pp. 503-518.

LIVINGSTONE, C.E., A.L. Gray, R.K. Hawkins, P. Vachon, T.I. Lukowski, and M. Lalonde, 1995. The CCRS Airborne SAR Systems: Radar for Remote Sensing Research. Canadian Journal of Remote Sensing, Vol. 21, No. 4, pp. 468-491.

LONG, D.G.F. and P. Copper, 1987. Stratigraphy of the Upper Ordovician upper Vaureal and Ellis Bay formations, eastern Anticosti Island, Quebec. Canadian Journal of Earth Sciences, Vol. 24, pp. 1807-1820.

LONG, D.G.F. and P. Copper, 1994. The Late Ordovician - Early Silurian Carbonate Tract of Anticosti Island, Gulf of St. Lawrence, Eastern Canada. Field Trip Guidebook B4. Geological Association of Canada/Mineralogical Association of Canada, Joint Annual Meeting, Waterloo, Ontario, 1994, 70 p.

LOPES, A., E. Nerzy, R. Touzi, and H. Laur, 1993. Structure detection and statistical adaptive speckle filtering in SAR images. International Journal of Remote Sensing, Vol. 14, No. 9, pp. 1735-1758.

MACKAY, D., 1979. Anticosti: the untamed island. McGraw-Hill Ryerson Limited, Toronto, Ontario, 160 p.

MCCRAKEN, A.D. and C.R. Barnes, 1981. Conodont biostratigraphy across the Ordovician – Silurian boundary, Ellis Bay Formation, Anticosti Island. *In* P.J. Lespérance (editor) I.U.G.S. Field meeting, Anticosti-Gaspé, Québec, 1981. Volume II Stratigraphy and paleontology. Département de géologie, Université de Montréal, pp. 61-69.

Ministère des Terres et Forêts, Québec, 1975. Photographies aériennes au 1:40 000.

Ministère des Terres et Forêts, Direction de la Côte-Nord, Québec, 1992. Carte au 1:250 000 délimitant les principales zones forestières de l'île d'Anticosti.

MORAIN, S.A., 1976. Use Radar for Vegetation Analysis, in Geoscience Applications of Imaging Radar Systems. *In* A.J. Lewis (editor), Remote Sensing of the Electromagnetic Spectrum, Association of American Geographers, Vol. 3, No. 3, pp. 61-78.

NADEAU, L., J.-M.M. Dubois, G. Lessard, and D. Côté, 1985. Géomorphologie d'une plate-forme littorale rocheuse de régions froides (île d'Anticosti, Golfe du Saint-Laurent, Canada). Photo-Interpretation (85-2), pp. 1-14.

NOWLAN, G.S. and C.R. Barnes, 1987. Thermal Maturation of Paleozoic Strata in Eastern Canada from Conodont Colour Alteration Index (CAI) Data with Implications for Burial History, Tectonic Evolution, Hotspot Tracks and Mineral and Hydrocarbon Exploration. Geological Survey of Canada, Bulletin 367, 47 p.

ORTH, C.J., J.S. Gilmore, and L.R. Quintana, 1986. Terminal Ordovician Extinction: Geochemical Analysis of the Ordovician/Silurian Boundary, Anticosti Island, Québec. Geology, Vol. 14, pp. 433-436.

PAINCHAUD, A., J.M.M. Dubois, and Q.H.J. Gwyn, 1984. Déglaciation et emersion des terres de l'ouest de l'île d'Anticosti, Golfe du Saint-Laurent, Québec. Géographie physique et Quaternaire, Vol. 38, No. 2, pp. 93-111.

PARÉ, G., 2000. Cartographie des géorisques karstiques à l'aide d'images radar: le cas de l'île d'Anticosti, Québec. Thèse M.Sc., Département de géographie et télédétection, Université de Sherbrooke, 105 p.

PCI Geomatics Group, 1998. Using PCI Software. *In* Reference Manual, Version 6.2, 530 p.

PERRAS, S., J.-M.M. Dubois, F. Bonn, and Q.H.J. Gwyn, 1985. Télédétection des dépôts meubles avec Landsat 4 TM, sur l'île d'Anticosti (Québec, Canada). Photo-Interpretation (85-3), pp. 11-18.

PETRYK, A.A., 1979. Stratigraphie révisée de l'île d'Anticosti. Ministère de l'énergie et des ressources. DPV 711, 24 p.

PETRYK, A.A., 1981a. Stratigraphy, sedimentology, and paleogeography of the Upper Ordovician-Lower Silurian of Anticosti Island, Québec. *In* P.J. Lespérance (editor) I.U.G.S. Field meeting, Anticosti-Gaspé, Québec, 1981. Volume II Stratigraphy and paleontology. Département de géologie, Université de Montréal, pp. 11-39.

PETRYK, A.A., 1981b. Carte géologique de l'île d'Anticosti (1:100 000). Ministère de l'Énergie et des Ressources, DVP-823, 14 p.

PETRYK, A.A., 1987. The Ordovician-Silurian boundary succession at Cap Henri, Anticosti Island, Québec. Geological Society of America Centennial Field Guide – Northeast Section, pp. 373-377.

RANEY, R.K., 1998. Radar Fundamentals: Technical Perspective. Chapter 2 *In* F.M. Henderson and A.J. Lewis (editors), Principles and Applications of Imaging Radar, Manual of Remote Sensing, John Wiley and Sons Inc., 3rd Edition, Vol. 2, pp. 9-130.

RHEAULT, M., I. Ouellet, and R. Saint-Jean, 1998. Evaluation of Polarimetric Airborne Radar for Lithologic Mapping, Lac Volant Cu-Ni-Co Showing, Canadian Shield. Presented at the Geological Association of Canada – Mineralogical Association of Canada (GAC-MAC) annual symposium, May 17-19, 1998, Québec, Québec.

RICHARDSON, J., 1857. Report for the year 1856 on the geology and topography of the island of Anticosti and Mingan Islands. Geological Survey of Canada, Report of Progress for 1853-54-55-56, pp. 191-245.

RIVA, J. and A.A. Petryk, 1981. Graptolites from the Upper Ordovician and Lower Silurian of Anticosti Island and the position of the Ordovician-Silurian boundary. *In* P.J. Lespérance (editor) I.U.G.S. Field meeting, Anticosti-Gaspé, Québec, 1981. Volume II Stratigraphy and paleontology. Département de géologie, Université de Montréal, pp. 159-164.

ROBERGE, J., 1996. Géomorphologie de l'île d'Anticosti et de la région de la Rivière Vauréal. État de connaissances. La Direction du Plein Air et des Parcs, Ministère de l'Environnement et de la Faune, Québec, 214 p.

ROLIFF, W.A., 1968. Oil and Gas Exploration - Anticosti Island, Québec. *In* Proceedings of the Geological Association of Canada, Vol. 19, pp. 31-36.

SABINS, F.F., 1997. Remote Sensing: Principles and Interpretation. Third Edition, W.H. Freeman and Company, New York, 494 p.

SAINT-JEAN, R., V. Singhroy, and M. Rheault, 1999. Multi-Polarized Airborne C-SAR Images for Geological Mapping at Lac Volant, Québec. Presented at the Thirteeth International Conference and Workshop – Applied Geologic Remote Sensing – ERIM, March 1-3, 1999, Vancouver, British Columbia.

SAMI, T. and A. Desrochers, 1992. Episodic sedimentation on an early Silurian, storm-dominated carbonate ramp, Becscie and Merrimack formations, Anticosti Island, Canada. Sedimentology, Vol. 39, pp. 355-381.

SANFORD, B.V. and A.C. Grant, 1990. Geology and Petroleum Potential of the Gulf of St. Lawrence Region. Bulletin of the American Association of Petroleum Geologists, Vol. 74, No. 8, p. 1310.

SANFORD, B.V., 1998. Geology and Oil and Gas Possibilities of the Gulf of St. Lawrence Region - Southeastern Canada. Open File Report – Geological Survey of Canada #3632, 63 p.

SCHABER, G.G., J.F. McCauley, and C.S. Breed, 1997. The Use of Multifrequency and Polarimetric SIR-C/X-SAR Data in Geologic Studies of Bir Safsaf, Egypt. Remote Sensing of Environment, Vol. 59, pp. 337-363.

SCHUCHERT, C. and W.H. Twenhofel, 1910. Ordovicic – Siluric section of the Mingan and Anticosti Islands, Gulf of St. Lawrence. Geological Society of America, Bulletin 21, pp. 677-716.

SÉGUIN, M.K. and A.A. Petryk, 1984. A Paleomagnetic Study of Upper Ordovician-Lower Silurian Strata of Anticosti Island, Québec. Northeastern Geology, Vol. 6, No. 1, pp. 25-37.

ST-PIERRE, L., Q.H.J. Gwyn, and J.M.M. Dubois, 1987. Lithostratigraphie et dynamique glaciaire au Wisconsinien, île d'Anticosti, golfe du Saint-Laurent. Canadian Journal of Earth Sciences, Vol. 24, pp. 1847-1858.

TANGUAY, M.G., F. Séa, S. Carboni, C. Seuthé, A.A. Petryk, 1988. Analyse de linéaments photogéologiques de l'île d'Anticosti, Québec. Institut de Recherche en Exploration Minérale, École Polytechnique de Montréal, Project 83-15, 62 p.

TOUTIN, Th. and B. Rivard, 1995. A New Tool for Depth Perception of Multi-Source Data. Photogrammetric Engineering & Remote Sensing, Vol. 61, No. 2, pp. 1209-1211.

TOUTIN, Th., 1997. Qualitative Aspects of Chromo-Stereoscopy for Depth Perception. Photogrammetric Engineering & Remote Sensing, Vol. 63, No. 2, pp. 193-203.

TOUZI, R. and F. Charbonneau, 2002. Polarimetric Workstation: User Guide. Canada Centre for Remote Sensing – Natural Resources Canada, Internal Publication, 16 p.

TWENHOFEL, W.H., 1914. The Anticosti Island Faunas. Geological Survey of Canada, Museum Bulletin No. 31, Geological Series, No. 19, 35 p.

TWENHOFEL, W.H., 1919. Revision of the Anticosti section. Geological society of America, Bulletin 31, 209 p.

TWENHOFEL, W.H., 1928. Geology of Anticosti Island. Geological Survey of Canada, Memoir No. 154, 481 p.

ULABY, F.T. and C. Elachi, 1990. Radar Polarimetry for Geoscience Applications, Artech House Inc., Norwood, MA, 364 p.

WANLESS, R.K. and R.D. Stevens, 1971. Note on the age of diabase dyke, Anticosti Island, Québec. Geological Association of Canada, Proceedings 23, pp. 77-78.

WILLIAMS, E.P., 1973. St. Lawrence Lowlands, Gaspé, and Gulf of St. Lawrence Areas. *In* R.G. McCrossan (editor), The Future Petroleum Provinces of Canada; Their Geology and Potential, Canadian Society of Petroleum Geology, Memoir 1, pp. 561-587.

WU, S.-T. and S.A., Sader, 1986. Multipolarization SAR Data for Surface Feature Delineation and Forest Vegetation Characterization. IEEE Transactions on Geoscience and Remote Sensing, Vol. GE-25, No. 1, pp. 67-76.

ZEBKER, H.A. and J.J. Van Zyl, 1991. Imaging Radar Polarimetry: A Review. *In* Proceedings of the IEEE, Vol. 79, No. 11, pp. 1583-1606.

APPENDICES

Appendix A: Details on the radiometric and geometric corrections

The image quality of the 1991 SAR data was exceptional. No radar antenna pattern in the cross-track direction of the image and no inherited radiometric artefacts due to the radar system itself were found suggesting a good reliability of the Convair-580 SAR facility during data acquisition. Only a 3x3 low-pass spatial filter developed especially for radar data, the Gamma map filter (Lopes *et al.*, 1993), was applied on the data to attenuate the weak presence of high-frequency noise (speckle). A linear contrast enhancement was also performed on the intensity image as part of its radiometric correction in order to expand the original grey-scale values of the data to a greater dynamic range and therefore facilitate the image interpretation.

In order to locate and trace the formation contacts and map the various structural elements present on Anticosti Island with respect to their actual ground location, the intensity image had to be projected onto a regular, two-dimensional cartesian grid. This is part of the geometric correction, called an *image-to-map* rectification (Jensen, 1996), which involves the planimetric transformation of the image geometry. Because of the side looking viewing configuration of the Convair-580 SAR system, radar data are acquired in a slant-range geometry, but transformed almost in real-time during acquisition to a ground-range geometry (Livingstone *et al.*, 1995). It is these ground-range data that were provided for this study and

geometrically rectified. The geometric correction was performed using a simple polynomial rectification assuming the wide-swath SAR data had a minimum of terrain distortions due to the shallow incidence angle used during its acquisition.

National Topographic System (NTS) map sheets at a scale of 1:50 000 were the principal source of planimetric information to geometrically rectify the intensity image. Ground control points (GCPs), which are points on the surface of the Earth where both image coordinates (measured in row/lines and columns/pixel) and map coordinates (measured in meters in Northing and Easting) can be identified, were collected most entirely from those NTS maps. GPS (Global Positioning System) readings, collected with a hand-held Magellan-320 receiver during the 1999 field campaign on Anticosti Island, were also used to rectify the 1991 SAR data. River junctions, road intersections, bridges, buildings and other man made structures such as fire towers and radio antennas were the prime targets to collect the GPS readings since they could be recognised on the intensity image. The positional accuracy of the GPS readings was estimated to range from 25 to 50 m, similar to what the 1:50 000 NTS maps are providing.

As illustrated in Figure A-1, a total of 84 GCPs with the best spatial distribution possible were selected from the NTS maps and the GPS readings. A mathematical relationship between the image coordinates and the map coordinates was therefore computed from these 84 GCPs to make the SAR image fit the geometry of the NTS maps (Table A-1). To define the best mathematical relationship between the image and the map projection, a fifth order

Figure A-1: Spatial distribution of the collected GCPs used for the geometric correction of the wide-swath SAR image. GCPs in blue are those with the worst residual with almost 9 pixel of RMSE.

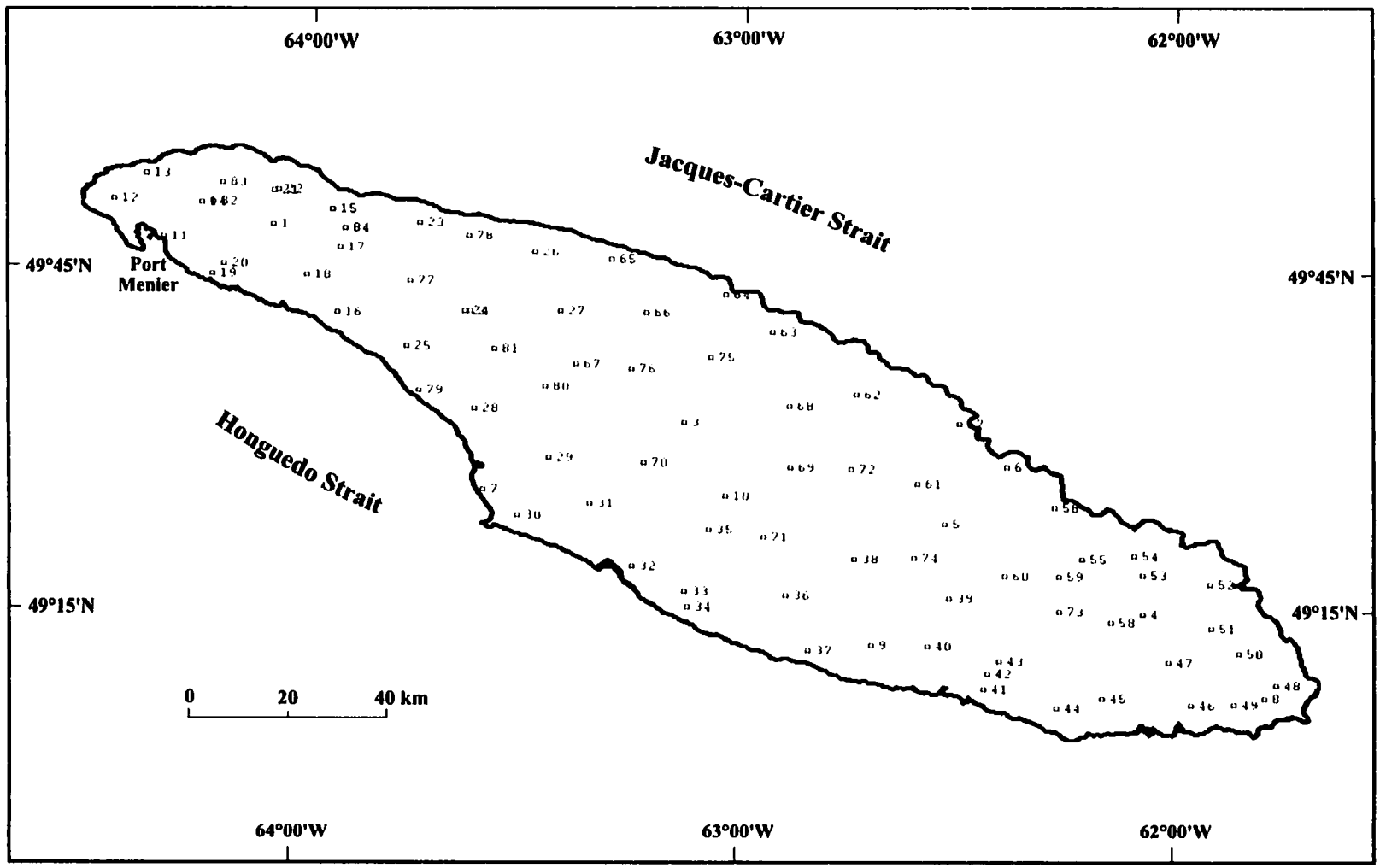
64°00'W
63°00'W
62°00'W
49°45'N
49°15'N
Jacques-Cartier Strait
Honguedo Strait
Port
Menier
0
20
40 km

Table A-1: Fifth order polynomial function used to geometrically rectify the wide-swath SAR image.

	Model Parameters		FX	FY
1	CONS		-7.307331253784135e+005	+1.456093284805043e+006
2	X		-2.411848561432695e+000	-9.164712867190437e+000
3		Y	+5.189017052098683e-001	+3.731951936575623e-001
4	X	* Y	+2.053482171060273e-006	+3.442041250899946e-006
5	X**2		-4.212426617701196e-005	-3.973306932252996e-005
6		Y**2	+5.565087256145376e-008	-8.959962156603399e-008
7	X**2	* Y	+1.122729017446463e-011	+1.033926983641313e-011
8	X	* Y**2	+0.000000000000000e+000	+0.000000000000000e+000
9	X**3		+6.185451788644126e-011	+7.880479109813343e-011
10		Y**3	-1.040606620185937e-013	-8.056411918021533e-014
11	X**2	* Y**2	-3.957597105532247e-020	-3.672568692616380e-019
12	X**3	* Y	-2.079088464005238e-017	-2.354022752284952e-017
13	X	* Y**3	-1.426916245547747e-019	-9.485920562299863e-020
14	X**4		-6.749049682331389e-018	-1.717817650218879e-017
15		Y**4	+2.350803152783989e-020	+2.093421914847276e-020
16	X**3	* Y**2	+1.752600017330563e-024	+1.673792296223547e-024
17	X**2	* Y**3	-1.118357436360738e-025	-3.506649130566531e-026
18	X**4	* Y	+1.101960259277531e-024	+3.065358471266070e-024
19	X	* Y**4	+1.629060699643355e-026	+6.548677477159740e-027
20	X**5		+3.440805768045090e-025	+2.714770915862736e-025
21		Y**5	-1.592397494870521e-027	-1.303918125769238e-027

polynomial function was chosen after evaluating the root-mean-square error (RMSE) of the GCPs. The selection of such high order polynomial function was possible because of the important number of collected GCPs, but also because of their ideal spatial distribution throughout the entire wide-swath SAR data. The obtained RMSE for that specific polynomial function was 29.9 m (or 2.0 pixel) in Easting and 37.8 m (or 2.5 lines) in Northing. These errors are also presented in Figure A-2 under a residual plot and in Table A-2 as the result of the individual positional error for each coordinate of the collected GCPs.

The geometric correction of the intensity image was performed by resampling the 15 m ground resolution data to a 25 m pixel spacing image file using the *Nearest-Neighbour* interpolation method of GCPWorks (PCI 6.2, 1998). It allowed the original grey-scale value of each pixel to be preserved during the projection even though the spatial resolution was transformed. The 25 m of pixel spacing of the projected image correspond to the positional accuracy of most geosciences data sets available in this study and its cartographic projection to a UTM (Universal Transverse Mercator) co-ordinate system with a 1983 North American Datum (NAD83) as listed in Table A-3.

Figure A-2: Residual plot of the collected GCPs.

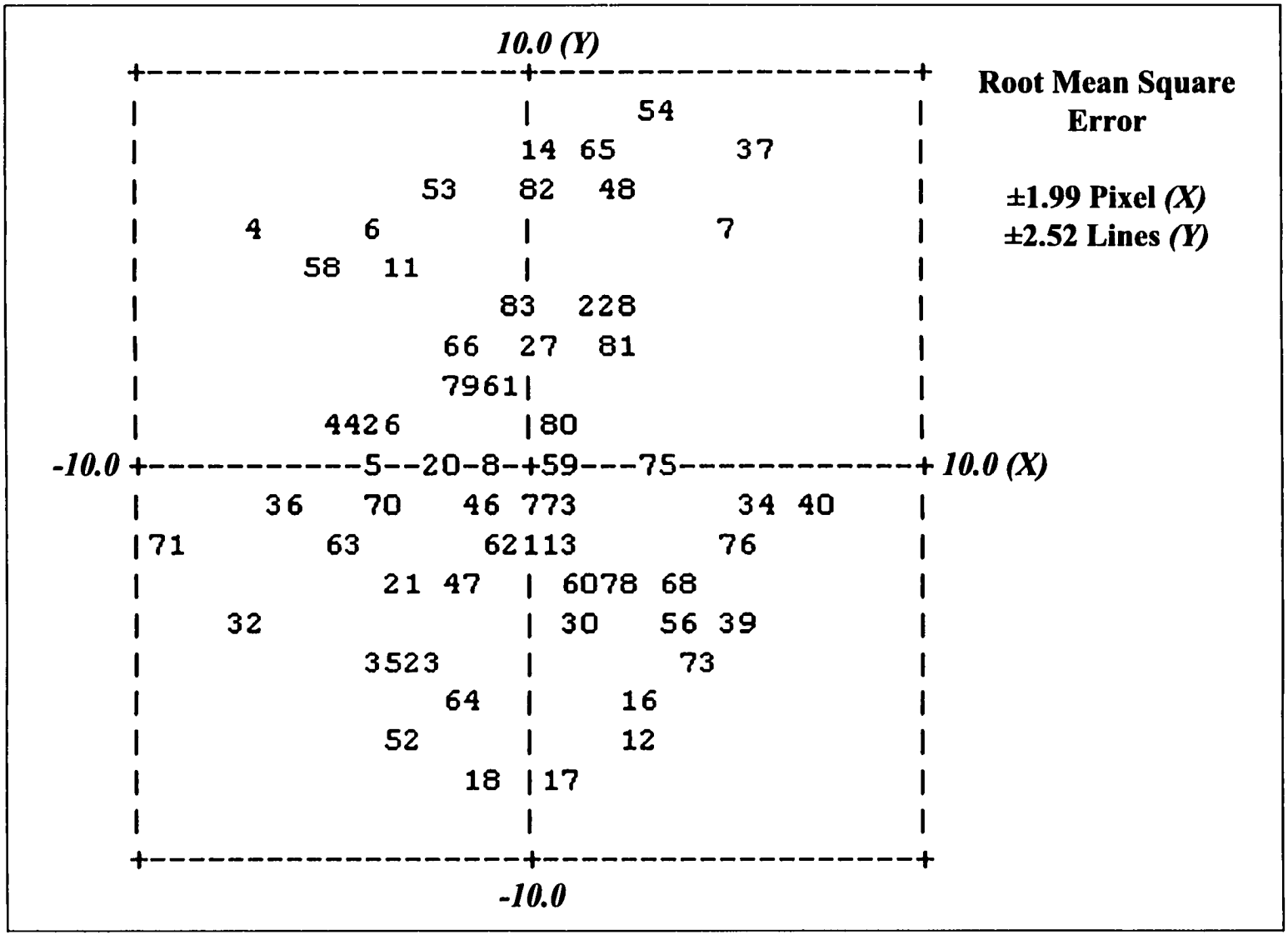
10.0 (Y)
-10.0
10.0 (X)
-10.0
Root Mean Square Error
±1.99 Pixel (X)
±2.52 Lines (Y)

Table A-2: List of GCPs ordered from worst to best residual.

GCP No.	Set 2 GCP's ----(UTM 20 U E008)---		Set 1 GCP's ------(PIXEL)----		Residual --- -------(PIXEL)--------		Distance --------
-84(	433217.2,	5521112.6)(	2988.6,	3023.2)(	-0.48,	-8.80)	8.81
-15(	430780.3,	5524648.5)(	3138.7,	2752.5)(	-0.71,	-8.45)	8.48
37(	515043.5,	5445836.9)(	537.9,	10810.6)(	3.14,	4.34)	5.36
4(	572800.2,	5454277.5)(	2460.5,	14346.5)(	-3.77,	3.34)	5.04
54(	571151.9,	5464678.3)(	3046.6,	13908.8)(	1.81,	4.69)	5.03
71(	506876.3,	5466181.1)(	1537.5,	9623.6)(	-4.82,	-0.82)	4.89
65(	479314.0,	5516749.2)(	3877.0,	6201.0)(	1.20,	4.35)	4.52
32(	484249.3,	5459907.2)(	606.3,	8331.3)(	-3.72,	-2.23)	4.34
14(	408238.8,	5525178.0)(	2612.0,	1277.0)(	0.29,	4.26)	4.27
18(	426775.6,	5512098.0)(	2292.0,	2890.9)(	-0.54,	-4.11)	4.14
40(	535775.6,	5447173.4)(	1130.7,	12129.5)(	4.10,	-0.49)	4.13
17(	432353.3,	5517459.6)(	2750.4,	3086.7)(	0.54,	-4.06)	4.10
51(	584632.8,	5452058.0)(	2625.4,	15189.2)(	0.71,	-4.04)	4.10
7(	458000.2,	5473680.3)(	783.5,	6172.1)(	2.62,	3.08)	4.04
52(	584401.8,	5459930.1)(	3088.0,	14924.8)(	-1.59,	-3.64)	3.97
58(	567291.4,	5452621.3)(	2226.7,	14035.8)(	-2.66,	2.89)	3.93
48(	596232.1,	5441828.3)(	2303.1,	16285.9)(	1.36,	3.63)	3.87
53(	572583.4,	5461330.4)(	2879.0,	14108.5)(	-1.09,	3.71)	3.87
12(	392970.2,	5525307.3)(	2243.8,	274.8)(	1.55,	-3.49)	3.82
73(	558380.5,	5454242.8)(	2108.2,	13391.8)(	2.52,	-2.86)	3.81
6(	548547.8,	5480542.4)(	3430.4,	11912.9)(	-2.27,	3.03)	3.78
16(	432191.7,	5505403.0)(	2030.0,	3459.0)(	1.55,	-3.36)	3.70
82(	410030.5,	5525290.7)(	2663.0,	1389.5)(	0.27,	3.69)	3.70
39(	539287.3,	5455848.9)(	1732.2,	12084.3)(	2.89,	-2.26)	3.67
36(	511024.2,	5455511.5)(	1007.0,	10235.5)(	-3.27,	-0.29)	3.29
11(	401645.8,	5518593.4)(	2056.5,	1053.3)(	-1.63,	2.83)	3.26
34(	494087.6,	5452981.3)(	444.7,	9200.1)(	3.19,	-0.41)	3.21
35(	497285.5,	5467285.0)(	1368.7,	8955.2)(	-1.99,	-2.52)	3.21
56(	557100.4,	5473361.8)(	3217.6,	12699.8)(	2.15,	-2.31)	3.15
64(	499166.7,	5510828.1)(	4015.6,	7687.9)(	-0.76,	-3.02)	3.12
76(	483295.5,	5496862.3)(	2789.2,	7093.1)(	2.84,	-1.27)	3.11
23(	445974.5,	5522512.1)(	3388.5,	3821.2)(	-1.33,	-2.80)	3.10
55(	562081.4,	5463757.4)(	2767.7,	13335.3)(	2.91,	-0.64)	2.98
68(	510791.6,	5490461.4)(	3089.4,	9106.5)(	2.09,	-1.82)	2.78
44(	558473.5,	5436342.1)(	1041.5,	13969.0)(	-2.48,	0.63)	2.56
28(	456265.2,	5488237.9)(	1604.1,	5592.6)(	1.38,	2.09)	2.51
49(	589000.2,	5438012.5)(	1898.0,	15925.0)(	1.77,	-1.75)	2.50
63(	507527.0,	5504395.7)(	3837.3,	8446.1)(	-2.28,	-0.94)	2.47
30(	464218.0,	5469013.3)(	657.7,	6724.2)(	0.73,	-2.32)	2.44
29(	469498.5,	5479623.8)(	1418.0,	6733.5)(	0.49,	-2.29)	2.34
2(	455195.9,	5506346.4)(	2655.0,	4945.4)(	0.68,	2.24)	2.34
83(	411674.0,	5528805.0)(	2912.6,	1385.4)(	0.06,	2.31)	2.31
21(	420657.1,	5527715.3)(	3069.2,	2001.1)(	-1.52,	-1.72)	2.30
72(	521765.0,	5479232.8)(	2689.0,	10191.5)(	-0.14,	2.26)	2.27
81(	459523.1,	5499754.4)(	2370.2,	5439.3)(	1.45,	1.61)	2.17
57(	540329.7,	5488183.1)(	3686.6,	11122.6)(	0.81,	-1.98)	2.13
70(	485792.7,	5479242.2)(	1795.9,	7820.1)(	-2.00,	-0.59)	2.08
5(	538163.2,	5469782.1)(	2529.7,	11569.7)(	-2.05,	0.01)	2.05
47(	577581.0,	5445589.3)(	2064.0,	14932.0)(	-0.82,	-1.87)	2.04
66(	485516.0,	5507132.1)(	3454.2,	6913.9)(	-0.85,	1.82)	2.01
26(	466077.1,	5517680.0)(	3599.6,	5297.6)(	-1.99,	0.30)	2.01
31(	476584.2,	5471530.1)(	1109.4,	7459.6)(	-1.97,	-0.22)	1.98
78(	454596.9,	5520368.7)(	3477.7,	4456.4)(	1.31,	-1.42)	1.94
75(	496930.8,	5499345.2)(	3275.5,	7912.4)(	1.89,	0.26)	1.90
69(	511210.2,	5479336.0)(	2434.7,	9492.7)(	1.21,	1.42)	1.87

Table A-2: Continued...

60(	548760.6,	5460405.5)(	2235.8,	12564.0)(	0.89,	-1.57)	1.81
10(	499960.9,	5473856.9)(	1826.4,	8924.5)(	-1.72,	-0.54)	1.80
27(	470684.9,	5506957.1)(	3075.8,	5944.1)(	0.30,	1.78)	1.80
24(	454270.9,	5506409.1)(	2634.7,	4882.0)(	-0.42,	1.62)	1.67
33(	493363.9,	5455669.2)(	582.4,	9069.2)(	-0.84,	1.41)	1.64
67(	473737.8,	5497264.4)(	2572.8,	6454.1)(	-0.12,	1.62)	1.62
25(	444324.6,	5499695.3)(	1988.8,	4441.8)(	-0.04,	1.47)	1.47
79(	446637.4,	5491428.1)(	1553.9,	4857.0)(	-0.68,	1.25)	1.42
45(	566142.2,	5438446.1)(	1357.0,	14407.9)(	-1.10,	0.85)	1.40
1(	420616.9,	5521467.4)(	2697.5,	2195.1)(	0.00,	-1.26)	1.26
20(	412292.8,	5513787.7)(	2034.2,	1895.2)(	-1.19,	0.24)	1.21
50(	589625.6,	5447709.5)(	2488.8,	15659.1)(	-0.05,	-1.18)	1.18
13(	398468.3,	5530095.7)(	2662.6,	484.2)(	0.47,	-1.06)	1.16
19(	410375.4,	5511673.4)(	1861.7,	1836.6)(	-1.08,	-0.21)	1.10
62(	522318.4,	5493030.3)(	3527.3,	9783.3)(	-0.30,	-1.03)	1.07
41(	545692.7,	5439472.3)(	914.5,	13026.0)(	0.27,	-0.97)	1.00
80(	468372.9,	5492893.1)(	2180.0,	6239.5)(	0.64,	0.72)	0.97
61(	533215.3,	5477132.3)(	2847.5,	11010.6)(	-0.39,	0.87)	0.95
74(	533039.9,	5463147.5)(	2009.4,	11444.5)(	0.11,	0.94)	0.95
3(	492723.9,	5486845.5)(	2423.2,	8034.0)(	0.45,	-0.74)	0.87
77(	444681.7,	5511470.3)(	2699.0,	4088.5)(	0.20,	-0.80)	0.82
59(	558178.0,	5460605.8)(	2480.6,	13178.9)(	0.62,	-0.20)	0.65
46(	581557.0,	5437721.9)(	1694.8,	15445.3)(	-0.50,	-0.32)	0.59
38(	522647.9,	5462595.9)(	1719.8,	10776.7)(	0.54,	-0.12)	0.55
8(	594193.6,	5439312.3)(	2101.2,	16227.9)(	-0.48,	0.21)	0.52
22(	421394.1,	5528015.7)(	3107.3,	2041.4)(	0.45,	-0.12)	0.47
43(	548173.3,	5444844.2)(	1294.1,	13020.7)(	-0.36,	0.15)	0.39
42(	546277.6,	5442541.9)(	1111.1,	12968.3)(	0.18,	-0.14)	0.23
9(	526068.9,	5447036.2)(	878.7,	11494.7)(	0.17,	-0.13)	0.22

Residual (in PIXEL)	**RMS=(**	**1.99,**	**2.52)** **3.21**

Table A-3: Description of the map projection used to geometrically rectify the wide-swath SAR image.

Georeference Units	:	UTM 20 U E008	
Projection	:	Universal Transverse Mercator	
Datum - Ellipsoid	:	NAD 83 - GRS 1980	
Upper Left Corner	:	385975.000 E	5537625.000 N
Upper Right Corner	:	602225.000 E	5537625.000 N
Image Centre	:	494100.000 E	5482650.000 N
Lower Left Corner	:	385975.000 E	5427675.000 N
Lower Right Corner	:	602225.000 E	5427675.000 N
Pixel Size	:	25.000 E	25.000 N
Upper Left Corner	:	64d35'25.49" W Lon	49d58'48.19" N Lat
Upper Right Corner	:	61d34'26.81" W Lon	49d58'55.89" N Lat
Image Centre	:	63d04'53.32" W Lon	49d29'47.24" N Lat
Lower Left Corner	:	64d33'31.33" W Lon	48d59'29.19" N Lat
Lower Right Corner	:	61d36'09.18" W Lon	48d59'36.63" N Lat

Appendix B: DEM Generation

The 18 digital maps provided separately for the entire island were merged together in order to get only one vector layer containing the contour lines (Figure B-1). Merging the maps together along with reconstructing the topology of the data was achieved using *ArcView3.2* in complementary with the *ArcInfo7.0* software. Once the merging was completed, edge matching between adjacent maps was evaluated as well as the consistency of the data. The vector layer representing the contour lines was imported in the *OrthoEngine* software of *PCI Geomatics* where the *VDEMINT* algorithm was used to interpolate the elevation at each DEM pixel from equal-distance points between the source elevation values (PCI 6.2, 1998). A finite differential method was also used during the process to interactively smooth the interpolated elevation values. The grid size (or pixel spacing) of the DEM was set to 25 m to meet the planimetric precision of the NTDB and to match the one of the geocoded SAR image.

Figure B-1: Representation of the contour lines derived from the 18 NTDB digital maps covering the whole Anticosti Island to generate the 1:50 000 DEM.

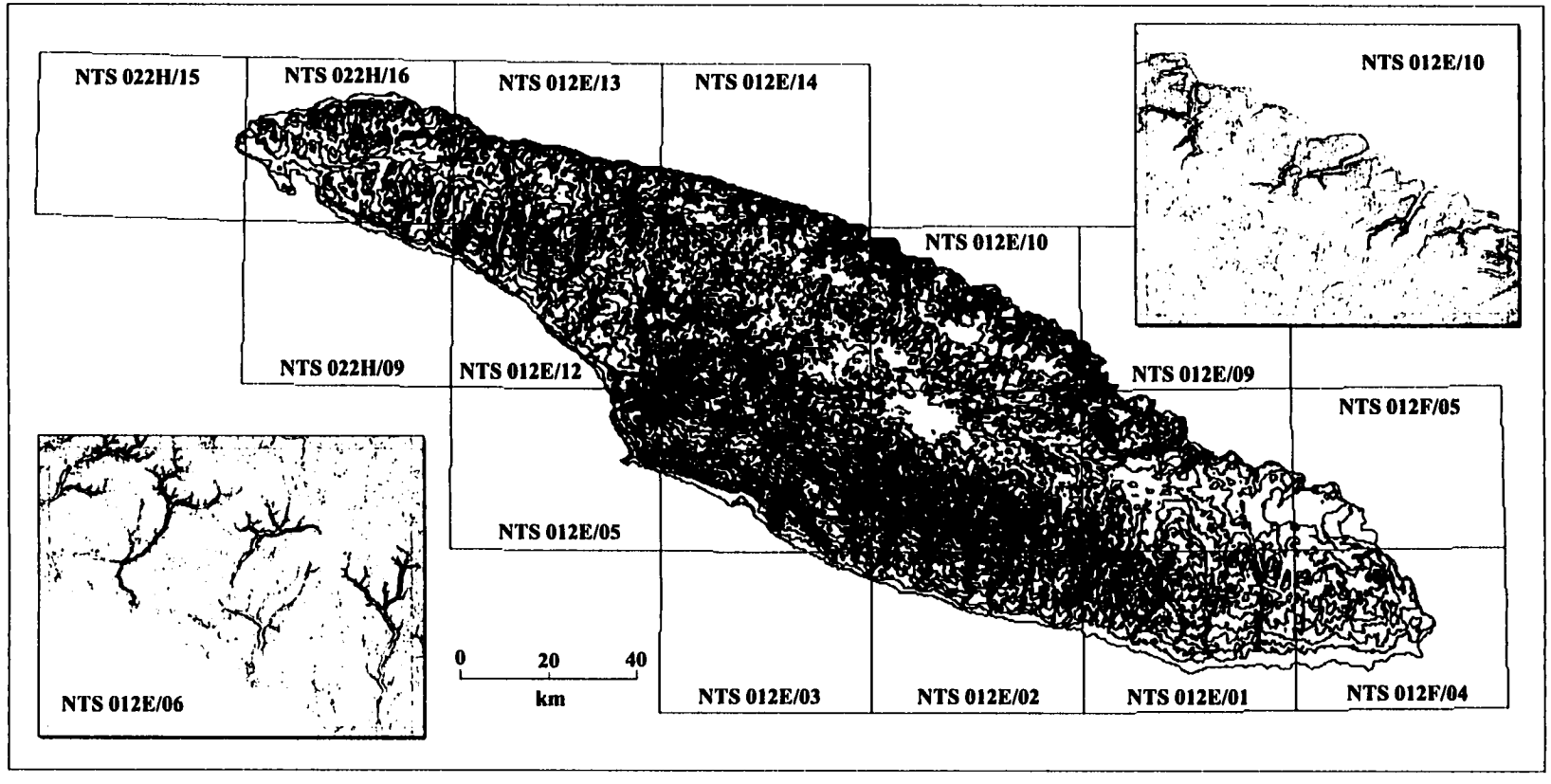
NTS 022H/15
NTS 022H/16
NTS 012E/13
NTS 012E/14
NTS 012E/10
NTS 012E/10
NTS 022H/09
NTS 012E/12
NTS 012E/09
NTS 012F/05
NTS 012E/05
NTS 012E/06
0
20
40
km
NTS 012E/03
NTS 012E/02
NTS 012E/01
NTS 012F/04

Appendix C: Statistics of every extracted polarimetric responses

The basic polarimetric parameters, including the linear and circular co- and cross-polarisation responses, the pedestal height, and the backscatter coefficient (σ°), were extracted with the *PW* software from 5 to 10 scattering samples taken within the 12 distinguished categories of vegetation, surface deposit, and bedrock geology. Table C-1 summarised the polarimetric statistics of every extracted scattering samples taken within the Vauréal Formation whereas Table C-2 gives these statistics for the Ellis Bay Formation.

Table C-1: Polarimetric statistics of every extracted scattering samples within the Vauréal Formation, independently of the surface deposits and forest stands. The typical 3D plots were generated from the polarimetric samples highlighted in grey.

Vauréal	Thin Organic Soil	White Spruce	s4-vl-pb-1	95	67.1	36 . 44855	80353	-11.44	-19.37	-12.54	-16.25
Vauréal	**Thin Organic Soil**	**White Spruce**	**s4-vl-pb-2**	**105**	**67.7**	**128 . 41615**	**70872**	**-11.52**	**-19.73**	**-12.84**	**-16.53**
Vauréal	Thin Organic Soil	White Spruce	s4-vl-pb-3	100	67.2	53 . 39095	24020	-11.30	-19.36	-12.56	-16.39
Vauréal	Thin Organic Soil	White Spruce	s4-vl-pb-4	105	67.3	69 . 32650	468452	-11.63	-19.94	-13.01	-16.82
Vauréal	Thin Organic Soil	White Spruce	s4-vl-pb-5	105	67.5	99 . 29395	121211	-11.69	-20.04	-13.08	-16.87
Vauréal	Thin Organic Soil	White Spruce	s4-vl-pb-6	112	68.6	287 . 33250	122909	-11.55	-19.97	-13.14	-16.73
Vauréal	Thin Organic Soil	White Spruce	s4-vl-pb-7	117	69.1	383 . 26575	139385	-11.82	-20.17	-13.32	-16.84
Vauréal	**Glacial Till**	**White Spruce**	**s4-vl-pb-8**	**112**	**68.4**	**247 . 12620**	**680484**	**-11.68**	**-20.16**	**-13.27**	**-16.78**
Vauréal	Thin Organic Soil	White Spruce	s4-vl-pb-9	82	62.7	1471 . 4055	150935	-10.83	-18.53	-11.20	-15.48
Vauréal	Glacial Till	White Spruce	s4-vl-pb-10	92	65.1	1780 . 40995	265352	-10.85	-18.61	-11.48	-15.52
Vauréal	Thin Organic Soil	White Spruce	s4-vl-pb-11	95	65.9	1894 . 32075	690559	-11.04	-19.15	-12.19	-16.04
Vauréal	Glacial Till	Black Spruce	s4-vl-pn-1	87	68.9	349 . 19665	133216	-11.70	-20.08	-13.41	-16.87
Vauréal	**Glacial Till**	**Black Spruce**	**s4-vl-pn-2**	**106**	**69.2**	**415 . 14155**	**46433**	**-11.92**	**-20.56**	**-13.79**	**-17.10**
Vauréal	Thin Organic Soil	Black Spruce	s4-vl-pn-3	81	61.9	1391 . 27865	34683	-9.95	-17.76	-10.46	-14.70
Vauréal	Littoral Sediments	Black Spruce	s4-vl-pn-4	49	53.3	691 . 16375	94195	-9.22	-17.10	-10.42	-13.56
Vauréal	Thick Organic Soil	Balsam Fir	s4-vl-sa-1	91	67.7	130 . 47135	92563	-11.57	-19.95	-12.97	-16.82
Vauréal	Thin Organic Soil	Balsam Fir	s4-vl-sa-2	110	68.6	291 . 40895	89231	-12.55	-21.05	-14.10	-17.88
Vauréal	Thin Organic Soil	Balsam Fir	s4-vl-sa-3	100	68.3	235 . 36155	279883	-12.24	-20.64	-13.72	-17.48
Vauréal	Thin Organic Soil	Balsam Fir	s4-vl-sa-4	113	68.8	326 . 27870	101954	-12.04	-20.73	-13.52	-17.50
Vauréal	Thin Organic Soil	Balsam Fir	s4-vl-sa-5	98	67.3	65 . 23035	178190	-11.58	-20.01	-13.03	-16.82
Vauréal	Glacial Till	Balsam Fir	s4-vl-sa-6	106	67.9	158 . 15280	74565	-11.63	-20.01	-13.16	-16.80
Vauréal	Glacial Till	Balsam Fir	s4-vl-sa-7	92	63.0	1507 . 2250	69442	-10.77	-18.14	-10.84	-15.07
Vauréal	Glacial Till	Balsam Fir	s4-vl-sa-8	90	63.8	1601 . 34455	251458	-11.01	-18.52	-11.19	-15.53
Vauréal	Thin Organic Soil	Balsam Fir	s4-vl-sa-9	77	61.7	1365 . 18240	74820	-10.51	-18.29	-10.89	-15.31
Vauréal	Glacial Till	White Spruce	s1-vl-pb-1	76	60.2	1208 . 13720	139439	-10.11	-17.93	-10.87	-14.78
Vauréal	Thin Organic Soil	White Spruce	s1-vl-pb-2	95	66.2	1935 . 5380	321102	-11.48	-19.74	-12.87	-16.46
Vauréal	Thin Organic Soil	White Spruce	s1-vl-pb-3	70	63.3	1548 . 2330	82781	-10.99	-18.38	-12.00	-15.30
Vauréal	Thin Organic Soil	White Spruce	s1-vl-pb-4	100	65.9	1883 . 10900	107505	-10.76	-18.94	-12.21	-15.63
Vauréal	Thin Organic Soil	White Spruce	s1-vl-pb-5	85	65.5	1830 . 43210	125524	-11.05	-19.07	-12.35	-15.75
Vauréal	Thin Organic Soil	White Spruce	s1-vl-pb-6	102	64.7	1714 . 39620	95204	-11.05	-19.03	-12.13	-15.70
Vauréal	Thin Organic Soil	White Spruce	s1-vl-pb-7	116	65.4	1820 . 28345	241663	-11.24	-19.12	-12.11	-16.01
Vauréal	Thin Organic Soil	White Spruce	s1-vl-pb-8	118	61.4	1336 . 31535	195636	-10.71	-18.12	-11.24	-15.08
Vauréal	Thin Organic Soil	White Spruce	s1-vl-pb-9	92	68.4	245 . 13535	45142	-11.85	-20.34	-13.60	-17.01
Vauréal	Thin Organic Soil	White Spruce	s1-vl-pb-10	80	67.9	167 . 9445	59236	-11.49	-19.90	-13.18	-16.46
Vauréal	Glacial Till	White Spruce	s1-vl-pb-12	106	70.4	667 . 26355	57522	-12.72	-21.40	-14.74	-17.80
Vauréal	Glacial Till	White Spruce	s1-vl-pb-13	103	70.4	666 . 29555	87302	-12.24	-20.79	-14.18	-17.21
Vauréal	**Thin Organic Soil**	**Black Spruce**	**s1-vl-pn-1**	**90**	**61.9**	**1385 . 11795**	**124929**	**-10.61**	**-18.60**	**-11.39**	**-15.45**
Vauréal	Thin Organic Soil	Black Spruce	s1-vl-pn-2	79	61.1	1297 . 16355	16408	-10.53	-18.09	-11.17	-14.91
Vauréal	Thick Organic Soil	Black Spruce	s1-vl-pn-3	61	65.5	1824 . 2845	11959	-11.31	-19.24	-12.65	-15.97
Vauréal	Thin Organic Soil	Black Spruce	s1-vl-pn-4	91	61.2	1314 . 8085	24556	-10.30	-18.31	-11.20	-15.27
Vauréal	Thin Organic Soil	Black Spruce	s1-vl-pn-5	121	66.5	1971 . 27580	29837	-11.18	-19.08	-12.73	-15.94
Vauréal	Thin Organic Soil	Black Spruce	s1-vl-pn-6	107	64.5	1692 . 36195	35341	-11.01	-18.95	-11.94	-15.91
Vauréal	Thick Organic Soil	Black Spruce	s1-vl-pn-8	91	69.5	474 . 33925	18184	-11.87	-20.03	-13.76	-16.60
Vauréal	Thin Organic Soil	Balsam Fir	s1-vl-sa-1	106	64.0	1629 . 60518	7925	-11.59	-19.33	-12.13	-16.13
Vauréal	Thin Organic Soil	Balsam Fir	s1-vl-sa-2	104	63.4	1560 . 7780	176073	-11.03	-18.69	-11.52	-15.58
Vauréal	Thin Organic Soil	Balsam Fir	s1-vl-sa-3	72	60.7	1258 . 3285	195563	-10.68	-18.62	-11.32	-15.57
Vauréal	Thin Organic Soil	Balsam Fir	s1-vl-sa-4	90	62.9	1495 . 42560	97569	-10.94	-18.65	-11.65	-15.65
Vauréal	**Thin Organic Soil**	**Balsam Fir**	**s1-vl-sa-5**	**101**	**65.8**	**1877 . 40895**	**62438**	**-11.67**	**-19.86**	**-12.94**	**-16.68**
Vauréal	Thin Organic Soil	Balsam Fir	s1-vl-sa-6	104	61.7	1361 . 37610	156333	-10.91	-18.53	-11.25	-15.52
Vauréal	Thin Organic Soil	Balsam Fir	s1-vl-sa-7	86	59.5	1146 . 41310	27778	-10.52	-18.33	-11.30	-15.27
Vauréal	Thin Organic Soil	Balsam Fir	s1-vl-sa-8	119	66.5	1977 . 29840	51691	-11.99	-20.27	-13.26	-18.99
Vauréal	Thick Organic Soil	Balsam Fir	s1-vl-sa-9	79	58.0	1017 . 38270	25570	-9.99	-17.63	-11.10	-14.63
Vauréal	Thin Organic Soil	Balsam Fir	s1-vl-sa-11	76	69.3	426 . 39805	327874	-12.49	-21.06	-14.45	-17.51
Vauréal	**Glacial Till**	**Balsam Fir**	**s1-vl-sa-12**	**108**	**69.0**	**377 . 29780**	**46367**	**-12.31**	**-20.64**	**-14.03**	**-17.34**
Vauréal	Glacial Till	Balsam Fir	s1-vl-sa-13	107	68.2	224 . 34485	64218	-12.85	-21.34	-14.60	-18.08

.44855	80353	-11.44	-19.37	-12.54	-16.25	-12.87	-16.29	1	0	73	-41	0.32	50	-43	98	0	0.22
,41615	**70872**	**-11.52**	**-19.73**	**-12.84**	**-16.53**	**-13.04**	**-16.52**	**179**	**0**	**65**	**-40**	**0.30**	**44**	**-41**	**7**	**1**	**0.21**
.39095	24020	-11.30	-19.36	-12.56	-16.39	-12.76	-16.22	4	0	73	-41	0.30	45	-43	115	-2	0.21
.32650	468452	-11.63	-19.94	-13.01	-16.82	-13.14	-16.74	0	0	71	-41	0.29	134	42	97	-1	0.21
.29395	121211	-11.69	-20.04	-13.08	-16.87	-13.20	-16.83	0	0	71	-41	0.29	134	42	2	0	0.21
.33250	122909	-11.55	-19.97	-13.14	-16.73	-13.19	-16.66	179	0	69	-40	0.28	45	-42	0	0	0.21
.26575	139385	-11.82	-20.17	-13.32	-16.84	-13.47	-16.78	0	0	65	-39	0.29	45	-40	1	0	0.21
,12620	**680484**	**-11.68**	**-20.16**	**-13.27**	**-16.78**	**-13.37**	**-16.72**	**0**	**0**	**66**	**-39**	**0.28**	**45**	**-40**	**1**	**0**	**0.21**
1.4055	150935	-10.83	-18.53	-11.20	-15.48	-11.88	-15.45	179	0	66	-43	0.34	138	44	9	0	0.22
0.40995	265352	-10.85	-18.61	-11.48	-15.52	-12.04	-15.56	176	0	113	43	0.33	137	43	170	-1	0.22
4.32075	690559	-11.04	-19.15	-12.19	-16.04	-12.45	-16.05	1	0	74	-41	0.31	47	43	6	0	0.21
.19665	133216	-11.70	-20.08	-13.41	-16.87	-13.41	-16.79	1	0	70	-39	0.28	46	-41	97	-1	0.21
,14155	**46433**	**-11.92**	**-20.56**	**-13.79**	**-17.10**	**-13.73**	**-17.13**	**177**	**-1**	**63**	**-37**	**0.26**	**45**	**-39**	**85**	**1**	**0.20**
1.27865	34683	-9.95	-17.76	-10.46	-14.70	-11.06	-14.66	177	0	81	-44	0.33	0	-45	5	0	0.21
.16375	94195	-9.22	-17.10	-10.42	-13.56	-10.89	-13.72	177	-1	121	39	0.33	45	-39	1	0	0.23
.47135	92563	-11.57	-19.95	-12.97	-16.82	-13.08	-16.73	1	0	69	-40	0.28	45	-42	0	0	0.20
.40895	89231	-12.55	-21.05	-14.10	-17.88	-14.14	-17.73	179	0	67	-40	0.27	45	-41	1	0	0.20
.36155	279883	-12.24	-20.64	-13.72	-17.48	-13.81	-17.37	0	0	71	-40	0.28	46	-42	93	0	0.21
.27870	101954	-12.04	-20.73	-13.52	-17.50	-13.57	-17.38	178	0	66	-40	0.27	134	42	8	1	0.19
.23035	178190	-11.58	-20.01	-13.03	-16.82	-13.11	-16.82	0	0	70	-40	0.28	45	-42	8	1	0.20
.15280	74565	-11.63	-20.01	-13.16	-16.80	-13.21	-16.85	0	0	113	40	0.28	46	-41	106	-2	0.21
7.2250	69442	-10.77	-18.14	-10.84	-15.07	-11.74	-14.99	169	0	72	-44	0.37	0	-45	3	0	0.23
.34455	251458	-11.01	-18.52	-11.19	-15.53	-11.97	-15.50	177	0	83	-44	0.35	0	-45	22	0	0.22
5.18240	74820	-10.51	-18.29	-10.89	-15.31	-11.53	-15.27	167	0	76	-44	0.33	0	-45	137	0	0.21
3.13720	139439	-10.11	-17.93	-10.87	-14.78	-11.39	-14.80	175	-1	61	-41	0.33	47	-42	1	0	0.22
5.5380	321102	-11.48	-19.74	-12.87	-16.46	-13.07	-16.42	179	0	66	-40	0.30	46	-41	90	0	0.21
8.2330	82781	-10.99	-18.38	-12.00	-15.30	-12.51	-15.25	1	0	69	-41	0.36	137	42	12	1	0.26
.10900	107505	-10.76	-18.94	-12.21	-15.63	-12.40	-15.65	1	0	68	-39	0.30	47	-41	2	0	0.22
0.43210	125524	-11.05	-19.07	-12.35	-15.75	-12.64	-15.86	179	0	114	40	0.31	46	-41	0	0	0.22
.39620	95204	-11.05	-19.03	-12.13	-15.70	-12.54	-15.81	1	0	119	40	0.32	136	41	1	0	0.22
0.28345	241663	-11.24	-19.12	-12.11	-16.01	-12.57	-15.97	179	0	65	-41	0.32	48	-42	91	0	0.22
5.31535	195636	-10.71	-18.12	-11.24	-15.08	-11.93	-15.01	175	0	65	-43	0.36	47	-43	90	0	0.24
.13535	45142	-11.85	-20.34	-13.60	-17.01	-13.60	-16.92	179	0	64	-38	0.27	135	40	175	-1	0.21
7.9445	59236	-11.49	-19.90	-13.18	-16.46	-13.29	-16.36	0	0	63	-38	0.28	45	-39	5	1	0.21
.26355	57522	-12.72	-21.40	-14.74	-17.80	-14.70	-17.64	179	0	65	-37	0.27	45	-39	0	0	0.21
.29555	87302	-12.24	-20.79	-14.18	-17.21	-14.19	-17.15	0	0	64	-37	0.28	45	-38	90	0	0.21
,11795	**124929**	**-10.61**	**-18.60**	**-14.39**	**-15.45**	**-11.86**	**-15.46**	**176**	**-1**	**65**	**-41**	**0.32**	**48**	**-43**	**3**	**0**	**0.21**
.16355	16408	-10.53	-18.09	-11.17	-14.91	-11.78	-15.09	178	0	114	42	0.34	45	-43	21	2	0.23
4.2845	11959	-11.31	-19.24	-12.65	-15.97	-12.96	-15.92	179	0	64	-39	0.32	136	40	168	-2	0.23
4.8085	24556	-10.30	-18.31	-11.20	-15.27	-11.62	-15.04	175	-1	63	-41	0.30	47	-42	175	-1	0.21
.27580	29837	-11.18	-19.08	-12.73	-15.94	-12.86	-15.97	1	-1	72	-39	0.31	52	-41	22	2	0.23
.36195	35341	-11.01	-18.95	-11.94	-15.91	-12.35	-15.75	175	-1	63	-40	0.31	48	-42	75	2	0.22
.33925	18184	-11.87	-20.03	-13.76	-16.60	-13.81	-16.62	1	0	66	-37	0.29	47	-39	12	2	0.23
.60518	7925	-11.59	-19.33	-12.13	-16.13	-12.79	-16.15	1	0	124	42	0.34	46	-42	99	-1	0.22
0.7780	176073	-11.03	-18.69	-11.52	-15.58	-12.17	-15.64	174	-1	122	43	0.34	48	-43	91	0	0.22
8.3285	195563	-10.68	-18.62	-11.32	-15.57	-11.84	-15.53	173	-1	63	-42	0.32	47	-43	15	1	0.21
.42560	97569	-10.94	-18.65	-11.65	-15.65	-12.17	-15.58	171	0	63	-42	0.33	45	-43	21	1	0.22
.40895	**62438**	**-11.67**	**-19.86**	**-12.94**	**-16.68**	**-13.14**	**-16.75**	**179**	**0**	**115**	**40**	**0.29**	**137**	**41**	**28**	**3**	**0.21**
.37610	156333	-10.91	-18.53	-11.25	-15.52	-11.94	-15.50	171	0	61	-43	0.34	46	-44	25	1	0.22
.41310	27778	-10.52	-18.33	-11.30	-15.27	-11.79	-15.23	177	0	64	-42	0.33	47	-43	107	-1	0.22
.29840	51691	-11.99	-20.27	-13.26	-18.99	-12.16	-26.43	2	0	69	-41	0.29	134	42	10	1	0.21
.38270	25570	-9.99	-17.63	-11.10	-14.63	-11.47	-14.54	174	-1	65	-40	0.33	135	42	147	-3	0.23
.39805	327874	-12.49	-21.06	-14.45	-17.51	-14.40	-17.54	0	0	116	37	0.27	136	39	91	0	0.21
.29780	**46367**	**-12.31**	**-20.64**	**-14.03**	**-17.34**	**-14.05**	**-17.36**	**179**	**0**	**113**	**38**	**0.28**	**43**	**-40**	**11**	**2**	**0.21**
.34485	64218	-12.85	-21.34	-14.60	-18.08	-14.55	-18.11	179	0	66	-38	0.27	46	-40	13	2	0.20

Table C-2: Polarimetric statistics of every extracted scattering samples within the Ellis Bay Formation, independently of the surface deposits and forest stands. The typical 3D plots were generated from the polarimetric samples highlighted in grey.

Ellis Bay	Glacial Till	White Spruce	s4-eb-pb-1	82	58.0	1022 , 29275	103880	-9.82	-17.56	-10.50
Ellis Bay	**Glacial Till**	**White Spruce**	**s4-eb-pb-2**	**60**	**49.8**	**498 , 49295**	**29896**	**-8.35**	**-16.26**	**-9.05**
Ellis Bay	Littoral Sediments	White Spruce	s4-eb-pb-3	45	47.6	396 , 16720	63421	-8.17	-15.86	-9.15
Ellis Bay	Glacial Till	Black Spruce	s4-eb-pn-1	80	56.3	886 , 2565	62343	-9.76	-17.37	-10.52
Ellis Bay	Thick Organic Soil	Black Spruce	s4-eb-pn-2	60	44.3	264 , 3415	66674	-7.23	-15.31	-8.66
Ellis Bay	**Glacial Till**	**Black Spruce**	**s4-eb-pn-3**	**98**	**58.2**	**1036 , 26975**	**185366**	**-9.95**	**-17.57**	**-10.52**
Ellis Bay	Glacial Till	Black Spruce	s4-eb-pn-4	105	55.0	797 , 25375	51669	-9.15	-16.83	-10.15
Ellis Bay	Glacial Till	Black Spruce	s4-eb-pn-5	100	58.2	1037 , 20025	38759	-10.11	-17.95	-10.90
Ellis Bay	Thick Organic Soil	Black Spruce	s4-eb-pn-6	45	45.0	289 , 15290	48887	-7.65	-15.80	-9.04
Ellis Bay	Thick Organic Soil	Black Spruce	s4-eb-pn-7	85	52.2	623 , 21380	76738	-8.75	-16.42	-9.70
Ellis Bay	Glacial Till	Black Spruce	s4-eb-pn-8	78	55.5	830 , 39015	27872	-9.59	-17.43	-10.33
Ellis Bay	Glacial Till	Balsam Fir	s4-eb-sa-1	80	46.0	330 , 580	80899	-7.88	-15.93	-8.90
Ellis Bay	Thick Organic Soil	Balsam Fir	s4-eb-sa-2	58	37.2	44 , 1435	71024	-5.96	-14.18	-7.40
Ellis Bay	Thick Organic Soil	Balsam Fir	s4-eb-sa-3	89	55.6	840 , 44805	45668	-9.56	-17.57	-10.32
Ellis Bay	Thick Organic Soil	Balsam Fir	s4-eb-sa-4	76	58.4	1050 , 40500	43587	-9.78	-17.46	-10.57
Ellis Bay	Glacial Till	Balsam Fir	s4-eb-sa-5	95	60.4	1229 , 33175	38743	-10.00	-17.89	-10.41
Ellis Bay	Glacial Till	Balsam Fir	s4-eb-sa-6	85	56.6	914 , 32705	193104	-9.99	-17.93	-10.67
Ellis Bay	Thick Organic Soil	Balsam Fir	s4-eb-sa-7	106	56.7	921 , 24115	52412	-9.93	-17.85	-10.76
Ellis Bay	**Glacial Till**	**Balsam Fir**	**s4-eb-sa-8**	**75**	**53.3**	**691 , 18140**	**117123**	**-9.02**	**-17.02**	**-10.12**
Ellis Bay	Thick Organic Soil	Balsam Fir	s4-eb-sa-9	45	46.8	361 , 15005	44036	-8.59	-16.37	-9.60
Ellis Bay	Glacial Till	Balsam Fir	s4-eb-sa-10	105	60.7	1263 , 22625	33318	-10.56	-18.29	-10.67
Ellis Bay	Glacial Till	White Spruce	s1-eb-pb-1	91	54.8	783 , 9485	16386	-8.91	-16.85	-10.34
Ellis Bay	Glacial Till	White Spruce	s1-eb-pb-2	85	56.6	907 , 18635	32788	-9.38	-17.19	-10.34
Ellis Bay	Glacial Till	White Spruce	s1-eb-pb-3	104	58.0	1020 , 6120	36670	-10.09	-18.02	-11.31
Ellis Bay	Glacial Till	Black Spruce	s1-eb-pn-1	76	52.1	620 , 12675	23117	-8.64	-16.50	-9.91
Ellis Bay	Glacial Till	Black Spruce	s1-eb-pn-2	85	52.4	634 , 10140	12652	-8.56	-15.67	-9.86
Ellis Bay	**Thin Organic Soil**	**Black Spruce**	**s1-eb-pn-3**	**110**	**52.0**	**615 , 26205**	**13812**	**-8.48**	**-16.33**	**-9.67**
Ellis Bay	Glacial Till	Balsam Fir	s1-eb-sa-1	88	55.9	861 , 16345	91172	-9.55	-17.34	-10.45
Ellis Bay	Glacial Till	Balsam Fir	s1-eb-sa-2	73	49.9	500 , 14795	74487	-8.12	-15.82	-8.99
Ellis Bay	Glacial Till	Balsam Fir	s1-eb-sa-3	93	55.9	861 , 6025	106716	-10.08	-18.12	-11.03
Ellis Bay	Glacial Till	Balsam Fir	s1-eb-sa-4	80	52.2	624 , 4115	34877	-8.81	-16.88	-10.17
Ellis Bay	Thin Organic Soil	Balsam Fir	s1-eb-sa-5	89	49.5	483 , 40585	127290	-8.46	-16.39	-9.39
Ellis Bay	**Thin Organic Soil**	**Balsam Fir**	**s1-eb-sa-6**	**102**	**52.6**	**644 , 40715**	**32378**	**-9.15**	**-17.37**	**-10.45**
Ellis Bay	Thin Organic Soil	Balsam Fir	s1-eb-sa-7	103	52.9	666 , 32675	82772	-8.39	-16.19	-9.75
Ellis Bay	Thin Organic Soil	Balsam Fir	s1-eb-sa-8	100	50.6	539 , 29560	153171	-8.90	-16.67	-9.68
Ellis Bay	Thin Organic Soil	Balsam Fir	s1-eb-sa-9	109	56.0	863 , 27995	9169	-10.61	-18.19	-11.72

103880	-9.82	-17.56	-10.50	-14.59	-11.01	-14.54	179	0	80	-43	0.33	0	-45	26	0	0.22
29896	**-8.35**	**-16.26**	**-9.05**	**-12.53**	**-9.87**	**-12.51**	**0**	**0**	**51**	**-36**	**0.33**	**45**	**-36**	**87**	**1**	**0.21**
63421	-8.17	-15.86	-9.15	-11.83	-10.06	-12.03	173	-3	51	-33	0.34	45	-34	0	0	0.02
62343	-9.76	-17.37	-10.52	-14.22	-11.10	-14.21	0	0	58	-41	0.35	42	-42	105	-2	0.23
66674	-7.23	-15.31	-8.66	-10.48	-9.86	-10.55	178	-1	51	-28	0.31	44	-29	92	-2	0.22
185366	**-9.95**	**-17.57**	**-10.52**	**-14.51**	**-11.13**	**-14.52**	**176**	**0**	**101**	**43**	**0.35**	**43**	**-44**	**101**	**0**	**0.23**
51669	-9.15	-16.83	-10.15	-13.65	-10.58	-13.80	173	-1	111	42	0.33	136	42	100	-1	0.24
38759	-10.11	-17.95	-10.90	-14.90	-11.37	-14.87	170	0	65	-42	0.32	40	-44	88	0	0.22
48887	-7.65	-15.80	-9.04	-10.84	-10.29	-10.98	177	-1	127	29	0.30	44	-29	92	2	0.22
76738	-8.75	-16.42	-9.70	-12.98	-10.30	-13.06	179	0	123	39	0.34	135	39	5	1	0.24
27872	-9.59	-17.43	-10.33	-14.14	-10.94	-14.10	0	1	53	-41	0.34	40	-41	94	-1	0.22
80899	-7.88	-15.93	-8.90	-11.44	-9.96	-11.63	175	-2	128	32	0.32	134	32	91	-1	0.21
71024	-5.96	-14.18	-7.40	-7.93	-10.23	-7.93	0	0	50	-19	0.30	135	20	91	-1	0.22
45668	-9.56	-17.57	-10.32	-14.33	-10.83	-14.42	177	0	119	41	0.32	45	-42	82	1	0.21
43587	-9.78	-17.46	-10.57	-14.36	-11.07	-14.45	177	0	104	43	0.34	43	-43	109	-1	0.23
38743	-10.00	-17.89	-10.41	-14.91	-11.02	-14.80	175	0	74	-44	0.32	0	-45	11	0	0.20
193104	-9.99	-17.93	-10.67	-14.77	-11.20	-14.79	175	0	111	42	0.32	39	-43	5	1	0.21
52412	-9.93	-17.85	-10.76	-14.73	-11.21	-14.77	175	0	108	42	0.32	46	-43	100	-1	0.22
117123	**-9.02**	**-17.02**	**-10.12**	**-13.67**	**-10.54**	**-13.69**	**176**	**-1**	**58**	**-39**	**0.31**	**45**	**-40**	**85**	**1**	**0.22**
44036	-8.59	-16.37	-9.60	-11.97	-10.66	-12.32	172	-4	129	33	0.33	45	-32	13	6	0.23
33318	-10.56	-18.29	-10.67	-15.23	-11.44	-15.26	142	0	50	44	0.33	0	-45	17	0	0.20
16386	-8.91	-16.85	-10.34	-13.50	-10.67	-13.34	178	0	60	-37	0.31	45	-38	0	0	0.23
32788	-9.38	-17.19	-10.34	-14.12	-10.73	-14.18	179	0	115	41	0.32	48	-42	41	3	0.22
36670	-10.09	-18.02	-11.31	-14.80	-11.57	-15.04	176	-1	110	41	0.31	46	-42	111	-2	0.22
23117	-8.64	-16.50	-9.91	-13.00	-10.31	-13.26	177	-1	120	38	0.31	44	-38	23	5	0.23
12652	-8.56	-15.67	-9.86	-12.22	-10.52	-12.26	178	-1	58	-35	0.38	136	37	19	5	0.28
13812	**-8.48**	**-16.33**	**-9.67**	**-13.00**	**-10.05**	**-13.12**	**178**	**-1**	**122**	**39**	**0.32**	**48**	**-39**	**160**	**-4**	**0.23**
91172	-9.55	-17.34	-10.45	-14.21	-10.93	-14.13	179	0	58	-40	0.33	133	41	121	-4	0.22
74487	-8.12	-15.82	-8.99	-12.11	-9.76	-12.24	174	-2	52	-35	0.33	135	36	115	-7	0.23
106716	-10.08	-18.12	-11.03	-14.89	-11.45	-14.89	173	-1	55	-39	0.31	42	-40	159	-3	0.21
34877	-8.81	-16.88	-10.17	-13.31	-10.60	-13.21	179	0	57	-36	0.31	45	-37	86	1	0.22
127290	-8.46	-16.39	-9.39	-12.55	-10.15	-12.61	0	0	128	35	0.32	45	-35	102	-4	0.22
32378	**-9.15**	**-17.37**	**-10.45**	**-13.74**	**-10.82**	**-13.93**	**174**	**-1**	**120**	**37**	**0.29**	**43**	**-38**	**178**	**0**	**0.21**
82772	-8.39	-16.19	-9.75	-12.77	-10.15	-12.76	178	0	58	-37	0.32	45	-38	107	-4	0.24
153171	-8.90	-16.67	-9.68	-13.16	-10.37	-13.23	176	-1	52	-37	0.33	135	37	125	-7	0.22
9169	-10.61	-18.19	-11.72	-14.91	-12.13	-15.28	174	-1	115	40	0.32	42	-40	44	5	0.23

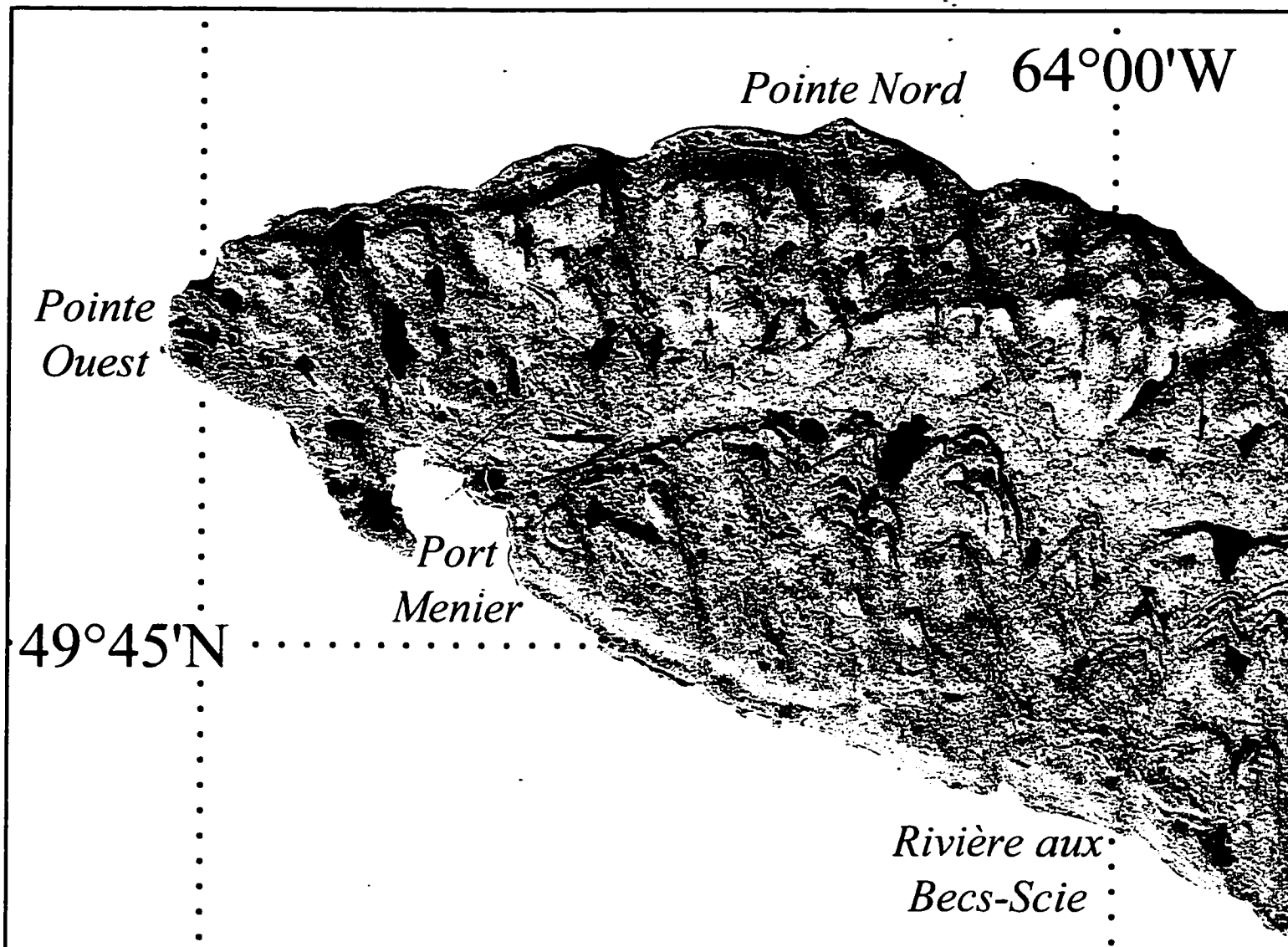

Convair-580 C-Band SAR
Wide-Swath

Shaded Re

Antic

Gulf of St.L

M

1 :

5 0 5

Universal Trans
(U

In

Rivière Vauréal

Rivière aux Saumons

Shaded Relief SAR Image

Anticosti Island

Gulf of St.Lawrence, Québec

MAP-IMAGE 1

1 : 250 000

5 0 5 10 15 20 25 30 km

Universal Transverse Mercator Map Projection
(UTM 20U NAD83)

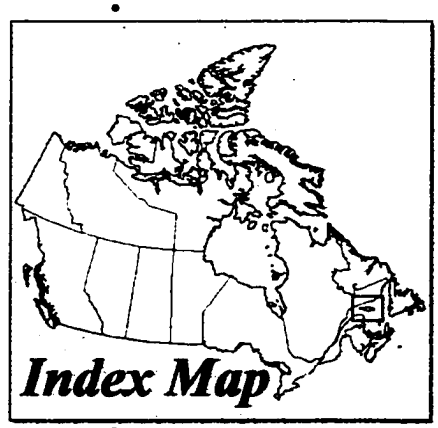

Rivière aux Saumons

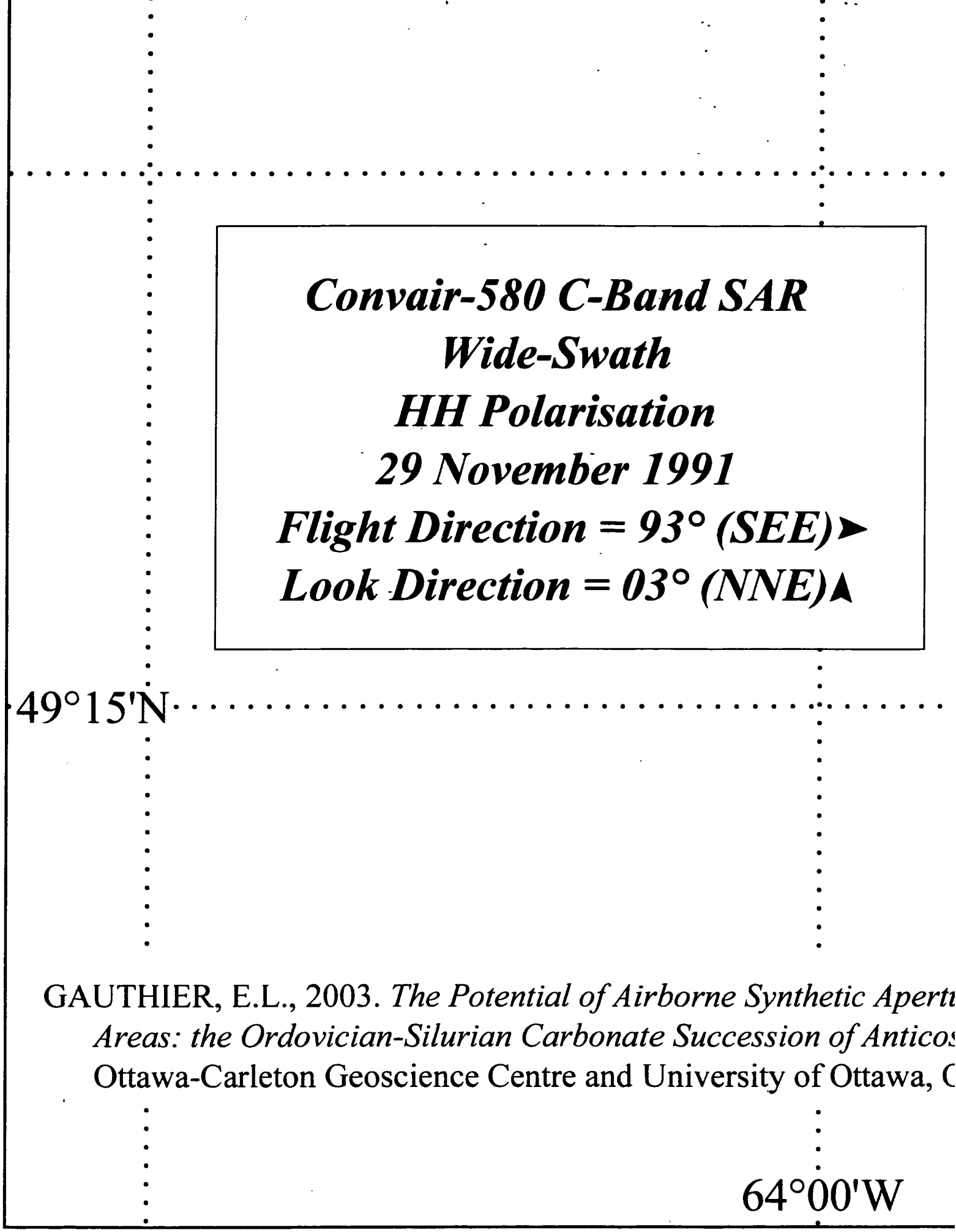

GAUTHIER, E.L., 2003. *The Potential of Airborne Synthetic Apertu*
Areas: the Ordovician-Silurian Carbonate Succession of Anticos
Ottawa-Carleton Geoscience Centre and University of Ottawa, C

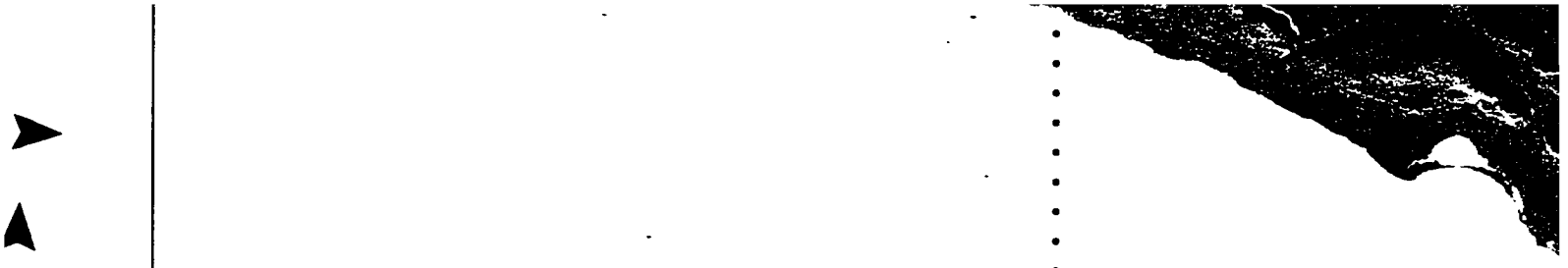

Honguedo Strait

tic Aperture Radar (SAR) Imagery as a Basic Tool for Stratigraphic Inve
of Anticosti Island, Gulf of St.Lawrence, Eastern Canada. M.Sc. Thesis i
Ottawa, Ottawa, Canada.

0'W

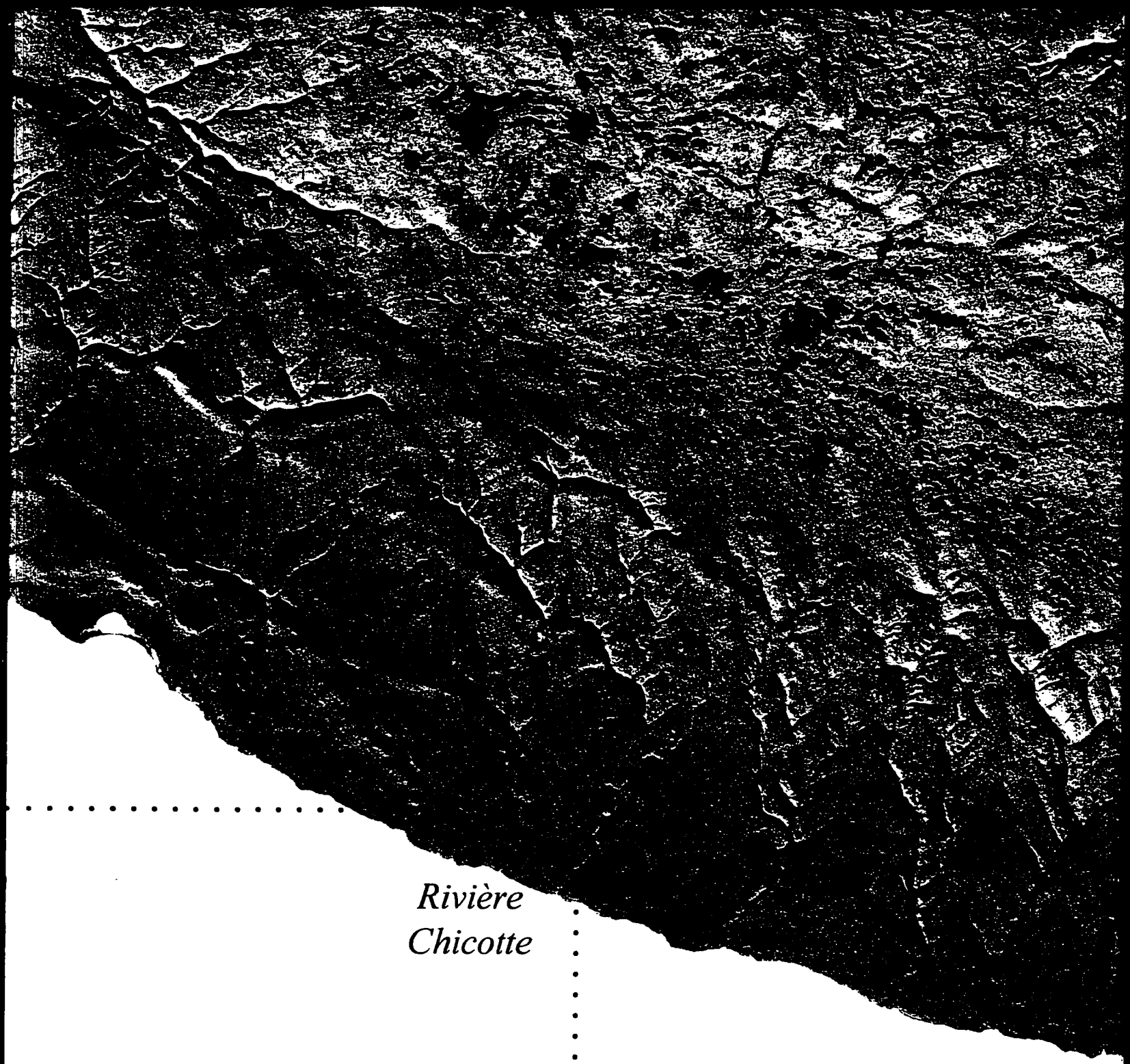

graphic Investigations in Forested
Sc. Thesis in Earth Sciences,

63°00'W

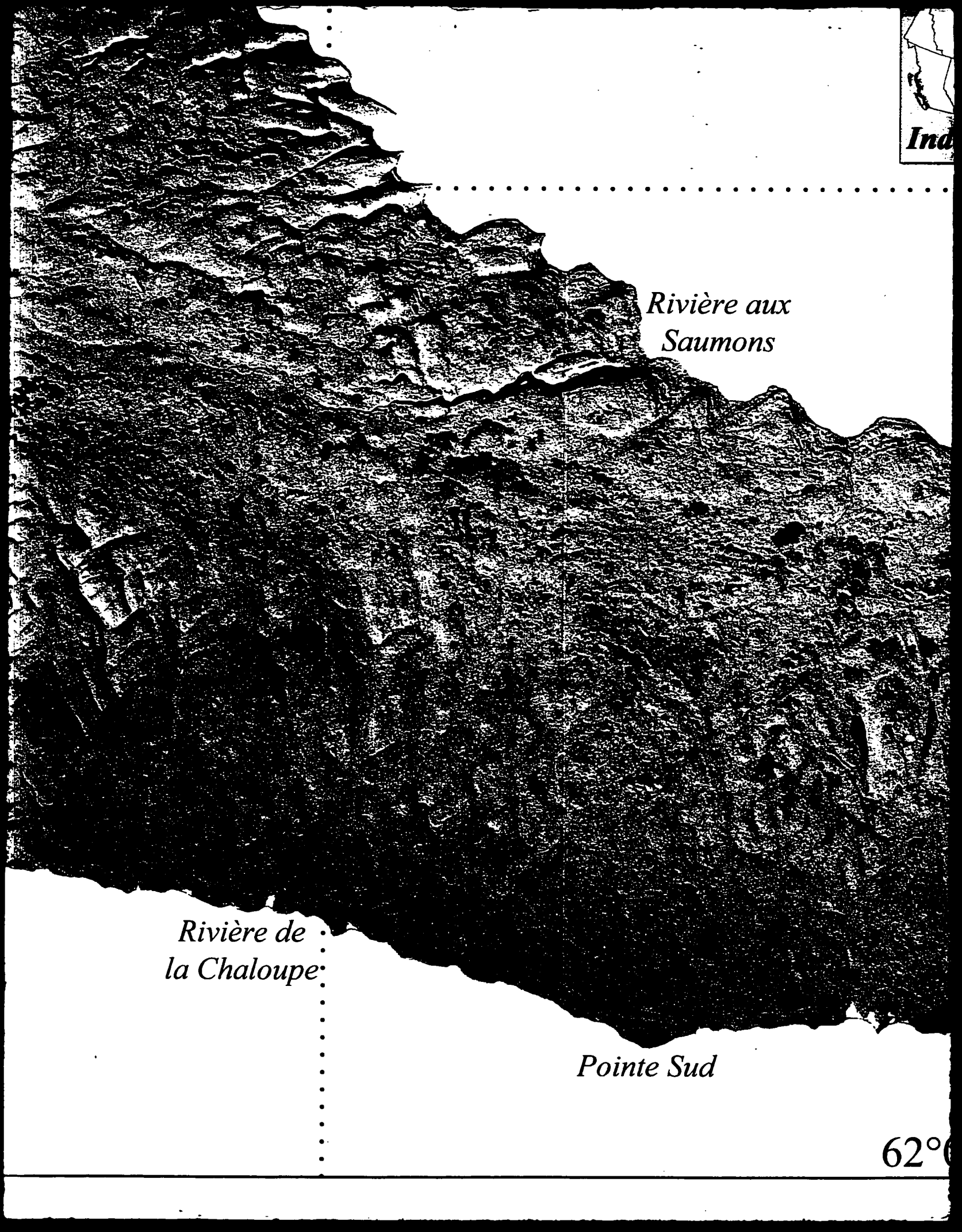
Rivière aux
Saumons
Rivière de
la Chaloupe
Pointe Sud
62°

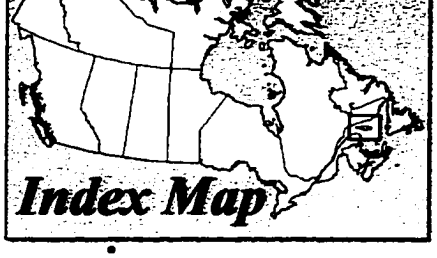

vière aux
aumons

Cap de
la Table

49°15'N

Pointe
Est

Pointe
Heath

lud

62°00'W

64°00'W

Pointe Nord

Pointe Ouest

Port Menier

49°45'N

Rivière aux Becs-Scie

Structural Lineaments

Mesozoic

LATE JURASSIC

(a) Diabase dykes

(b) *(a)* certain, *(b)* interpreted

Lower Paleozoic

EARLY SILURIAN

Chicotte Formation

Jupiter Formation

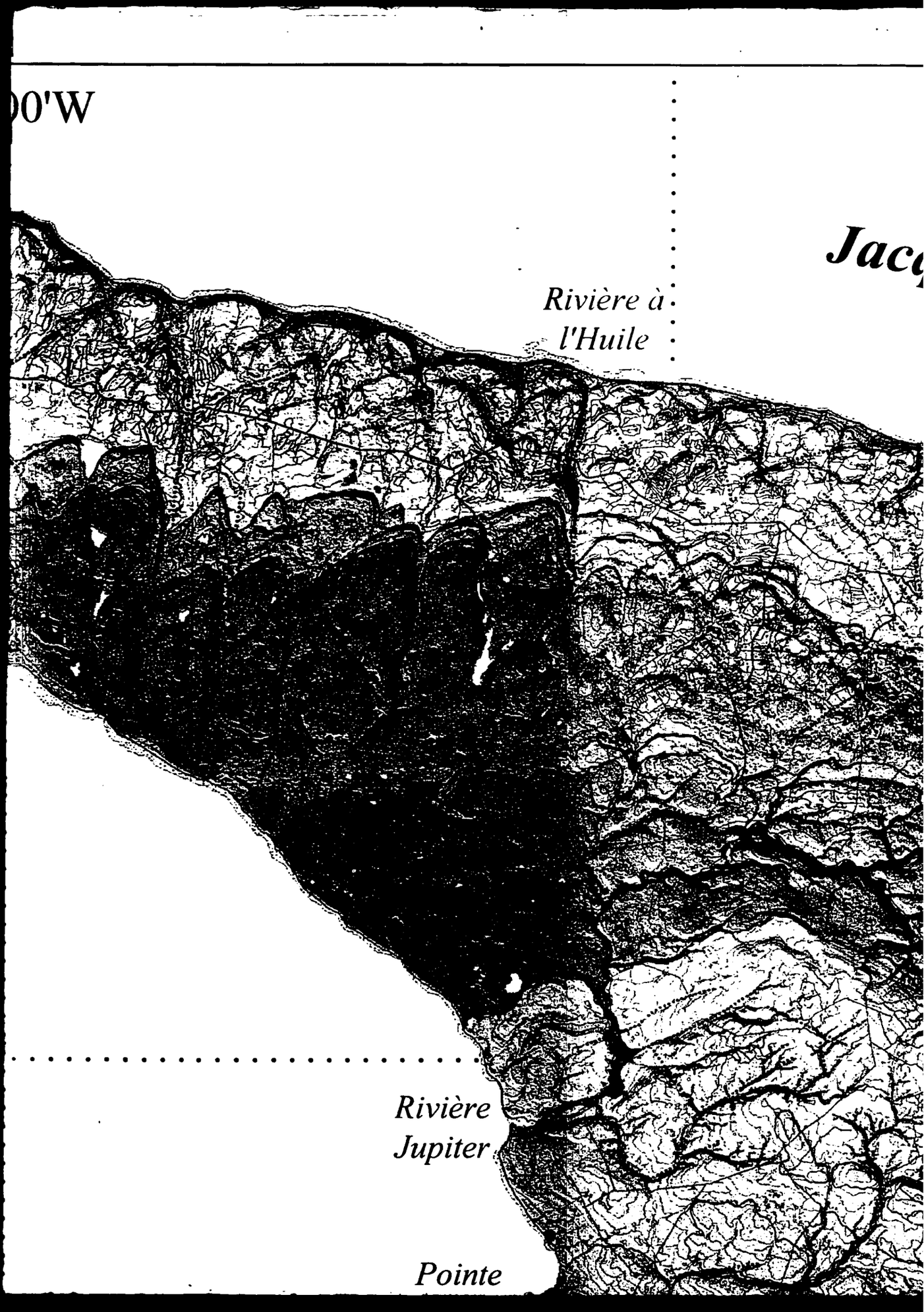
00'W
Jacq
Rivière à
l'Huile
Rivière
Jupiter
Pointe

Geology Map

Anticosti Island

Gulf of St. Lawrence, Québec

MAP-IMAGE 2

1 : 250 000

5 0 5 10 15 20 25 30 km

Universal Transverse Mercator Map Projection
(UTM 20U NAD83)

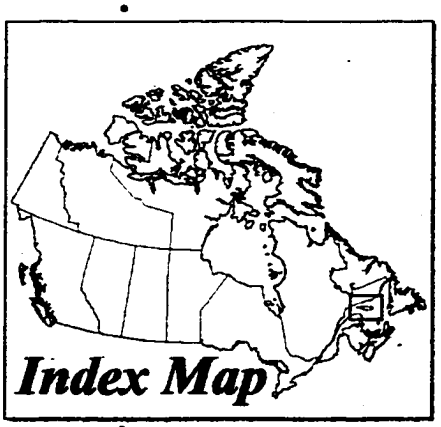

Rivière aux Saumons

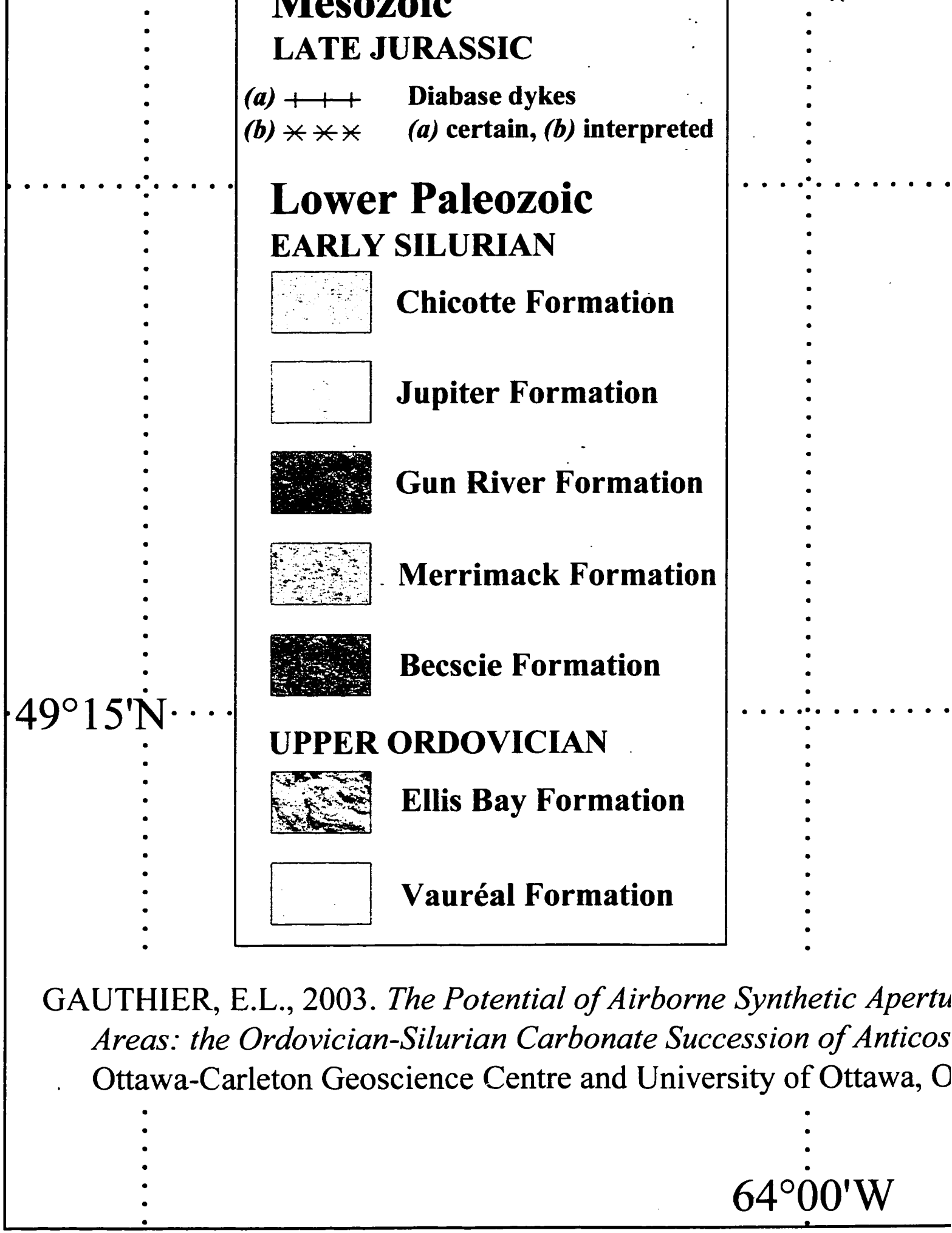

GAUTHIER, E.L., 2003. *The Potential of Airborne Synthetic Apertu*
Areas: the Ordovician-Silurian Carbonate Succession of Anticos
Ottawa-Carleton Geoscience Centre and University of Ottawa, O

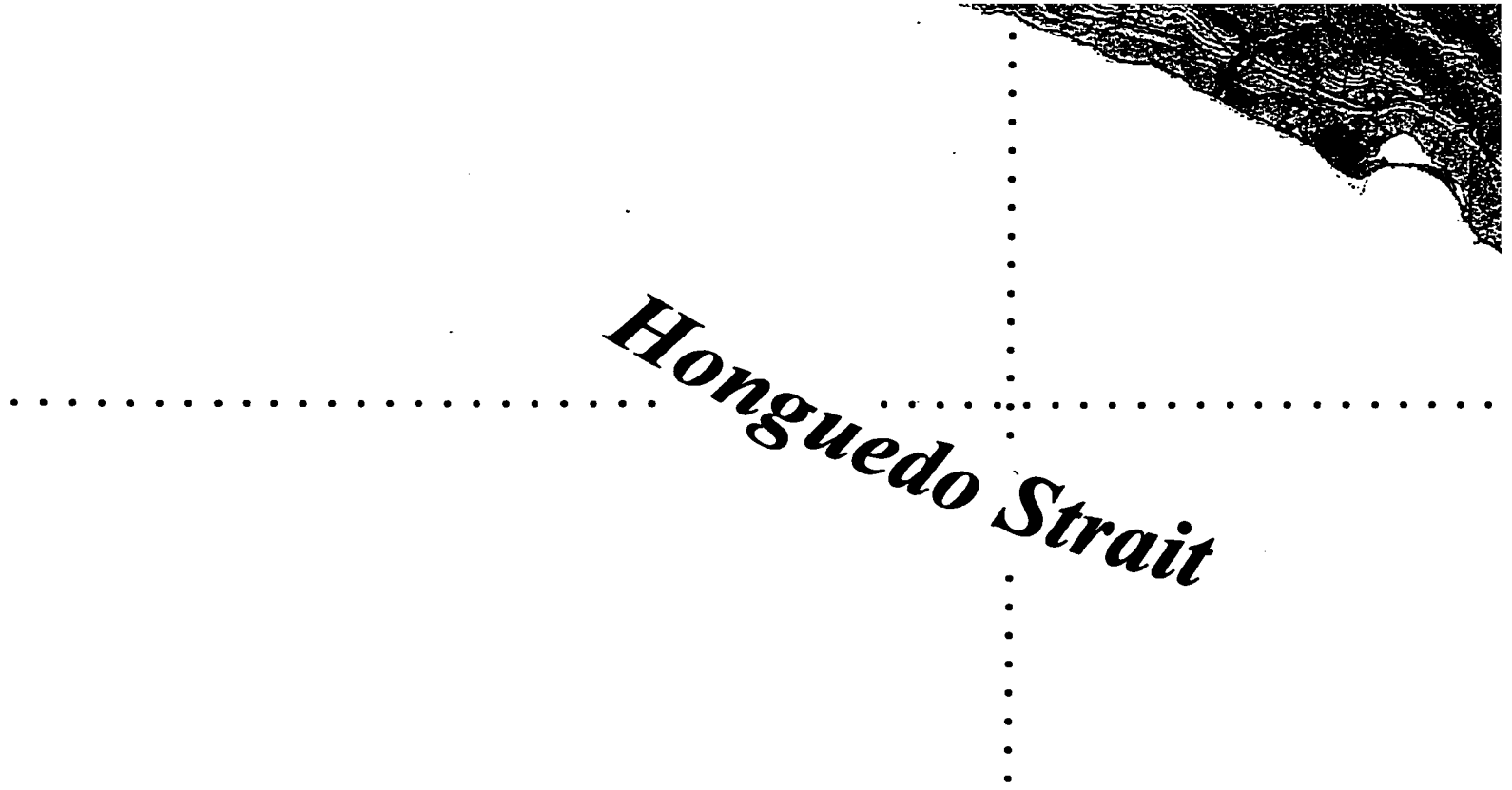

tic Aperture Radar (SAR) Imagery as a Basic Tool for Stratigraphic Inve
of Anticosti Island, Gulf of St.Lawrence, Eastern Canada. M.Sc. Thesis i
Ottawa, Ottawa, Canada.

0'W

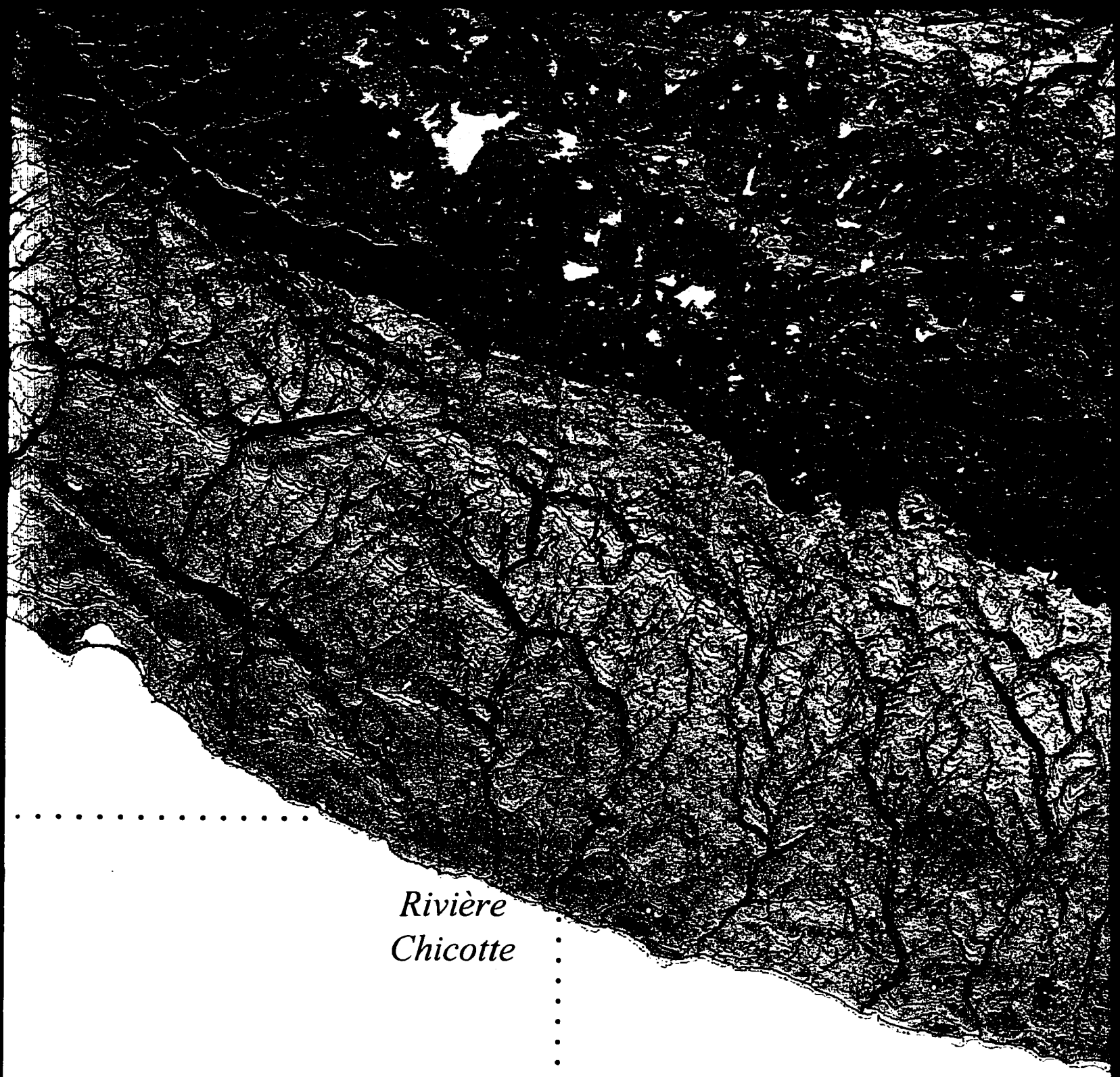

raphic Investigations in Forested
Sc. Thesis in Earth Sciences,

63°00'W

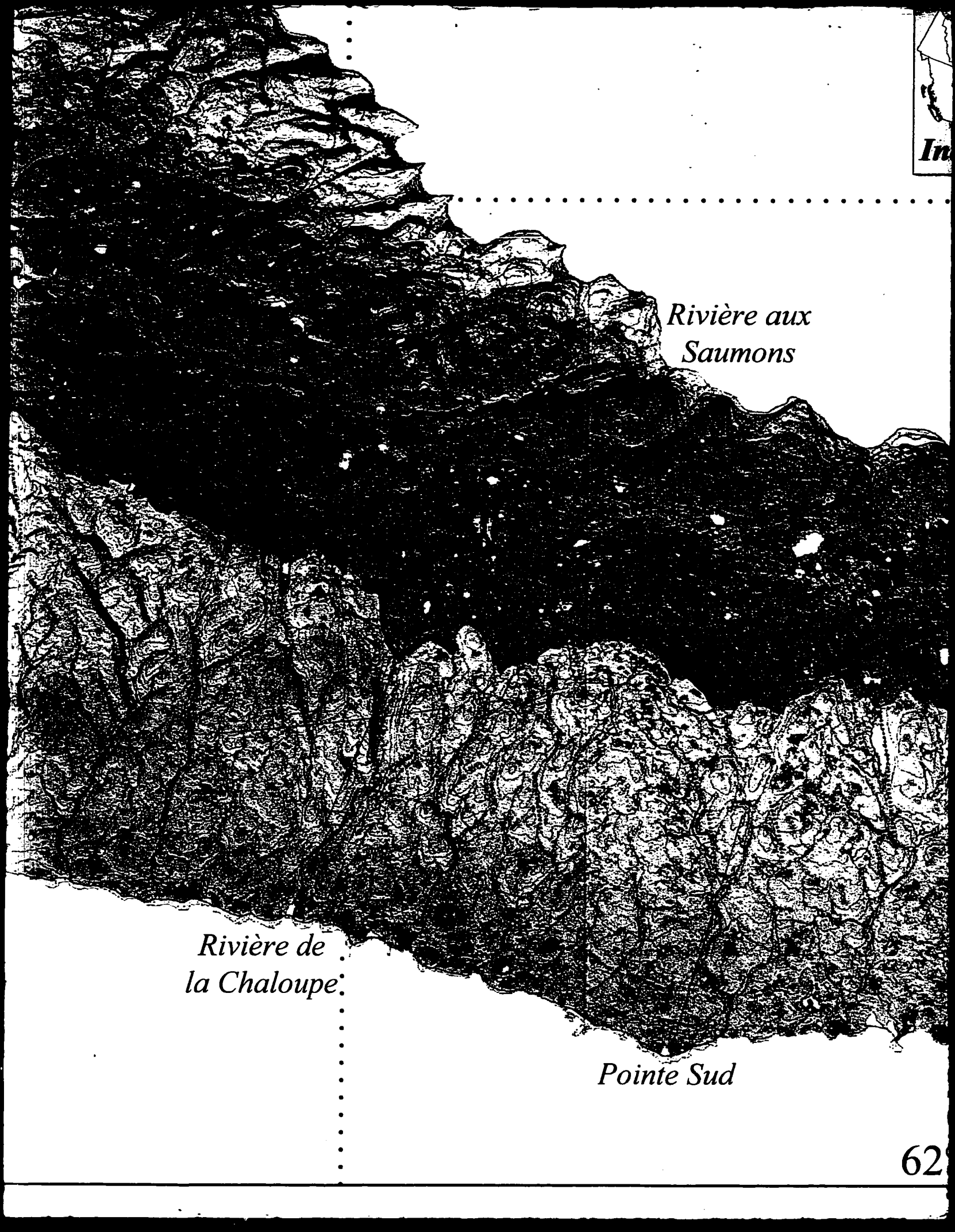
Rivière aux
Saumons
Rivière de
la Chaloupe
Pointe Sud

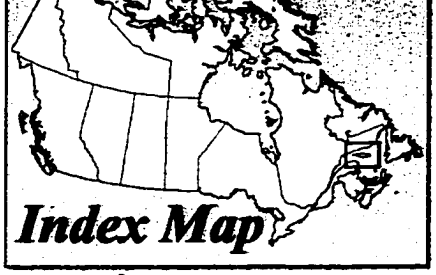

Rivière aux Saumons

Cap de la Table

49°15'N

Pointe Est

Pointe Heath

inte Sud

62°00'W